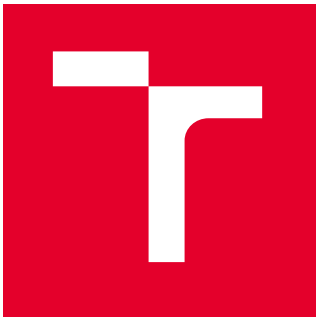

BRNO UNIVERSITY OF TECHNOLOGY

VYSOKÉ UČENÍ TECHNICKÉ V BRNĚ

CENTRAL EUROPEAN INSTITUTE OF TECHNOLOGY BUT

STŘEDOEVROPSKÝ TECHNOLOGICKÝ INSTITUT VUT

DAMAGE MECHANISMS IN NICKEL-BASED SUPERALLOY RENÉ 41 SUBJECTED TO FATIGUE

MECHANISMY POŠKOZENÍ NIKLOVÉ SUPERSLITINY RENÉ 41 PŘI ÚNAVĚ

DOCTORAL THESIS
DIZERTAČNÍ PRÁCE

AUTHOR — **Ing. Tomáš Babinský**
AUTOR PRÁCE

SUPERVISOR — **prof. RNDr. Jaroslav Polák, DrSc.**
ŠKOLITEL

BRNO 2023

Abstrakt

Předkládaná práce se zabývá vznikem poškození ve tvářené niklové superslitině René 41, která je podrobena únavovému zatěžování za pokojové a zvýšené (800 °C) teploty. Slitina byla zkoumána ve dvou termodynamických stavech: po rozpouštěcím žíhání a po stárnutí. Jednoosé zkoušky nízkocyklové únavy byly prováděny symetricky vzhledem k řízené veličině, kterou byla celková podélná deformace. Za účelem studia mechanismů poškození a jejich souvislosti s plastickou deformací byly aplikovány techniky elektronové mikroskopie doplněné o analýzu cyklické odezvy ve formě hysterezních smyček statistickým přístupem. Navíc byly provedeny přerušované únavové zkoušky za účelem studia vývoje povrchového reliéfu ve vztahu k dislokační substruktuře, k čemuž bylo opět využito elektronové mikroskopie. Porušení za pokojové teploty bylo povětšinou transkrystalické, únavové trhliny iniciovaly především uvnitř zrn z povrchového reliéfu. Srovnáme-li dva zkoušené stavy, stárnutý materiál vykazoval vyšší hodnoty cyklického napětí a při srovnatelném napětí dosahoval vyšších životností. Cyklická deformace byla od prvního cyklu lokalizována do persistentních skluzových pásů. Bylo zjištěno, že většina skluzových pásů vzniká na začátku únavového života, kvůli čemuž jsou koherentní precipitáty γ' významně deformovány pouze na začátku únavového života. Skluz v persistentních skluzových pásech vedl k vytvoření povrchového reliéfu ve formě skluzových schodů, extruzí a intruzí. Vznik povrchového reliéfu byl podrobně diskutován s existujícími modely. Vysokoteplotní expozice měla za následek oxidaci povrchu, zejména na oslabených hranicích zrn, kde iniciovaly a následně se šířily únavové trhliny. Výsledné poškození bylo tudíž interkrystalické.

Klíčová slova

Nízkocyklová únava, Lokalizace cyklické deformace, Persistentní skluzový pás, Persistentní skluzová stopa, Dislokace, Elektronová mikroskopie, Superslitina

Abstract

The present study deals with the aspects of fatigue damage in a wrought Ni-based superalloy René 41. The material of interest was investigated in two thermodynamical states: solutionised and aged. Uniaxial, fully-reversed low-cycle fatigue tests were conducted at room and elevated (800 °C) temperatures under total strain amplitude control. To study the relevant damage mechanisms and reveal their connection to plastic deformation, a detailed analysis of the cyclic response using a statistical approach was performed, and advanced microscopy techniques were employed, namely scanning and transmission electron microscopy. Interrupted fatigue tests were performed to study the evolution of surface relief and the underlying dislocation structure. After each interruption, the evolution of the microstructure was analysed using electron microscopy techniques. At room temperature, the damage was mostly transgranular, and the cracks initiated predominantly within grains from the roughened surface. Comparing the two investigated material states, the aged material attained higher stresses and exhibited higher lifetimes in service-relevant stress-life relation. Cyclic deformation was found to localize to persistent slip bands since the first cycle, and the majority of slip bands formed very early in the fatigue life. Hence, shearing of the strengthening phase, coherent γ' precipitates, occurred largely only in the first few cycles. Due to the cyclic slip localization, surface roughening emanated in the form of slip steps, extrusions and intrusions. The formation of surface relief was thoroughly discussed with existing models. The exposure to high temperatures led to an environmental attack, due to which an oxide layer formed on the surface. The cracks initiated and propagated along weakened grain boundaries, and the resulting damage was thus intergranular.

Keywords

Low-cycle fatigue, Cyclic slip localization, Persistent slip band (PSB), Persistent slip marking (PSM), Dislocation, Electron microscopy, Superalloy

Bibliographic citation

BABINSKÝ, T. *Damage mechanisms in nickel-based superalloy René 41 subjected to fatigue*. Brno, 2023. Available at: https://www.vut.cz/studenti/zav-prace/detail/150301. Dissertation thesis. Brno University of Technology, Central European Institute of Technology. Supervisor Prof. RNDr. Jaroslav Polák, DrSc., dr. h. c.

Declaration

I hereby declare that the dissertation thesis called ‘Damage mechanisms in nickel-based superalloy René 41 subjected to fatigue’ was written solely by myself under the supervision of Prof. RNDr. Jaroslav Polák, DrSc., dr. h. c. All the presented results are original, and all sources of information are fully listed in the References.

Brno, 21. 4. 2023 Ing. Tomáš Babinský

Acknowledgements

I would like to express my gratitude to several people who supported me throughout my studies.

Firstly, I sincerely thank my family who provided all the love and care I needed to successfully navigate myself emotionally through my studies.

Secondly, a huge thank you to my supervisor, Prof. Jaroslav Polák, for the necessary guidance and help he provided to me, and the countless discussions, which always clarified any issues I came up with, and finally also for providing space for my self-realization in the field of science.

Lastly, I thank all my friends and colleagues from the Institute of Physics of Materials in Brno, most of all my co-supervisor Dr. Ivo Kuběna for teaching me how to operate FIB and TEM, Dr. Ivo Šulák for help with TEM analyses, numerous discussions, and support on issues regarding fatigue of superalloys and electron microscopy in general, and Mr. Ladislav Poczklán, for support with the Weibull fits on my data. I would like to thank all these guys also for keeping me sane by being good friends and creating a friendly working environment.

Apart from that, I am thankful to the Institute of Physics of Materials for providing me the necessary infrastructure to conduct all the fatigue tests and electron microscopy observations. It has been a real pleasure to work there, and I consider myself lucky to be a part of it.

Table of contents

1 Introduction

Along with the development of materials science since the 19th century, several fields of science dedicated to specific problems arose in time. The need for materials able to withstand many years of service led to the research of premature cracks and the fatigue damage causing them. Thus, fatigue damage is of the utmost importance for the material design of various mechanical components. Fatigue refers to the changes in properties and microstructure due to the applied repeated loading. The key feature of research in the area of fatigue damage is the description of fundamental mechanisms taking place in any material under the conditions of fatigue loading.

According to the most widespread approach, we distinguish two major areas of fatigue life: *low-cycle* and *high-cycle fatigue*, which are separated by a limit of 10^5 cycles. Whereas researchers studying fatigue life of mechanical parts supposed to withstand a huge number of cycles, e.g. in the automotive industry, focus on high-cycle fatigue, researchers studying limits of extremely thermally exposed materials, e.g. in jet engines during take-off/landing procedure, focus on low-cycle fatigue. Low-cycle fatigue corresponds to extreme loading conditions above the yield limit of the material, which results in severe damage throughout the component. Even though the mechanisms of high-cycle fatigue may vary significantly, the basic mechanisms of low-cycle fatigue are also valid for the high-cycle fatigue domain as well. The operating mechanisms are dependent not only on the experimental conditions but also on the applied stress or strain. The number of cycles until fracture is generally the higher the less plasticity is induced in a material. The role of plastic strain in cyclic damage was independently clarified by Coffin (1954) and Manson (1953). The formulated empirical Coffin-Manson's law marks the beginning of a systematic investigation of the aspects of cyclic plasticity and is still the most used approach for the assessment of the cyclic plastic behaviour of materials.

Although the fundamental fatigue mechanisms have been explained quite well in simple metals such as pure copper or aluminium, the fundamental mechanisms acting in engineering materials with complex microstructures such as nickel-based superalloys are less clear. This is crucial for better understanding of material behaviour under real operating conditions, and eventually more precise fatigue-life estimations of relevant components. Nickel-based superalloys are commonly used for manufacturing of hot-going components for almost a century. A typical example of application are turbine blades and vanes in aircraft engines, emphasizing the essential role superalloys play, for instance, in air travel or energy conversion. The excellent high-temperature performance is closely related to the unique microstructure of superalloys, typically exhibiting a large volume fraction of coherent precipitates embedded in the matrix. It is, however, unclear to this day how exactly this unique microstructure affects the evolution of fatigue damage. Such fundamental relationship is possible to assess only with the help of high-resolution imaging techniques such as scanning and transmission electron microscopy.

Hence, in this work, advanced microscopy techniques were employed to study relevant damage mechanisms under cyclic loading in low-cycle regime in the material of choice – nickel-based superalloy René 41.

2 Theoretical background

The commonly used argument over the insignificance of low-cycle fatigue says that the component design strives for the highest fatigue life possible and thus, exercised loading does not even reach the yield limit of the component material. This idea is not completely false and yet not completely true. During start-up or shut-down periods, any necessary interruptions of the usual operation, or in the vicinity of the notches, the yield limit might be exceeded, and elasto-plastic behaviour occurs. Resulting strain localization may lead to the initiation of fatigue cracks which may grow under standard service conditions and, eventually, a premature fracture may occur as evidenced by a catastrophic case of crashed Comet aeroplanes [1].

There are two major approaches to fatigue design: stress-based and strain-based. These methods correspond to the number of stress or strain cycles completed until the component breaks due to fatigue failure. There are 3 stages of fatigue life: firstly, the change of mechanical properties related to the response of the tested material, secondly, the initiation of fatigue cracks due to the existence of surface relief or metallurgical inhomogeneities and thirdly, the propagation of major crack and failure when the length of the crack reaches the critical value. Since the initiation of the major crack covers most of the fatigue life, the low-cycle fatigue approach is often considered a design against fatigue crack initiation. "The stresses associated with low-cycle fatigue are generally high enough to cause appreciable plastic deformation before failure. Under these circumstances, the fatigue life is characterized in terms of the strain range." [1]

Laboratory mechanical testing of standard room-temperature fatigue may be performed under the control of either total or plastic strain amplitude. To keep testing conditions steady, the strain rate is usually constant. Fatigue specimens are usually round and smooth-surfaced, however flat specimens are being used as well. The basic output of the low-cycle fatigue experiment is a set of stress-strain hysteresis loops. Hysteresis loops can be analysed later to gain additional information about the evolution of mean stress, the width of the loop, effective modulus etc. The setup and the usual approach are not dogmatic and can be adjusted to the specific needs of the research, e. g. including thermal cycles results in thermomechanical fatigue taking place in aircraft during take-off/landing. Shortcut procedures, e.g. by raising the strain amplitude after a definite number of cycles, enable evaluation of different loading conditions on one specimen. The specimens can be hollow so that real operating conditions in pipes and tubes can be simulated etc. Adjustments to standardized fatigue testing may prove useful in many cases as it makes life predictions more accurate, however its use is often confined to the specific case and cannot be generalized.

Systematic investigation of low-cycle fatigue behaviour dates back to 1954 when Coffin and Manson independently found the empirical relation between applied plastic strain and the number of cycles until failure, which has been generalised into

$$\varepsilon_{ap} = \varepsilon_f'\left(2N_f\right)^c \tag{2.1}$$

where ε_{ap} stands for plastic strain amplitude, ε_f' for fatigue ductility coefficient, N_f for the number of cycles until fracture and c for fatigue ductility exponent. Eq. (2.1) is a power law and nowadays is widely known as Coffin-Manson law [1–2].

Special attention has been paid to the description of mechanisms governing fatigue damage. Studies of mechanisms, as well as studies dedicated to the influence of various mechanical, microstructural and environmental factors, have been allowed by the innovations in the field of microscopic techniques. Early evidence on Swedish iron under repeated reversals of stress

provided by Ewing and Humfrey [3] revealed the existence of slip bands which "appear in ordinary testing when any portion of the material has passed its limit of elasticity under strain." In 1950 microscopic striations were first reported, yet their connection to the growth of the fatigue crack was suggested later by Forsyth and Ryder [4]. Thompson and Wadsworth [5] noticed that slip bands emerge on the surface as slip markings after fatigue loading and some of the bands develop into "obvious fatigue cracks". It was proved that some of the marks are persistent as they reappear when the surface is repolished and the specimen is further cycled. This finding turned out to be significant as the localization of the dislocation slip into slip bands is a key feature of cyclic plastic behaviour and the occurrence of the resulting damage in metallic engineering materials [1, 6].

2.1 Cyclic plasticity

2.1.1 Parameters of cyclic straining

2.1.1.1 Monotonic loading

If a body is subjected to external loading, stress and strain are produced. A commonly agreed convention marks the stress in tension as positive and the stress in compression as negative. Analogically, the strain characterizing the state of a material is governed by the same convention. The simplest relation between stress and strain describes the case of unidirectional straining of continuous, homogeneous and isotropic bodies – it is the well-known Hooke's law

$$\sigma = E\varepsilon \tag{2.2}$$

where σ stands for applied stress, E for Young's modulus and ε for tensile strain in the direction of applied stress. Eq. (2.2) is a result of several simplifications of the tensor relation between stress and strain. In a pure shear straining, Eq. (2.2) transforms into

$$\tau = G\gamma \tag{2.3}$$

where τ stands for applied shear stress, G for shear modulus and γ for shear strain. The elastic constants E and G are mutually dependent in the form of

$$G = \frac{E}{2(1+\nu_p)} \tag{2.4}$$

where ν_p stands for Poisson's ratio. Constants E, G and ν_p are unique for each material and may vary in each direction profoundly if the material is not isotropic, which is typical for single crystals. Polycrystalline materials usually contain many inhomogeneities such as precipitates, segregated atoms at grain boundaries etc., yet on a macroscale, they are considered isotropic since they possess little to no anisotropy due to the random orientation of grains. This trait can be affected by metallurgy, metal forming processes, heat treatment etc. [2]

The occurrence of damage in metals is determined by plastic deformation, i.e., the slip of mobile line defects – dislocations on crystallographic planes, and the generation of new defects. Plastic deformation of individual grains is governed by Schmid's law. To deform plastically, a grain must reach critical shear stress

$$\tau_0 = \sigma_0 \cos\theta \cos\lambda \tag{2.5}$$

where σ_0 stands for tensile (or compression) stress corresponding to the yield limit, θ for an angle between the loading direction and the slip plane normal and λ for an angle between the loading direction and the slip direction. Eq. (2.5) can be simplified in the form of

$$\tau_0 = m\sigma_0 \tag{2.6}$$

where m stands for Schmid factor. Schmid factor reaches the maximum of 0.5 if $\theta = \lambda = 45°$. When the elasticity is depleted in a polycrystalline material, the slip first takes place in conveniently oriented grains with the highest Schmid factor. Due to plastic deformation, the grains start to rotate so that their Schmid factor increases. That explains the existence of deformation texture in heavily deformed polycrystalline aggregates [7].

If a plastic deformation occurs, total strain is no longer governed by Hooke's law as the stress–plastic strain relationship is not linear. Total strain ε_t can be divided into the elastic and plastic component

$$\varepsilon_t = \varepsilon_e + \varepsilon_p \tag{2.7}$$

where ε_e stands for the elastic component and ε_p for the plastic component of total strain. By combining Eq. (2.2) and Eq. (2.7), plastic strain can be estimated as follows

$$\varepsilon_p = \varepsilon_t - \frac{\sigma}{E}. \tag{2.8}$$

If the loading is stopped before the fracture occurs, plastic strain remains in the material. That is caused by the irreversible movement of dislocations and thus, plastic strain is considered irreversible in monotonic loading. In cyclic loading, the situation is different [2].

2.1.1.2 Cyclic loading

As mentioned in the introduction, fatigue refers to the changes in properties and microstructure under applied repeated loading. The repetition of loads can be "either truly variable or can be periodic or even harmonic. It can be characterised by the alternating of local maxima and minima (peaks and troughs). The resulting strain-time history also contains maxima and minima." [2] Applying repetitive loads to a specimen is commonly called cycling or cyclic loading. Let's consider the simple case, harmonic loading, as depicted in Fig. 2.1.

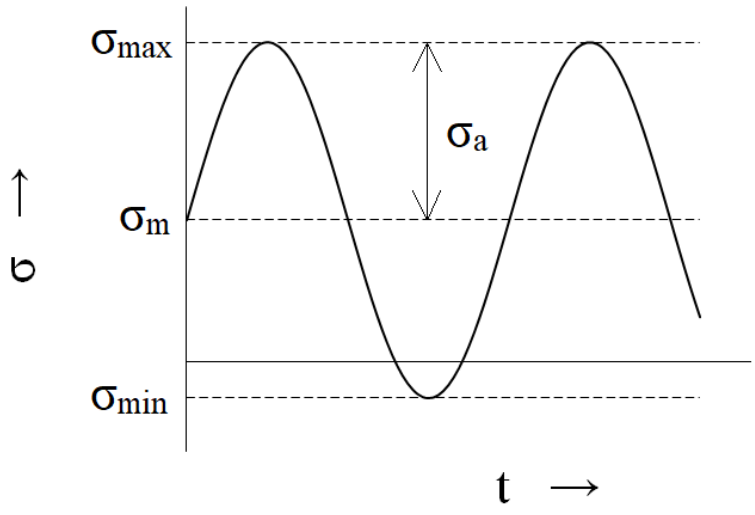

Fig. 2.1. Stress-time history in harmonic sinusoidal loading.

σ_{max} and σ_{min} refer to maximum stress and minimum stress in cycling, respectively. The cycling is primarily defined by stress amplitude σ_a, given by half the difference between maximum and minimum stress, and mean stress σ_m, given by half the sum of the maximum and minimum stresses. An important parameter is the stress asymmetry, given by the relation

$$R = \frac{\sigma_{min}}{\sigma_{\max}}, \tag{2.9}$$

which gives information about the prevalence of the tensile or compressive part of the cycle. Analogously to the abovementioned, strain parameters ε_{max}, ε_{min}, ε_a and ε_m and plastic strain parameters $\varepsilon_{max,p}$, $\varepsilon_{min,p}$, ε_{ap} and ε_{mp} can be defined.

The shape of stress- or strain-time dependence may be selected concerning the proposed conditions of the experiment. In strain cycling, which is typical for low-cycle fatigue experiments, the triangular shape of strain-time dependence is mostly preferred because the strain rate remains constant within the half-cycle. At the end of each half-cycle, the strain rate $\dot{\varepsilon}$ suddenly changes from positive value to negative value and vice versa. The switch must be fast enough not to influence the strain rate considerably. Such conditions are met if the frequency of strain cycling is

$$f = \frac{\dot{\varepsilon}}{4\varepsilon_a} < 1\ Hz, \tag{2.10}$$

where $\dot{\varepsilon}$ stands for strain rate. It is important to keep the strain rate constant since it strongly influences both the density of mobile dislocations via Orowan's relation as well as the effective stress component [2].

During cycling, the stress-strain response is recorded in the form of time-dependent hysteresis loops, depicted in Fig. 2.2. Coordinates can be shifted so that relative stress σ_r and relative strain ε_r of the half-loop is always positive which can be favourable for analyses such as the statistical theory of the hysteresis loop [8]. Relative stress σ_r, relative strain ε_r and relative plastic strain ε_{pr} are given by

$$\sigma_r = \sigma + \sigma_a \tag{2.11}$$

$$\varepsilon_r = \varepsilon + \varepsilon_a \tag{2.12}$$

$$\varepsilon_{pr} = \varepsilon_p + \varepsilon_{ap} \tag{2.13}$$

for tensile half-loop and

$$\sigma_r = \sigma - \sigma_a \tag{2.14}$$

$$\varepsilon_r = \varepsilon - \varepsilon_a \tag{2.15}$$

$$\varepsilon_{pr} = \varepsilon_p - \varepsilon_{ap} \tag{2.16}$$

for compressive half-loop. Plastic strain amplitude can be estimated analogously to Eq. (2.8) as

$$\varepsilon_{ap} = \varepsilon_a - \frac{\sigma_a}{E}. \tag{2.17}$$

However, true plastic strain amplitude may differ from the value estimated by Eq. (2.17). This phenomenon can be attributed to the change of Young's modulus which can be significant during cycling. A more reliable estimation arises from the actual hysteresis loop as "the half-width of the hysteresis loop at the mean stress" [2]

$$\varepsilon_{ap} = \frac{\Delta\varepsilon_p}{2}, \tag{2.18}$$

where $\Delta\varepsilon_p$ stands for the width of the hysteresis loop. There is still a small inaccuracy present since the actual plastic strain amplitude is slightly higher due to the existence of the reverse

strain. Reverse strain arises when areas with relatively low critical shear stress start deforming in a reverse direction (that can be reconciled with a statistical approach considering microvolumes with low critical internal stress which is discussed in more depth in Chapter 2.1.1.3). The majority of cyclic plastic strain is irreversible and accounts for the qualitative changes to the microstructure of the strained material [2, 9].

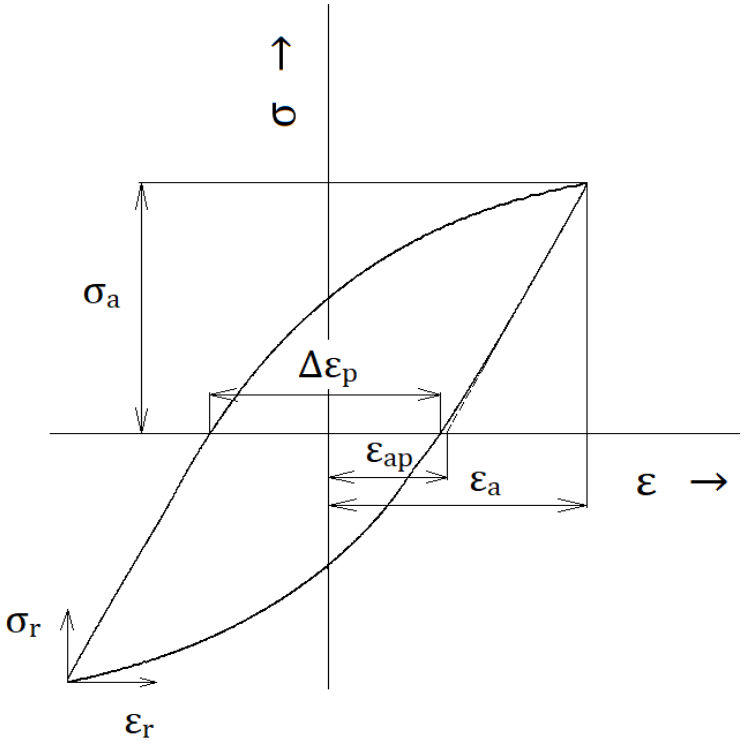

Fig. 2.2. Model hysteresis loop in strain cycling.

The evolution of the hysteresis loop and its characteristics provides basic information about the response of the material to fatigue loading. The hysteresis loop is not closed until the response is fully saturated. If the stress amplitude gradually increases and the plastic strain amplitude decreases, the material cyclically hardens. On the other hand, if the stress amplitude gradually decreases and the plastic strain amplitude increases, the material cyclically softens. Cyclic softening is usually followed by the saturation of the cyclic plastic response, which is accompanied by the closure of the hysteresis loop [2].

It is well established that plastic strains are inevitable for the development of fatigue damage and eventually fracture in ductile materials. In real applications, the imposed plastic strains due to cyclic loading are usually small and the contribution to the damage per cycle appears negligible and even decreases with cyclic work hardening. It is, however, the cumulative character of plastic deformation through the accumulation of the damage that is critical. A nominal measure of damage accumulation in *i*-th cycle is the cumulative plastic strain

$$\varepsilon_c = 2\sum_{1}^{i} \Delta\varepsilon_p. \tag{2.19}$$

It is important to note that cumulative plastic strain is an approximate measure of the overall fatigue damage as it solely incorporates the influence of irreversible plastic strains, and completely ignores the interactions with the environment, microstructural inhomogeneities etc. [1–2]

2.1.1.3 Statistical theory of the hysteresis loop

The statistical approach to the analysis of cyclic plasticity in metals is based on Masing's hypothesis [10], which presumes a distribution of elementary volumes with different flow stresses in the material bulk. The original idea was expanded to include thermal effects by Polák and Klesnil [11] (in Czech) and Burmeister and Holste [12] and finally generalized by Polák and Klesnil [8]. Although originally designed to analyse simple one-phase materials [13], the statistical approach has proven to be an effective tool in the determination of the role of individual phases in multiphase materials (see e.g. [14–16]) too.

The basis of the Polák and Klesnil's generalization [8] is an assumption considering a separation of material bulk into microvolumes with different critical internal stresses σ_{ic}, which oppose the applied external stress, and which are determined by long-range stress fields from an internal structure of a material, e.g. dislocation density and dislocation arrangement. The distribution of microvolumes is defined by a normalised probability density function of critical internal stresses

$$\int_0^\infty f(\sigma_{ic})\, d\sigma_{ic} = 1. \tag{2.20}$$

In real crystals, however, there are many sources of short-range obstacles, such as P-N stresses, which need to be overcome too to set the dislocation in the respective microvolume to motion, and which are represented by effective stress component σ_e. Importantly, short-range obstacles may be overcome by thermal activation. As the internal stress component needs to be reached as a first prerequisite for a dislocation to move, the effective stress component is necessary to achieve the velocity derived from the prescribed strain rate. Total stress can thus be expressed as a sum of internal σ_i and effective σ_e stress components as follows

$$\sigma = \sigma_i + \sigma_e\ . \tag{2.21}$$

Analogously, critical flow stress can be expressed in the form

$$\sigma_0 = \sigma_{ic} + \sigma_{es}\ . \tag{2.22}$$

For sake of simplicity, it is assumed that while loading beyond the yield limit of the respective microvolume, critical internal stress remains constant and the effective stress eventually saturates at the saturated effective stress value σ_{es}, which is for a given strain rate a material constant. The slope of the respective curve in the $\sigma_e - \varepsilon$ representation is determined by effective Young's modulus E_{eff}

$$E_{eff} = \left(\frac{\partial \sigma_e}{\partial \varepsilon}\right)_{\varepsilon=\sigma_{e0}/E} = E\left[1 + \exp\left(\frac{\sigma_{e0} - \sigma_{es}}{\alpha}\right)\right] \tag{2.23}$$

where σ_{e0} stands for the initial value of effective stress and α is a parameter defining the obstacles, which may be overcome by thermal activation. Hence, for a small initial effective stress ($\sigma_{e0} \approx 0$), it holds $E_{eff} \approx E$. The effective modulus can be derived directly from the slope of the loading curve in the σ–ε plot.

Both stress components can be derived from the hysteresis loops, provided the plasticity is induced in the tested material by the applied stress, which is usually the case in low-cycle fatigue experiments. The shape of the hysteresis loop can be expressed in relative coordinates as follows

$$\sigma_r = \varepsilon_r E_{eff} \quad \text{for} \quad \varepsilon_r \leq \frac{2\sigma_{es}}{E_{eff}} \tag{2.24}$$

$$\sigma_r = \frac{\varepsilon_r E_{eff}}{2} - 2G\left(\frac{\varepsilon_r E_{eff}}{2} - \sigma_{es}\right) \quad \text{for} \quad \frac{2\sigma_{es}}{E_{eff}} \leq \varepsilon_r \leq 2\varepsilon_a \tag{2.25}$$

where *G(x)* is a second integral function of the probability density function. Polák *et al.* [13] showed that the probability density function of the critical internal stresses can be obtained from experimental data by double differentiation of the hysteresis loop. Hence, considering the double differentiation of Eq. (2.25) to relative strain, the second derivative is obtained in the form [8]

$$f\left(\frac{\varepsilon_r E_{eff}}{2} - \sigma_{es}\right) = -\frac{2}{E_{eff}^2}\frac{\partial^2 \sigma_r}{\partial \varepsilon_r^2} \tag{2.26}$$

Physical meaning of a double differentiated hysteresis loop is a material hardening rate within a half-loop. Effective stress can be derived from the shift of the experimentally obtained second derivative, which corresponds to the probability density function. The evolution of the respective peaks corresponds to the rearrangements in the dislocation structure, resulting in cyclic hardening, cyclic softening, or saturation of the cyclic stress-strain response [16].

2.1.2 Mechanisms of cyclic plasticity in fcc metals

The partial irreversibility of cyclic slip plays a crucial role in the onset of fatigue damage, which is closely related to the surface relief evolution, as stated by the early work of Thompson and Wadsworth [5]. The resulting qualitative changes due to pure fatigue loading are confined to the movement of dislocations on active slip planes. Cyclic slip irreversibilities are produced in the bulk of the strained material as well as on its surface, where the surface relief arises. The surface relief thus reflects a whole history of cyclic slip irreversibility accumulation both on the surface and in the bulk underneath. Hence, the occurrence of cyclic slip irreversibilities due to dislocation motion in the bulk under the surface indeed contributes to the gradual evolution of fatigue damage. In metals with the face-centred cubic crystal structure (fcc metals), Mughrabi [9] considers several mechanisms:

- cross-slip of screw dislocations, implying that forward and reverse glide of dislocations do not occur on the same slip planes,
- mutual annihilation of the opposite screw and opposite edge dislocations: whenever a dislocation is annihilated, this marks the end of its glide path, implying that reverse deformation cannot occur along the same glide path,
- the random to-and-fro glide of dislocations.

The degree of cyclic slip irreversibility depends on the induced strain, or more precisely induced plastic shear strain amplitude. Generally, the larger the plastic shear strain amplitude, the larger the degree of cyclic slip irreversibility is. 'The reason is simply that small to-and-fro dislocation displacements will be more reversible in the preceding sense than larger ones," [9].

Fcc metals can be divided into two groups based on the character of the slip: they prefer either wavy slip or planar slip. The pivotal factor separating the two groups is stacking fault energy. Metals with (relatively) high stacking fault energy, typically simple single-phase metals such as pure copper or nickel, promote cross-slip behaviour, resulting in the almost complete annihilation of screw dislocations and formation of dipolar edge dislocation clusters, or dislocation cells at sufficiently high strains. On the other hand, metals promoting "planar

slip" exhibit (relatively) low stacking fault energy due to which the recombination of partial dislocations and thus cross-slip is difficult. Such behaviour is usually promoted by a more complex microstructure, e.g., in precipitation-hardened alloys such as nickel-based superalloys. The resulting microstructure contains planar dislocation arrays on one or more slip systems, depending on the imposed strain. [9, 17]

2.1.2.1 Dislocation arrangements under cyclic loading

Strains imposed by cyclic loading result in the glide of dislocations, ultimately forming more or less stable dislocation arrangements. The character of such arrangements is primarily determined by resolved shear strain amplitude.

If the strains are low (region A of the cyclic stress-strain curve in Fig. 2.3, showing a simplified example of fcc single crystal oriented for a single slip), the whole crystal is deformed and so-called dislocation veins are formed, which are dipolar or multipolar clusters of edge dislocations. The dislocation-rich veins are separated by dislocation-poor channels, occupying approximately half the volume. The dislocation structure is inhomogeneous only on a microscale.

As the vein structure cannot accommodate higher strains, it breaks down locally and the dislocations arrange themselves in thin bands, lying parallel to active slip planes (region B in Fig. 2.3). These bands are formed through the crystal and are softer than the surrounding matrix which results in gradual localization of cyclic slip in them. Once formed, the bands are persistent throughout the cyclic loading, hence being called persistent slip bands (PSBs). Internally, the persistent slip bands exhibit a ladder-like structure consisting of thin (primary) dislocation-rich walls, which are mainly built of edge dislocations. They are separated by dislocation-poor channels, scarcely populated by screw dislocations gliding between two neighbouring walls. The edge dislocations in the walls form dislocation dipoles, mostly of vacancy type [18]. Cyclic straining of the material thus results in the production of vacancies, which are accountable for volume changes of the strained material, as follows from resistivity measurements [19]. The characteristic ladder-like PSB structure has a typical thickness of ~1 μm in materials promoting wavy slip [2, 20]. On the other hand, materials promoting planar slip exhibit thin PSBs which are often grouped in macro-PSBs with a typical thickness up to ~100 nm [21]. The ladder-like structure is usually missing and internally the PSBs consist of randomly distributed parallel arrays of dislocations [22]. Cyclic stress is usually saturated since in PSBs, dynamic equilibrium is reached between the multiplication and annihilation of both edge and screw dislocations, resulting in a steady production of vacancies [19, 23].

With increasing plastic shear strain amplitude, the PSBs gradually fill the whole volume. At sufficiently high strains, secondary slip systems are activated early in the fatigue life and the dislocation arrangement of cells separated by (secondary) cell walls arises through the whole volume. However, engineering materials are usually randomly oriented polycrystals. Hence in real applications, various modifications and combinations of the three dislocation arrangements can arise. [2, 9]

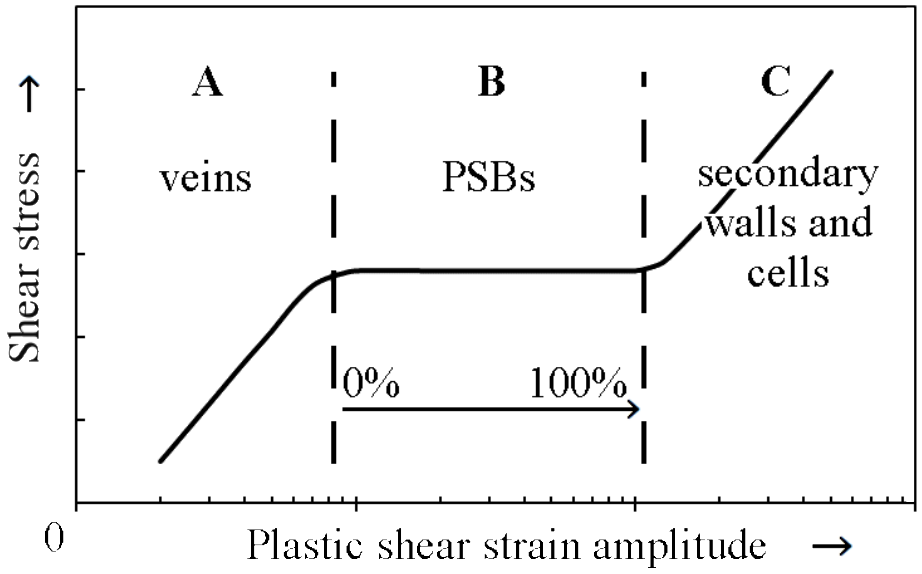

Fig. 2.3. Schematic cyclic stress-strain curve of a simple single-phase fcc metal single crystal oriented for a single slip in a semilogarithmic plot. The curve is separated into 3 regions with corresponding prevalent dislocation structures: Region A: dislocation veins, region B persistent slip bands (PSBs), and region C: dislocation cells. Reproduced from [2].

2.1.2.2 Surface relief and its relation to fatigue crack initiation

In a low-cycle regime, fatigue damage generally initiates at the surface. Thompson and Wadsworth [5] noted that "it is still far from obvious at what stage a 'persistent slip band' may properly be called a 'crack'". Given the statement dates over 60 years back, it remains an open question as there is no general agreement in the scientific community. The significance of PSBs in fatigue is, however, nowadays clear. The authors [5] performed an interrupted test – after each interruption, the slip markings on the surface were removed by electropolishing, but they reappeared during cycling, proving them 'persistent' in nature. As a result, the fatigue life of a specimen was 125 % longer than predicted which pointed out the crucial role PSBs play in fatigue crack initiation. With the current knowledge, however, we should strictly recognize PSBs as a bulk feature and persistent slip markings (PSMs) as the manifestation of PSBs on the specimen/component surface.

The formation of a PSB leaves a roughened surface at the sites where the PSB emerges on the surface – PSMs appear – and an almost featureless surface remains between the individual PSMs. A typical PSM consists of material extruded above the surface on top of the PSB in the direction of the active Burgers vector (extrusion) and a thin crack-like layer of missing material (intrusion) [24]. There is a great number of models (see e.g. [24–32]) attempting to explain the exact mechanism of PSM formation at the surface, and its relation to fatigue crack initiation.

One of the first physics-based models is the EGM model which is still widely recognized today [26–27]. The EGM model proposes a rapid formation of so-called static extrusion on the surface above the PSB due to the production of vacancies by the annihilation of edge dislocations in dislocation walls. A temperature effect is manifested in higher diffusivity of vacancies. The model assumes a diffusion of vacancies to the matrix from the thin sheet adjacent to the PSB-matrix interface, which is equivalent to the transport of matter in the other direction. The resulting extrusion growth is thus continuous but confined only to narrow regions of PSBs close to the PSB-matrix interface. The model considers only vacancy-type defects due to energy reasons, hence only the formation of extrusions is predicted [9]. The extrusion surface is further

supposed to roughen due to random glide of dislocations, arriving at the extrusion surface and forming there slip steps. [27] The EGM model considers extrusion height *e* as a function of saturated vacancy concentration and grain size. For surface grains, Mughrabi later proposed [9] a simplified relation in the form

$$e \approx 2 \cdot 3 \cdot 10^{-4} \cdot d \tag{2.27}$$

where *e* stands for static extrusion height measured in the direction of active Burgers vector and *d* for grain size measured in the direction of active Burgers vector. While the equation shows a satisfactory fit in some cases [33], in other cases the observed extrusion heights differ by more than one order of magnitude even after a few elapsed cycles [34]. The model assumes there are two types of stress raisers at the surface, acting as nucleation sites of fatigue cracks:

- The surface steps at the PSB-matrix interfaces, formed as a consequence of stress concentration at the tip of PSBs parallel to the active Burgers vector,
- Valleys at the extrusion surface, formed as a consequence of a random roughening due to a random dislocation slip.

It is important to emphasize that the model does not predict the onset of notch-like deepenings (see e.g. [34–35]), labelled as intrusions by other models [24, 36–37], but regards them as already nucleated stage I microcracks. It is also worth noting that fatigue cracks in the early stage do not necessarily lead to failure since the conditions for propagation need to be met as well [9]. Although the EGM model appears to describe the evolution of surface relief and its relation to fatigue crack initiation well, some discrepancies from the experimental observations, e.g. regarding the profile of PSM due to extrusion growth [20] or predicted extrusion heights [34], raise serious doubts over some of the model's assumptions.

A substantial modification of the EGM model was presented by Polák [24], and later extended by Polák and Man [32]. The model proceeds from the fact that vacancy-type defects are steadily produced in PSBs because of cyclic straining [19]. Contrary to the EGM model, Polák assumes the vacancy production takes place in both dislocation walls and channels. Hence, the resulting extrusion height is higher, and the continuous extrusion growth appears over the entire width of a PSB. Polák assumes that the vacancy migration across the PSB-matrix interface and the resulting mass accumulation in the PSB gives rise to internal compressive stress (equivalent to external tensile stress) in the PSB and internal tensile stress (equivalent to external compressive stress) in the narrow sheet of the adjacent matrix. The stress is then relaxed by a formation of an extrusion atop the PSB and thin sharp intrusions at the PSB-matrix interfaces. Intrusions are predicted to appear later due to the higher flow stress of the matrix, which explains the occurrence of solitary extrusions at the specimen surface (see them e.g., in [9, 34, 38]). The sharp shape of the intrusions causes a significant notch effect allowing a relatively easy propagation of the intrusion into the bulk. Hence, intrusions are considered a key feature for fatigue crack initiation. The quantitative approach presented by Polák and Man [32] regards the extrusion height *e* and intrusion depth *i* as

$$e = \frac{plN\cosh(ax)}{\cosh\left(\frac{aw}{2}\right) + \frac{a}{\sqrt{\rho_c}}\sinh\left(\frac{aw}{2}\right)} \quad \text{for } x < \frac{w}{2}, \tag{2.28}$$

$$i = r_{im}N\exp\left(-\sqrt{\rho_c}\left(x - \frac{w}{2}\right)\right) - d_c \quad \text{if } r_{im}N > d_c \quad \text{for } x > \frac{w}{2}, \tag{2.29}$$

where p stands for vacancy production rate in a PSB, ρ_c for edge dislocation density in the matrix, w for the width of the PSB, l for its length in the direction of active Burgers vector, N for cycle number, x for the distance from the middle of a PSB, a for reciprocal characteristic diffusion distance, r_{im} for maximum intrusion growth rate defined as

$$r_{im} = \frac{pl\sqrt{\rho_c}}{a\left(\coth\left(\frac{aw}{2}\right) + \frac{a}{\sqrt{\rho_c}}\right)} \tag{2.30}$$

and d_c for material-dependent parameter which characterizes the delay between the start of the extrusion and intrusion growth (for more details see [32]). If the condition in Eq. (2.29) is not met, the intrusion does not arise. Equations (2.28) and (2.29) predict approximately flat extrusion and sharp intrusion at PSB-matrix interface [32]. The model shows an appreciable agreement with experiments on simple metals even if a ladder-like dislocation structure is not present and the slip is planar [20].

The two aforementioned models represent the most accurate predictions of the true surface relief. The early model of Tanaka and Mura [25] correctly predicts the occurrence of slip steps but ignores the point defect production and migration and thus fails in the case of more developed PSMs. The models based on random slip [27–28] explain the surface roughening of the PSM well, however, fail to satisfactorily explain the more developed PSMs. That can be accounted to the non-random nature of PSM formation. The micromechanical model of Repetto and Ortiz [29] predicts the crack initiation sites precisely, however, its prediction of gradually sharpening grooves becoming microcrack fails to meet the experimentally observed reality [20]. Recent progress in computational power gave rise to models based on discrete dislocation dynamics [30, 39], which provide appreciable agreement with experimental observations for a small number of cycles. Unfortunately, no predictions are available for a high number of loading cycles, corresponding to real fatigue lives of components, due to the limitations in computational capacity. Also, effects such as non-conservative dislocation motion or point defect diffusion are neglected [40].

2.2 Low-cycle fatigue of nickel-based superalloys

Nickel-based superalloys are a material class commonly used for manufacturing of critical hot-going components in the fields of air transport and energy production, e.g., combustion chamber and turbine blades and vanes of a jet engine, pumps, valves and pipeline of gas and oil extraction fields, reaction vessels for chemicals containment etc. A gradual depletion of natural resources as well as an urge to reduce carbon footprint naturally leads to pressure on increasing the efficiency which, as a direct consequence of thermodynamics, is increased when the operating temperature is increased. Higher efficiency results in lower fuel consumption and hence pollution reduction and cheaper maintenance. Generally, research in the area aims to increase the operating temperature, which results in improved performance and thus heavier payloads, higher speed and greater range. In all cases, the components are subjected to repeated loads and strains. Since cyclic plasticity might be introduced during the start-up and shut-down periods of the aforementioned components, it is of utmost importance to study lifetime behaviour as well as relevant damage mechanisms under low-cycle fatigue (LCF) loading. In some applications, such as turbine blades and discs, LCF is a life-limiting factor. As such, also the LCF properties of nickel-based superalloys indirectly affect our everyday lives, being projected in the costs of goods, transport and energy.

2.2.1 The microstructure of nickel-based superalloys

The feature crucial for the outstanding performance of nickel-based superalloys under severe operating conditions at high temperatures and corrosive environments is the unique microstructure arising from the complex chemical composition. The effect of the most common alloying elements is summarized in Table 1.

Table 1. Main effects the most common alloying elements have on nickel-based superalloy microstructure and resulting properties. Adapted from [41–43].

Element	Partitions to	Effect
Co	γ	Raises solidus of γ'
Cr	γ	Carbide former, improves corrosion resistance, promotes TCP phases
Fe	γ	Decreases oxidation resistance, promotes TCP phases
Mo	γ	Carbide former, increases density, strengthens the matrix
Re	γ	Strongly raises liquidus, retards γ' coarsening, increases misfit
W	γ	Carbide former, promotes TCP phases
Al	γ'	Improves oxidation resistance
Nb	γ'	Promotes γ'' and δ phases
Ti	γ'	Strengthens γ', substitutes Al in γ', decreases the fault energy in γ'
Ta	γ'	Often replaces Ti, strengthens γ'
Zr	grain boundary	Inhibits carbide coarsening, improves grain boundary strength, improves creep strength and ductility
B, C, N	grain boundary	Forms borides (Cr, Mo), carbides, nitrides (Cr, Mo, W, Nb, Ta, Ti)

Typical nickel-based superalloys primarily consist of small coherent precipitates dispersed in the fcc matrix, usually labelled as phase γ. The precipitates have a strong effect on the strengthening due to the coherency strain arising from a small lattice misfit between the precipitates and the matrix. The coherent precipitates are usually the chemically ordered A_3B-type compounds with fcc crystal structure, most usually $Ni_3(Al, Ti)$, labelled as γ' phase, which exhibits anomalous growth in yield strength with increasing temperature [44]. According to Hume-Rothery's classification, Ni_3Al is the most stable A_3B phase [41]. Since γ and γ' have similar cubic structures, the precipitates are often cubic with γ/γ' interfaces aligned on elastically soft {100} planes [42, 45]. Coarsening of γ' precipitates leads to loss of coherency and thus a decrease in strength. The volume fraction of γ' determines, most of all, the high-temperature capability of an alloy [41]. In some alloys, such as IN718, the primary strengthening phase is the disc-shaped $Ni_3(Nb, Ta)$ with a body-centred tetragonal crystal structure, labelled as γ''. It is noteworthy that γ'' phase is stable only to 650 °C, hence the use of γ''-strengthened alloys is limited to 650 °C. Only a few alloys, such as IN625, exhibit no precipitate substructure and rely on solid solution strengthening alone [46].

Due to the carbon content and some carbide-forming elements, carbides of MC, $M_{23}C_6$, M_6C, M_2C and/or M_7C_3-type are often present and contribute to material strengthening via the dispersion in the matrix [47] and reduce creep by inhibiting grain boundary sliding [43]. Carbide formation can be detrimental to creep properties due to different thermal expansion coefficients [48]. In specific alloys, nitride [49] and boride [50] formation can be promoted.

Finally, there are several undesirable phases with a variety of crystal structures, such as β, δ, ε, η, π, or topologically closed-packed (TCP) phases, which might occur in the microstructure due to local chemical heterogeneity at grain boundaries and interdendritic areas. Generally, the occurrence of these phases is detrimental to mechanical properties due to the needle-like

morphology, promoting embrittlement via initiation of early cracks in the component bulk at relatively low stresses [41, 43].

Both the extraordinary strength and the anomalous yielding behaviour of γ'-strengthened superalloys is closely related to the line defects. The precipitates can be sheared by moving dislocations assuming the precipitate size is not too large, which favours Orowan looping mechanism. A single dislocation entering a precipitate on a {111} plane creates a displacement in chemical ordering by a/2<110> and leaves an anti-phase boundary (APB) behind. Hence, a second dislocation of a/2<110>{111} type is needed to restore the γ' lattice to the original perfect state, and the closure vector is thus twice the Burgers vector of a single dislocation. Due to those reasons, the formation energy of an APB is relatively large and an alloy with shearable precipitates exhibits a relative increase in strength. Each dislocation is referred to as superpartial and a pair of superpartials form a superdislocation. Superpartials can further dissociate into a/6<112> Shockley partials, creating a complex stacking fault (CSF) between them, which is manifested in a change in the nearest-neighbour atomic configuration. Due to the relatively low (around 30 mJ/m^2 [51]) stacking fault energy of superalloys, the dissociation is significant and cross-slip is difficult, which promotes planar slip [34] and twinning [52]. Shearing by a/3<112> partials produces either superlattice intrinsic stacking fault (SISF; equivalent to a removal of one {111} plane) or superlattice extrinsic stacking fault (SESF; equivalent to an introduction of extra {111} plane). Four types of dislocation reactions, schematically shown in Fig. 2.4, have been observed [42, 53]:

i. Dissociation by CSF, APB and CSF on {111} planes
$$a[\bar{1}01] \rightarrow \frac{a}{6}[\bar{1}\bar{1}2] + \frac{a}{6}[\bar{2}11] + \frac{a}{6}[\bar{2}11] + \frac{a}{6}[\bar{1}\bar{1}2]$$

ii. Dissociation by APB on {111} planes
$$a[\bar{1}01] \rightarrow \frac{a}{2}[\bar{1}01] + \frac{a}{2}[\bar{1}01]$$

iii. Dissociation by SISF and SESF on {111} planes
$$a[\bar{2}11] \rightarrow \frac{a}{3}[\bar{1}2\bar{1}] + \frac{a}{3}[\bar{1}\bar{1}2] + \frac{a}{3}[\bar{2}11] + \frac{a}{3}[\bar{2}11]$$

iv. Dissociation by APB on {100} planes
$$a[\bar{1}01] \rightarrow \frac{a}{2}[\bar{1}01] + \frac{a}{2}[\bar{1}01]$$

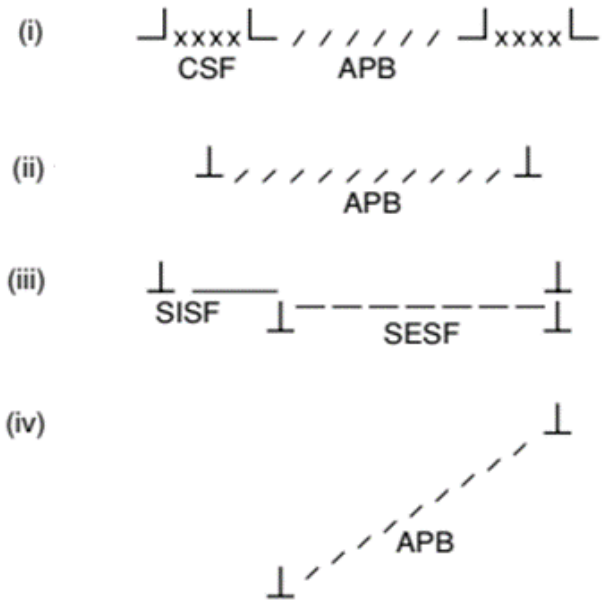

Fig. 2.4. Schematic of possible dislocation reactions in γ' precipitates. Adapted from [42] and [53].

Dislocations can be more complex since superdislocations can dissociate on both {111} and {100} planes, with distinct segments lying on each of the two planes. Since the cube {100} plane only becomes a glide plane in γ' at high temperatures, such configurations involving the dissociation on {100} plane are at relatively low temperatures sessile and thus practically immobile. A typical example is the Kear-Wilsdorf lock, formed by a cross-slip of APB on {100} planes while the two CSFs remain on a {111} plane. The formation of such configurations was proven to be energetically favourable. There is general agreement that cross-slip from octahedral {111} planes to cube {100} planes is the principal reason for the anomalous increase in yield strength with temperature. Since the considered cross-slip is a thermally activated process, it occurs more often with increasing temperature [22], resulting in decreased spacing between the locks and reduction of the free glide path of dislocations. The factors determining the occurrence of the anomalous yield behaviour and related effects, such as the abnormally high work hardening, or the compression/tension asymmetry of the yield stress, have been widely discussed in the literature (for more details see e.g. [54–56]). Since the dislocations are generated in greater numbers at higher temperatures, this can also contribute to more frequent lock formation [42]. Nevertheless, the configuration becomes mobile at high temperatures (usually around 800 °C, based on chemical composition) due to the activation of the slip on the cube planes, which results in a gradual, pronounced drop in yield strength [42, 53].

2.2.1.1 Microstructure as a function of processing technology and heat treatment

There are some differences in the microstructure based on the applied manufacturing technique. Generally, conventional polycrystalline nickel-based superalloys are manufactured in ingots and further used in either as-cast or cast-and-wrought states. Powder metallurgy has been used for manufacturing of specific components, which are compacted by hot isostatic pressing (HIP), sometimes followed by forging, or ball milling and extrusion. Recent progress in the development and optimization of additive manufacturing (AM) led to an increased interest in its capabilities [57] but AM, related microstructures and mechanical properties are still an open field to study.

The cast alloys allow relatively higher (often over 50%) γ' volume fractions, which further shifts the operating temperatures higher [41]. For most cast alloys, the grain structure is equiaxed with large grains of millimetre size [33, 58]. Casting defects are often present as well as pronounced dendritic structures resulting in the precipitation of undesirable phases [58] and, eventually, dendritic fractures [59]. The presence of casting defects can be reduced by subsequent HIP treatment [60]. Due to the high volume fraction of γ', the volume fraction of the matrix is decreased, which limits the alloying by elements partitioning to the matrix, such as Cr, Mo or W. Special attention should be paid to a lower amount of Cr, resulting in the loss of oxidation resistance as well as hot corrosion resistance [41, 42]. Although oxidation resistance may be enhanced by a higher amount of Al, the application of coatings is necessary to prevent corrosion cracking at high temperatures. The coatings usually have a detrimental effect on mechanical properties [61], new types of coatings, however, show promise as shown by Šulák *et al.* [62]. Mechanical properties in a desired direction may be enhanced by directional solidification, resulting in columnar grain structure, or by a complete absence of grain boundaries in single-crystal alloys, suppressing thus the evolution of creep damage along the grain boundaries. A typical application of cast alloys with directional microstructure is turbine blades [42].

In other applications, e.g., turbine discs, the operating temperatures are lower. Hence, the γ' volume fraction can be lower and a good compromise between the corrosion resistance and the operating temperature can be achieved by forging. Wrought alloys typically contain

a significant amount of Cr (usually around 20%), Co and Mo [41–42]. Forgeability decreases with an increasing amount of Ti and Al [46]. The high-temperature performance is limited by the volume fraction of γ', which reaches, with some exceptions, about 50% at maximum [42]. The resulting microstructure contains equiaxed grains with grain size at a scale of tens or occasionally lesser hundreds of micrometres [63]. After forging, optimal properties are generally achieved by precipitation hardening [46].

Closer control of microstructure as well as waste management is offered by powder metallurgy. Due to the processing costs, powder metallurgy is only used when the component cannot be produced using traditional casting [46]. Using powder metallurgy, some special microstructures can be produced, such as oxide-dispersion-strengthened superalloys [64]. The components produced by HIP (plus possibly forging) exhibit very fine, uniform grain size, lack of segregation and thus a lesser number of undesirable phases. On the other hand, the extruded components exhibit crystallographic texture [64]. General problems include the occurrence of oxide and ceramic inclusions and porosity due to increased gas content [46]. AM techniques use powder to produce near-net shape components via layer-by-layer fabrication from a digital 3D model. The most common technique for manufacturing of metallic parts is laser powder bed fusion. The resulting microstructure is hierarchical, comprising dislocation cells, and exhibits a strong crystallographic texture. The dislocation cells are accountable for superior static properties due to hindering the dislocation movement [65]. Some AM superalloys require additional precipitation hardening treatment [66].

The most commonly performed heat treatments of nickel-based superalloys include stress relieving, solution annealing and precipitation (age) hardening. Stress relieving is confined to non-age-hardenable alloys. Its purpose is to relieve residual stress, which might be significant in welded or complex-shaped components. The applied temperatures are usually below the annealing or recrystallization temperatures. Solution annealing intends to dissolve undesirable phases and homogenize the chemical composition. It is often placed before the subsequent precipitation hardening as it also recrystallizes an inherent wrought structure. Therefore, the applied temperatures reach between 1000–1200 °C for most alloys, with a rather short duration of up to 4 hours [46]. The purpose of precipitation hardening (ageing) is to introduce strengthening phases into the microstructure, primarily the γ' phase, but other phases such as carbides occur as well due to the temperature range of precipitation hardening. Typical ageing treatment is performed at about 700–1080 °C for several hours (e.g., 16 hours for IN939 superalloy [67]). For some alloys, the ageing consists of several steps, resulting in a multimodal precipitate structure [67]. Careful optimization of the process parameters is needed to avoid the precipitation of TCP and other undesirable phases. Stabilizing treatment is often placed between solution annealing and ageing [46].

2.2.2 Room temperature fatigue

At low and room temperatures, precipitate shearing is considered by some authors [68–69] as the primary deformation mechanism since the precipitates are closely spaced and coherent. Since the dislocations are restricted to the primary {111} planes, cross-slip is limited, and the occurrence of the immobile dislocation locks is rather scarce [22, 43]. The maximum stress induced by cyclic straining either saturates (as for Waspaloy superalloy [70]) or reaches a maximum followed by cyclic softening (as for René 41 [34] or René 88DT [52] superalloys). The exact nature of cyclic stress evolution depends on several factors, mainly the internal stress state, the microstructure, the strain rate and the applied plastic strain amplitude. Observed hardening behaviour is most probably due to an increased dislocation density and becomes more pronounced at high strain amplitudes due to the activation of secondary slip systems. Moreover, the density of slip bands increases with increasing strain amplitude, resulting in more

slip plane intersections and hence reducing the effective mean free path of dislocations. Consequently, the internal stress as well as the maximum stress reached during the test is increased [22]. A higher density of slip bands is projected in the spacing of PSMs, hence more cracks are initiated [33]. In IN718, microtwinning was reported [68]. Hardening ceases once an equilibrium number of slip bands is formed. Cyclic saturation and cyclic softening arise as the consequence of the localization of plastic strain to the soft PSBs, which are for superalloys typically planar, and precipitate shearing [22]. Merrick [69] suggested that the intensive shearing of γ' by PSBs leads to a gradual dissolution of γ'. On the other hand, Antolovich and Lerch [22] argued that rather than complete dissolution, shearing of γ' results in a gradual decrease in the effective precipitate size within the active slip plane, possibly reaching a complete shear of the precipitate, which thus imparts no further resistance to the dislocation motion. Stoltz and Pineau [71] found that should the precipitates be too large to be sheared, Orowan looping prevails and the character of the slip is rather wavy. Consequently, the softening by shearing the precipitates does not occur and the work hardening is more pronounced. In γ''-strengthened alloys, a phase transformation of the γ'' phase to the δ phase was suggested as a complementary softening mechanism [68].

Three typical sites for fatigue crack initiation were identified: PSMs, carbides and casting defects. Initiation from carbides can be observed in the case of large surface or subsurface carbides [72]. Initiation from casting defects, resulting in defective fracture, often prevails in cast alloys [59]. However, the fatigue cracks initiate predominantly from PSMs [33, 70, 73]. As the PSMs form early in the fatigue life, so do the first microcracks [34, 73]. The consequent growth of the microcracks follows the active crystallographic plane until it reaches a grain boundary. Later, the crack path usually gradually deviates under the influence of normal stresses to the direction perpendicular to the applied stress. The crack propagation is thus usually transgranular [33]. At high strains, when multiple slip systems are activated, the cracks often change the cracking plane [22]. With decreasing strain amplitude, the occurrence of PSBs is more often confined to microstructural heterogeneities causing local stress concentrations, which results in local stress exceeding critical shear stress. The heterogeneities considered may include large-angle grain boundaries, favourably oriented grains, inclusions or twin boundaries [74]. Crack initiation was widely reported both on twin boundaries and near-surface defects, typically non-metallic inclusions [75–76]. The PSBs arise at the twin boundaries since the twin boundary plane is the slip plane as well. Hence, the dislocations on the aligned slip plane can travel large distances under the influence of the stress concentrations having arisen due to the twin, as explained by Heinz and Neumann [77]. The authors consider the localization in the near-twin PSB stronger than in general PSBs. PSBs at twin boundaries were reported also in the LCF regime, however, cracking along them is scarcer since the stresses are high enough to initiate the cracks at other PSMs.

Due to the slip planarity, the PSBs are narrow (tens of microns at maximum). Internally, a random distribution of planar dislocation arrays within a PSB was observed [22], indicating a slip inhomogeneity within a PSB. Dislocations typically move in pairs, indicating shearing of the γ' precipitates. A ladder-like PSB structure, similar to the one observed in simple fcc metals [9], was reported in cyclically strained IN713LC superalloy by Petrenec *et al.* [78], however, further evidence is missing.

Room temperature LCF properties are mostly affected by grain size and precipitate size. Higher flow stress and cyclic strength are generally achieved by finer grain size, contributing to the overall strength via Hall-Petch strengthening [42]. Static flow stress increases proportionally to the precipitate size up to the point when the precipitate shearing is not energetically favourable. The “ideal” γ’ precipitate size requiring maximum shear stress to be

overcome is marked by a transition from shearing by weakly coupled dislocations to strongly coupled dislocations. This value is different for each superalloy depending on its chemical composition. A transition to Orowan looping appears at an even higher precipitate size [79]. The resulting deformation is more homogeneous due to the higher waviness of the slip, and the work hardening is more pronounced since the precipitates are not shearable. More homogeneous deformation is manifested in lower density of slip bands and thus retardation of crack initiation. However, since the stresses are kept high due to a less significant softening, the crack propagation rate is higher in comparison to alloys with shearable precipitates [22, 43].

2.2.3 High-temperature fatigue

At high temperatures, material interaction with the environment plays a significant role and is further complemented by creep mechanisms. The LCF lifetime is thus determined by an interaction of slip mechanisms with oxidation and creep [43].

Deformation mechanisms evolve with an increase in temperature, promoting cross-slip, which is due to the dislocation locks becoming mobile. With the temperature increase, the dislocation structures become more homogeneous, and the dislocation density becomes lower due to increased mobility of dislocations, which are thus able to accommodate the applied plastic strain at a lower number of cycles. Slip bands may still be observable but are scarcer and not well-defined. The formation of planar slip bands, however, indicates that shearing of the coherent precipitates still occurs [22]. Since the slip band intersections are scarcer, the resulting deformation behaviour often comprises cyclic softening from the beginning of the fatigue test [68, 80–81]. In some alloys, however, the cyclic response is stable [82–83] and cyclic hardening might occur [33].

As the temperature increases, the environment is increasingly damaging. When the oxide layer forms at the component surface, high stresses arise due to material integrity and crack the brittle oxidic phase relatively easily. High stress at the crack tip results in the crack propagation into the superalloy, hence the corresponding propagation mechanism is referred to as stress-assisted grain boundary oxidation [84–85]. The cracks initiate at structural inhomogeneities, such as PSMs, secondary phases and, most often, oxidised grain boundaries. Lerch *et al.* [70] observed crack initiation at the intersections of oxidised slip markings with grain boundaries. Oxygen penetrates along the grain boundaries and forms oxidic grain boundary intrusions ahead of the crack tip, causing dynamic embrittlement [86–87]. Consequently, intergranular cracking is dominant, and the oxide layer is found on the crack surfaces. The extent of oxide penetration increases with the applied stress. Intergranular damage is further promoted by cavitation at grain boundaries, providing voids for oxygen to diffuse to, altogether resulting in the dominance of intergranular crack propagation mode [22]. Preferential oxidation of secondary phases has also been reported [85]. To prevent the occurrence of grain boundary oxidation mechanism, coatings are applied [62].

Based on the temperature and alloy composition, deformation-assisted coarsening and subsequent coalescence of γ' precipitates might occur. Coarsening of γ' promotes softening behaviour as it provides a larger mean free path for dislocation motion and favours Orowan looping rather than precipitate shearing, provided the precipitates are too large to be sheared. Coarsening occurs at high temperatures and low strain rates and its degree depends, above all, on the matrix/precipitate lattice misfit [22], hence more rapid changes can be expected in alloys with higher misfit [43]. Since the dislocations provide easy diffusion paths, the coarsening rate is greatly accelerated by cyclic straining [81], or creep load, resulting in a rafted structure [88]. The role of coarsening can be beneficial as the coarsening decreases the stress response while increasing ductility, which results in prolonged fatigue life. This is mainly due to the prolonged

crack initiation phase of the oxide spikes on the surface under the effect of lower stresses, as stated by Antolovich *et al.* [81]. If the *γ'* precipitates are sufficiently small, so that the coarsened precipitates can still be sheared, hence requiring higher stresses, the material may harden [22].

At intermediate temperatures (~400 °C), the strain ageing effect occurs in several alloys [70–71], increasing the cyclic stress. It is linked with a pronounced increase in dislocation density and the number of slip bands. The true reason for the occurrence of strain ageing has not been resolved [89–90].

Exposure to temperatures close to the ageing temperature may result in the precipitation of undesirable phases, typically a TCP *σ* phase. The occurrence of *σ* crystallites is detrimental to the mechanical properties of superalloys thanks to their acicular form. Precipitation can be minimized through careful compositional control [22]. On the other hand, precipitation of carbides, which occurs at temperatures above 700 °C and which is more pronounced at high strain rates [91], can be beneficial as they primarily precipitate at grain boundaries, mechanically hindering grain boundary sliding. Carbides can also positively affect the cyclic stress response as they represent an obstacle to dislocation motion. If, however, the precipitation at the grain boundaries is too frequent, a film can be formed which imparts embrittlement on the superalloy [92]. Increased susceptibility to environmental attack due to carbides at grain boundaries was reported by McMahon [85]. Carbide precipitation can also occur in other dislocation-rich regions, typically slip bands [70], thanks to the easy diffusion paths along the dislocation cores.

There are several factors affecting the high-temperature performance of a superalloy. As mentioned earlier, the key parameters are the chemical composition of an alloy and the utilised processing technology. The most profound effect has the grain size, which is typically in the range of millimetres for cast alloys, and which controls the extent of creep damage by cavity nucleation, growth and coalescence at grain boundaries. Thermal stresses are significantly reduced in a <001> direction, which is utilised for the production of directionally solidified and single-crystal turbine blades [43]. Even small deviations from a <001> direction significantly affect the resulting creep properties [93]. The effect of individual alloying elements is listed in Table 1. Another important factor is the volume fraction of *γ'* precipitates, which increases material strength at a given strain amplitude as shown by Miner *et al.* [63]. It has been shown recently [94] that interaction of matrix solutes with crystal defects such as dislocations influences the dominant deformation mode via altering the local microstructure, which may result in the rafting and precipitation of TCP phases. Segregation of solutes at dislocations may occur as early as at 750 °C [95]. Precipitation of carbides is positively influenced by the loading frequency [91].

3 Aim of the thesis

The thesis aims to clarify the fundamental damage mechanisms leading to the initiation of cracks in nickel-based superalloys subjected to fatigue loading. The topic of fatigue damage and the initiation of fatigue cracks has been studied for a long time. The case of simple one-phase materials such as pure copper or aluminium is quite well described in numerous sources [2, 4–5, 96–97], however, the explanations of observations differ. Several models (see e.g. [9, 24–32]) have been proposed in past but the scientific community is not unanimous on the topic yet.

Engineering materials are usually much more complicated in terms of structure, which is directly related to the fatigue response of the material and the damage mechanisms responsible for possible premature failure of various components. Even if there are many sources, e.g. [43, 69–70, 98], discussing the relevant damage mechanisms in complex engineering materials such as nickel-based superalloys, a satisfying explanation dealing with how the fatigue cracks initiate has not yet been presented. The material of interest in this study is a wrought nickel-based superalloy René 41. Although high-cycle fatigue properties of the alloy are known for years [99], material behaviour under high cyclic stresses introducing plastic strains has not been to the author's knowledge studied.

The objectives are as-follows:

- characterization of low-cycle fatigue behaviour of a chosen nickel-based superalloy – René 41 – in both solutionised and precipitation-hardened (aged) states,
- comparison of relevant damage mechanisms at room and elevated temperature (800 °C),
- clarification of the influence of the localization of plastic strain on the occurrence of fatigue cracks and fatigue fracture in general,
- finding the relation between the stress-strain response of the material on one hand and the microstructural changes and related damage mechanisms on the other,
- clarification of the role of defects on the fatigue crack initiation in nickel-based superalloys,
- studying the evolution of plastic strain localization into persistent slip bands,
- analysis of cyclic plasticity using the statistical theory of the hysteresis loop.

4 Experimental

4.1 Material – Ni-based superalloy René 41

René 41 (René is a trademark of General Electric Company) is a precipitation-hardened superalloy which exhibits high strength at high temperatures. It is commonly used in the most thermally exposed parts of jet engines and missile components [100], such as turbine disks or exhaust nozzles, due to its microstructural stability at high temperatures, high corrosion, and creep resistance. According to the technical guide by Donachie and Donachie [46], René 41 is commonly used at temperatures up to 760 °C, however, some authors [101] report a use up to 815 °C for long exposures and up to 980 °C for short exposures. Its main disadvantage is a tendency to crack under high contact stresses due to its low plasticity at high temperatures which is promoted by a high content of alloying elements and related segregation during conventional casting. René 41 can be welded in the solutionised state when the plasticity is larger [101]. Some selected mechanical and physical properties are listed in Table 2.

The material tested in the present study was supplied by VDM Metals in the form of a cylindrical bar of 12 mm in diameter. The chemical composition analysed using optical emission spectroscopy (OES) by the supplier was complemented by an additional measurement using the OES technique in the as-received state as shown in Table 3. Note that nitrogen content was not evaluated due to the technical limitations of the spectroscope. The material was tested in two thermodynamical states: solutionised, and solutionised and precipitation-hardened, further labelled as aged for the sake of simplicity. Solution heat treatment was performed at 1060 °C for 1 hour, followed by cooling in air. Solution heat treatment was performed to dissolve the undesirable phases and reach a homogeneous distribution of elements and maximum ductility. Precipitation hardening (aging), introducing the γ' precipitates to the microstructure, was performed following the recommendation from [46] at 760 °C for 16 hours, followed by cooling in air. Specimens for interrupted fatigue testing were aged in a vacuum and cooled in the furnace to achieve a larger precipitate size, which provided better contrast for precipitates in lamellae for TEM observation.

Table 2. Selected properties of René 41 superalloys according to [46].

Density	Incipient melting temperature	γ' solvus	Rupture strength at 760 °C	Rupture strength at 870 °C	Mean coefficient of thermal expansion	Loss in diameter at 870 °C
8.25 g/cm^3	1230 °C	1050 – 1070 °C	345 MPa	115 MPa	$15.6 \cdot 10^{-6}$ K	0.3 mm

Table 3. Comparison of the theoretical and real chemical composition of René 41 superalloy. Note that N content was not evaluated due to the technical limitations of the OES equipment.

	Ni	Cr	Co	Mo	Ti	Al	Fe	C	Si	Other
Ref. [46]	55.00	19.00	11.00	10.00	3.10	1.50	<0.30	0.09	-	0.01 B
OES by supplier	54.83	18.37	10.40	9.34	3.23	1.57	1.89	0.07	0.04	<0.03 B, Bi, Mn, Pb, S, Se, Zr
OES	53.22	18.30	11.04	10.13	2.90	1.68	1.87	0.07	0.07	0.17 Cu, 0.20 Nb, 0.13 W, 0.10 V, <0.05 B, Mn P, S, Zr

4.2 Methods

4.2.1 Test specimen preparation

Specimens were machined from the bars to a cylindrical shape with dimensions specified in Fig. 4.1. The gauge length was mechanically ground, polished with a diamond compound (down to a size of 1 μm) and electrochemically polished to acquire a mirror-like surface suitable for electron microscopy observations. Electropolishing conditions are listed in Table 4. The preparation of a smooth surface of aged René 41 superalloy proved to be challenging as fine Mo-rich carbides at grain boundaries were attacked by an electrolyte primarily. None of the solutions suggested by the ASM metallography handbook [102] led to a perfectly flat surface, usually leaving dimples on the surface as shown in Fig. 4.2a. The least damage to the surface was imposed by a solution of methanol, nitric acid and perchloric acid. Aged specimens were finally manually polished with colloidal silica to remove the dimples (see Fig. 4.2b).

Table 4. Electropolishing conditions.

René 41	Electrolyte (volume ratio)	T (°C)	U (V)	t (s)
Solutionised	93.9 CH_3CH_2OH + 1.4 HNO_3 + 4.7 $HClO_4$	-16	54	5
Aged	93.9 CH_3CH_2OH + 1.4 HNO_3 + 4.7 $HClO_4$	5	20	4

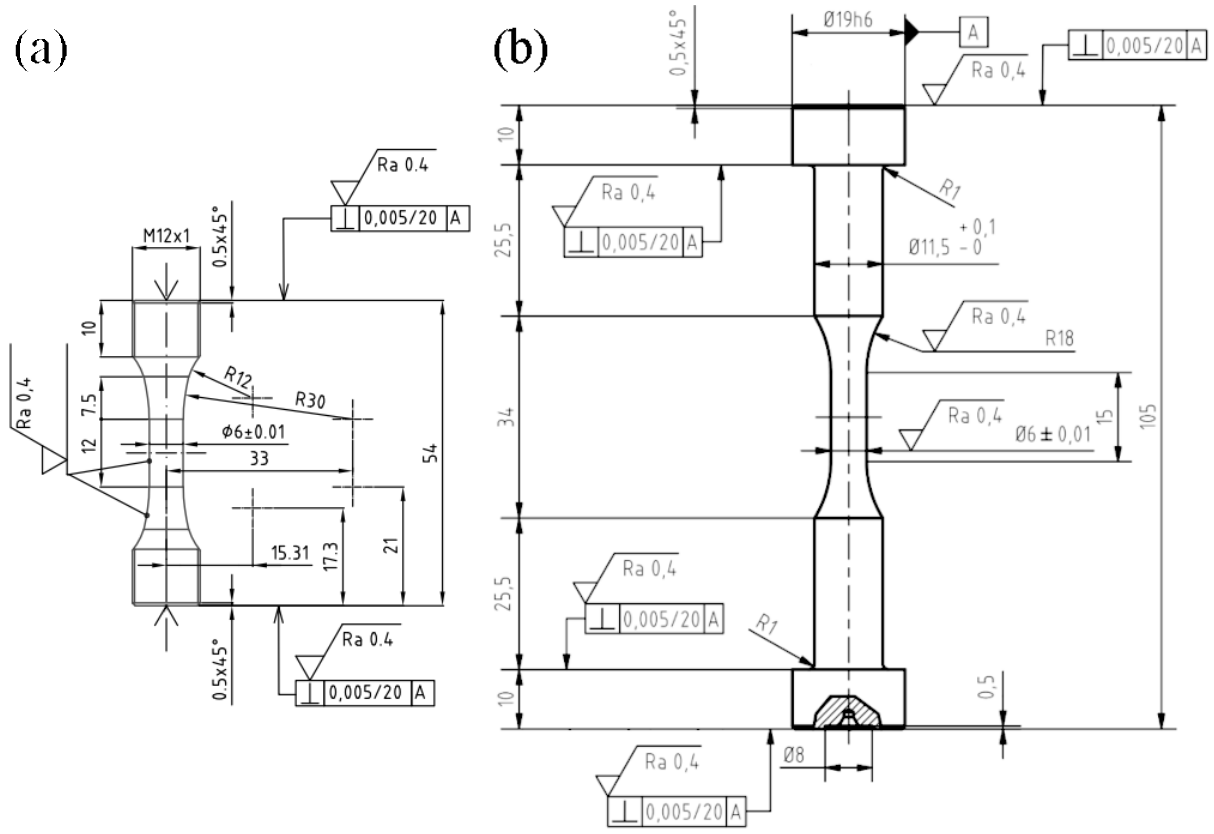

Fig. 4.1. Engineering drawings of specimens for (a) room temperature and (b) high temperature tests.

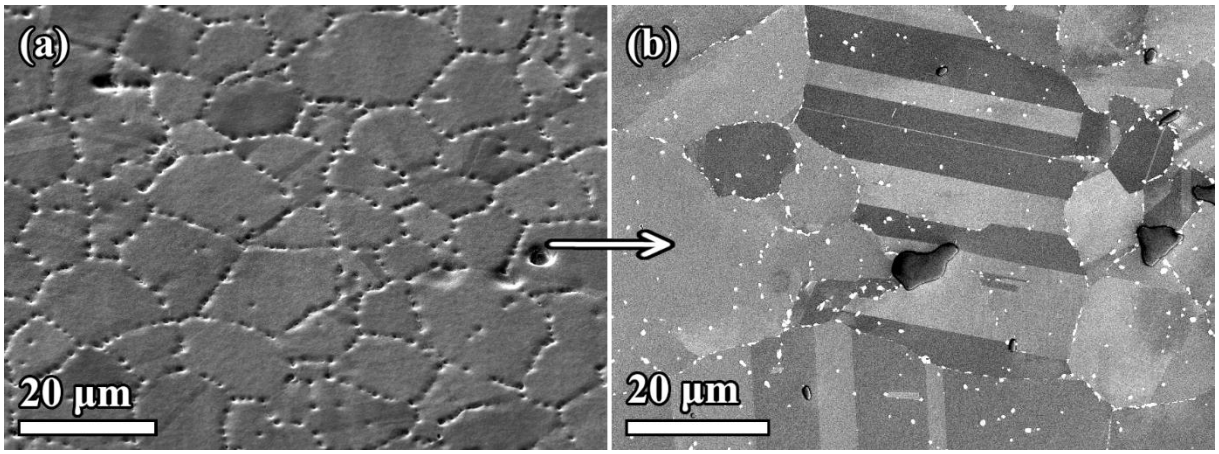

Fig. 4.2. SEM micrographs showing specimen surface of aged René 41 superalloy (a) after electropolishing and (b) after additional manual polishing with colloidal silica.

4.2.2 Mechanical testing

Fatigue tests were performed in laboratory air using the computer-controlled servohydraulic testing machine MTS 880. Servohydraulic testing machine MTS 810 with a furnace was utilised for high-temperature testing (up to 1000 °C). Specimens were subjected to fully-reversed, uniaxial cyclic straining (R = -1) at a constant strain rate of $2 \cdot 10^{-3}$ s^{-1} at room temperature and elevated temperature of 800 °C, which represents the most demanding conditions for the tested material. The test temperatures were chosen to study relevant cyclic deformation behaviour and fundamental damage mechanisms with and without the high-temperature effect. All tests were performed in strain control with constant total strain amplitude. The total strain amplitudes are listed in Table 5 and were chosen so that the resulting lifetimes approximately cover the range of 500–20000 cycles. The strain was measured longitudinally using an MTS contact axial extensometer for LCF testing. In the case of room temperature tests, the extensometer with a gauge length of 8 mm was attached to the specimen gauge length using metallic springs around the gauge diameter. In the case of high-temperature tests, the extensometer with a gauge length of 12 mm was placed outside the furnace and attached to the specimen gauge length using air-cooled alumina extension rods. In each cycle, 2000 data points were recorded for data analysis. Data postprocessing, including numerical differentiation of the experimentally obtained hysteresis loops, was performed using the dedicated software Derivace, specifically designed by Jiří Tobiáš. Fatigue lifetime was evaluated using the criterion

$$k_{cr} = \frac{\sigma_m}{\sigma_a} \leq -0.3. \tag{4.1}$$

Table 5. Fatigue test conditions adopted in the present study.

René 41	T (°C)	ε_a (%)
Solutionised	23	0.5, 0.8, 1.0, 1.2
Aged	23	0.5, 0.8, 1.0, 1.2
Aged	800	0.23, 0.35, 0.5, 0.8

4.2.2.1 Interrupted fatigue tests

Room-temperature fatigue tests cycled with ε_a = 0.8% were interrupted after the definite number of elapsed cycles to study microstructural changes using electron microscopy. Two types of interruptions were used, as depicted in Fig. 4.3. The solutionised specimen was interrupted at maximum compression strain (see Fig. 4.3a), followed by relaxation of the elastic

strain resulting in a stress drop to zero, while the plastic strain remained. The interruptions were performed after 1, 3, 10, 30, 100 and 500 cycles. The cycling after interruption continued from the end strain level (at zero stress) within the prescribed strain range ±0.8%. Interruptions to the aged specimen were enhanced as depicted in see Fig. 4.3b. To reach zero plastic strain, the test run was interrupted at a specific total strain, derived from an uninterrupted test run cycled with the identical total strain amplitude of ε_a = 0.8%. The interruptions were performed after 1, 10 and 100 cycles. This approach mitigated the disproportion between compressive and tensile plastic strains which might be significant in the first few cycles.

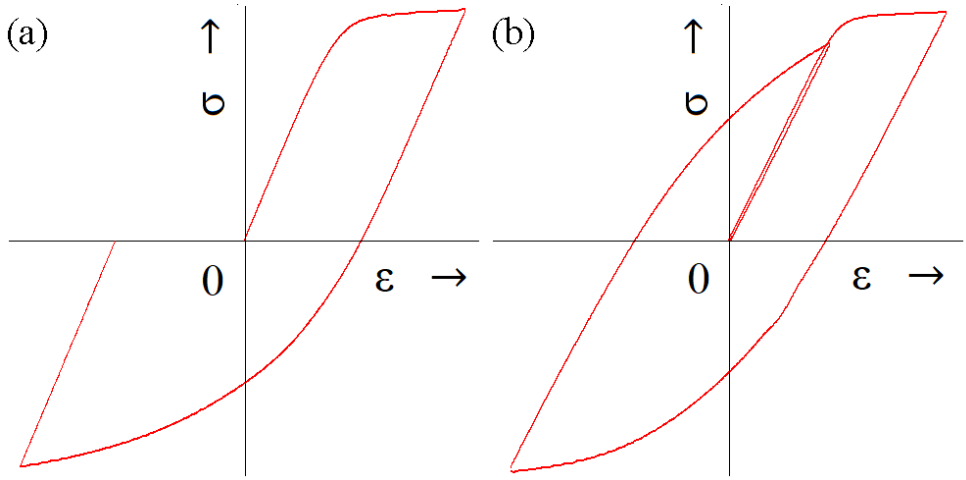

Fig. 4.3. Schematic illustration of the two types of performed interruptions. (a) Interruption at maximum compression strain was adopted for the solutionised specimen. (b) Interruption at 0% strain was adopted for the aged specimen.

4.2.3 Analysis of the hysteresis loop using the statistical approach

Analysis of the loop shape was performed using the statistical theory of the hysteresis loop. Experimental curves approximating probability density functions of critical internal stresses were derived from the second derivatives of relative stress to relative strain. In each point, numerical differentiation was performed by establishing the slope of a linear fit of the nearest 15 data points. Afterwards, the data were numerically smoothed by averaging the nearest 70 data points. Second derivatives of tensile and compressive half-loops for selected cycles were plotted in the form of $-\frac{2}{E_{eff}^2}\frac{\partial^2\sigma_r}{\partial\varepsilon_r^2}$ against fictive stress in the form $\frac{\varepsilon_r E_{eff}}{2}$. Effective moduli E_{ef} were evaluated for the respective cycles. Major peaks corresponding to the quantities of the second derivatives were fitted with the Weibull distribution function in the form

$$f(x) = C\frac{k}{\eta}\left(\frac{x-\theta}{\eta}\right)^{k-1}\exp\left(-\left(\frac{x-\theta}{\eta}\right)^{k}\right), \qquad x > \theta, \eta > 1 \tag{4.2}$$

where k stands for the shape parameter (k = 3), η for the scale parameter, C for the proportionality parameter and θ for the location parameter, which determines the threshold value of the fit. The fitting was performed in Python language using the least square procedure. The purpose of the fit was to derive initial effective stress σ_{e0} and saturated effective stress σ_{es}, which were approximated by a threshold value. Since the saturation of the stress amplitude was missing in most of the cases, σ_{es} was derived at half-life. The fit, and the determination of the respective parameters, appeared to be sensitive to the value of the shape parameter which was thus fixed to 3, which is equivalent to fitting with the Gauss distribution.

4.2.4 Electron microscopy observation

4.2.4.1 SEM observation

Specimen surfaces considered for observations using the methods of electron microscopy were carefully polished to acquire mirror-like surfaces. Firstly, the surface was mechanically ground using SiC grinding paper, followed by polishing using diamond compound down to a particle size of 1 μm, and final mechanical-chemical polishing using colloidal silica with a particle size of 0.04 μm. Eventually, the specimens were cleaned using an ultrasound cleaning system and Tergeo plasma cleaner.

Electron microscopy techniques were used for a detailed analysis of the initial material state and material after cycling. Overall damage as well as fracture surface and surface relief were observed using scanning electron microscope SEM LYRA 3 XMU FEG/SEM (SEM). The imaging was performed using an electron beam with an accelerating voltage of 10 kV. SEM images were captured in secondary electron contrast and/or back-scattered electron contrast. The SEM was equipped with a focused ion beam (FIB), utilised for mass imaging and cross-sectioning, energy-dispersive x-ray spectroscope Ultimmax (EDS) for local chemical analyses, and electron back-scattered diffraction detector Symmetry (EBSD) with AZtec software for grain size, grain and twin boundary identification and texture evaluation. The grain size and texture analyses using EBSD were performed on square areas of 1 mm^2 with a step size of 0.5 μm on specimen cross-sections under the electron beam with an accelerating voltage of 20 kV. Identical voltage was used also for EBSD analysis of grain and twin boundaries at the surface secondary cracks. The secondary crack analysis was performed on longitudinal sections over a length of 2 mm from the fracture surface.

4.2.4.2 FIB cross-sections and preparation of lamellae for TEM observation

FIB with high-energy gallium ions was utilised to mill out shallow cross-sections revealing the microstructural features underneath the specimen surface and to prepare thin lamellae for TEM observations from the specimen surface. Due to the microscope configuration, the specimens had to be tilted by 55° to produce the cross-sections, causing a distortion of true dimensions in the corresponding SEM micrographs. Both cross-sections and lamellae were oriented parallel to the loading axis (perpendicular to the surface), so the specimen/loading axis always lay in the cross-section/lamella plane. For the sake of uniformity, average-sized grains with a maximum size of 20 μm and PSMs approximately perpendicular (within a 15° deviation) to the cross-section plane were chosen.

To protect the surface from redeposition and ion damage during milling, a protective Pt layer was deposited by melting the Pt powder, which was then sprayed onto the surface by a gas injection system, using an electron beam and ion beam, subsequently. The electron beam deposition was performed at an accelerating voltage of 5 kV. The ion-beam-induced deposition (accelerating voltage 30 kV, probe current 150–200 pA) was followed by rough milling of the cross-section (30 kV, 4–10 nA), which was subjected to two-step polishing afterwards (rough polishing at 30 kV, 1 nA and smooth polishing at 30 kV, 100–200 pA). The resulting cross-sections were approximately 10–15 μm wide and 10 μm deep.

FIB+SEM tomography technique was used to observe the profiles of stage I microcracks along the PSMs. The basis of this technique is Pt layer deposition onto the larger area of interest, and FIB milling, which is utilised to produce a cross-section by the aforementioned procedure. Consequently, the material at the cross-section is continuously milled out by FIB and SEM images are taken. In this study, FIB milling was stopped, and the SEM images were taken after the material of an approximate thickness of 100 nm was milled out from the cross-section.

The lamellae production procedure is an extended version of the production procedure of the cross-sections. The surface was protected by a Pt layer deposited using electron and ion beams, subsequently. Lamellae were prepared by careful FIB milling at both sides of the area of interest, followed by cutting the lamella off the specimen bulk using J-cut, and lifting out *in-situ* using a micromanipulator. Afterwards, the lamellae were attached to a copper TEM grid and thinned down to ~100 nm by careful polishing. In addition to the polishing procedure described above, the lamellae were finally polished with low accelerating voltages (5 kV and finally 2 kV) to reduce ion damage and contamination. The resulting lamellae were approximately 10–15 μm wide, 10 μm deep and 100 nm thick.

4.2.4.3 TEM observation

Thin foils for TEM observations were prepared *post-mortem* from representative specimens cycled with ε_a = 0.5% using standard procedure. Approximately 3-mm-wide plates were cut from a specimen transversally to the specimen axis and thinned down to 70 μm by grinding on SiC grinding papers. Consequently, foils were produced from the plates by electrochemical thinning in a double jet device TenuPol2 using an electrolyte consisting of 70 vol.% methanol, 20 vol.% glycerine and 10 vol.% perchloric acid. The electropolishing was performed at 11.5V/-5 °C until the foil was sufficiently thin for TEM observation (~100 nm).

TEM technique was adopted for observations of the true surface relief and its relation to the underlying dislocation structure on the site-specific lamellae prepared by FIB, the observations of the dislocation structures and other related microstructural features on thin foils, and for particle analysis and analysis of the specimen crystallography. The presented TEM micrographs were captured in scanning mode (STEM) using JEOL JEM-2100F transmission electron microscope equipped with a double tilt holder and an EDS detector Oxford Instruments X-MAX 80, and Thermo Scientific Talos F200i equipped with a double tilt holder and with built-in EDS detector. The latter TEM microscope was also used for taking pictures in high resolution (HRTEM). HRTEM micrographs were taken exclusively in a <110> zone. Both microscopes were operated at 200 kV. Diffraction patterns and Kikuchi lines were used to determine the crystallographic orientation of the loading axis, foil/lamella, specific grains and related dislocation structures. Dislocation structures were further analysed with three different diffraction vectors. For particle analysis, at least three different diffraction patterns were analysed using the ICSD database of phases and JEMS software, and the connecting Kikuchi lines were compared with projections by JEMS software.

5 Results

5.1 Initial material state

After solution heat treatment, the microstructure contained equiaxed grains with annealing twins and no γ' precipitates as shown in Fig. 5.1, and contained carbides as well as carbonitrides as shown in Fig. 5.2. According to the EBSD analysis (Fig. 5.1a), no significant material texture was present in the loading direction, and the average grain size was 16.45 μm ± 12.89 μm (grain size 8.5 according to ASTM E2627) with grain sizes in the range 3.57 μm–108.68 μm (notice the relatively large grains in Fig. 5.1b). Initial dislocation content was low due to the performed heat treatment at a temperature sufficiently high to relax plastic deformation imposed during the forging process (see Fig. 5.1c).

EDS analysis, complemented by analysis of Kikuchi patterns and selected area electron diffraction (SAED) patterns in TEM, revealed several secondary phases. Relatively large, mostly spherical particles (up to 10 μm in diameter) found mostly within the grains were identified as cubic MC carbides enriched in Mo, Ti and Nb and depleted of Ni, Cr, Co and Fe relative to the matrix, and cubic Ti(C,N) carbonitrides with only a minor content of other elements such as V. The MC carbides were distinguished from the Ti(C,N) carbonitrides based on combined area and point analysis by EDS (see Fig. 5.2a–b), as the lattice parameters were similar. The finer particles (up to 1 μm) found both at the grain boundaries and within the grains were identified as cubic M_6C carbides (see Fig. 5.2c), which were enriched in Mo and depleted of Ni (see Fig. 5.2a) and some also depleted of Co and Fe, indicating that different types of M_6C carbides had precipitated.

After ageing treatment followed by cooling in air, the microstructure contained equiaxed grains with annealing twins (Fig. 5.3b) and spherical, coherent γ' precipitates (Fig. 5.3d–f) with typical cube/cube relationship $(01\bar{1})_\gamma$ // $(01\bar{1})_{\gamma'}$. According to the EBSD analysis (Fig. 5.3a), no significant material texture was present in the loading direction, and the average grain size was 11.76 μm ± 6.02 μm (grain size 9.8 according to ASTM E2627) with grain sizes in the range 3.57 μm–50.63 μm. The γ' precipitates formed during ageing treatment with subsequent cooling in the air exhibited an average precipitate size of 22.8 nm in diameter and volume fraction of 42.8% (Fig. 5.3d), estimated by image analysis from TEM micrographs. Heat treatment in a vacuum and subsequent cooling in a furnace yielded a different result, specifically, an average precipitate size of 98 nm and volume fraction of 32.6% (Fig. 5.3e). Similarly to the solutionised state, the initial dislocation density was low (Fig. 5.3c). Some dislocations were observed at secondary phase particles.

According to the STEM+EDS analysis complemented by diffraction analysis of selected patterns at particles and particle/matrix interfaces (see Fig. 5.4), ageing treatment induced changes also in the occurrence of secondary phases. The content of M_6C carbides was found to increase particularly at the grain boundaries (some of the white dots in Fig. 5.3b), while MC carbides and Ti(C,N) carbonitrides were scarcer in comparison to the solutionised state. As a by-product of ageing treatment, tiny (up to 300 nm) elongated cubic $M_{23}C_6$ carbides, enriched in Cr and Mo, co-precipitated at the grain boundaries with the M_6C phase. The $M_{23}C_6$ particles were analysed in the zone axis [111], in which the orientation relationship $(\bar{1}01)_\gamma$ // $(0\bar{1}1)_{M_{23}C_6}$ was observed. Furthermore, fine (up to 3 μm) spherical tetragonal M_3B_2 borides, enriched in Cr and Mo, were detected both at the grain boundaries and within the grains.

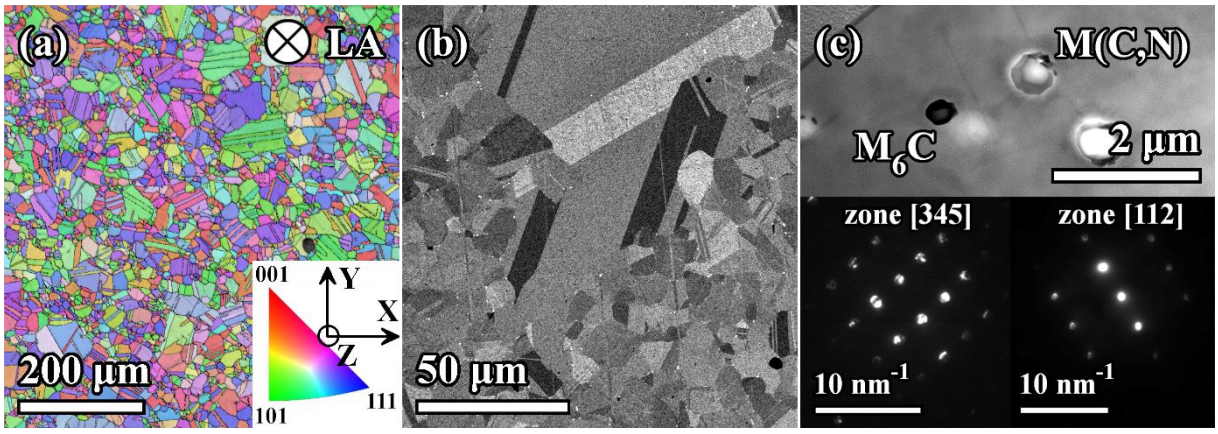

Fig. 5.1. Initial, γ' precipitate-free microstructure of solutionised René 41 superalloy. (a) EBSD IPFZ image revealing no significant material texture along the loading axis (LA). (b) SEM micrograph showing typical microstructure with equiaxed grains and some large grains up to about 110 µm in diameter, and frequent annealing twins. (c) STEM micrograph reveals low initial dislocation content. SAED on the particles suggested the presence of cubic Ti(C,N) or MC phase (right-hand inset), and cubic M_6C phase (left-hand inset).

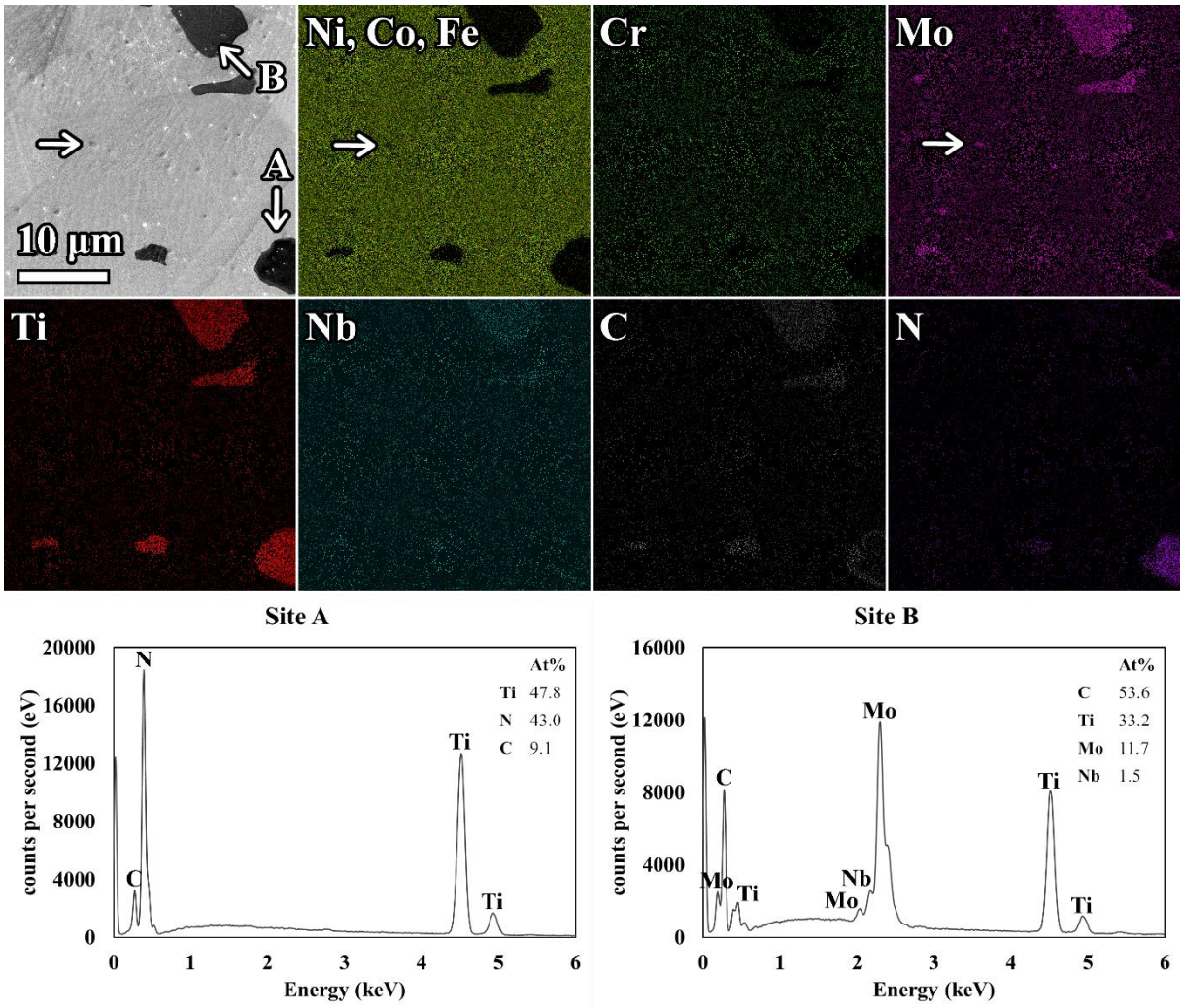

Fig. 5.2. SEM+EDS analysis of solutionised René 41 superalloy, distinguishing Ti(C,N) carbonitrides (site A) from MC carbides (site B) enriched in Mo, Ti and Nb, relative to the matrix. Notice the arrow pointing at a fine Mo-enriched particle (presumably M_6C carbide).

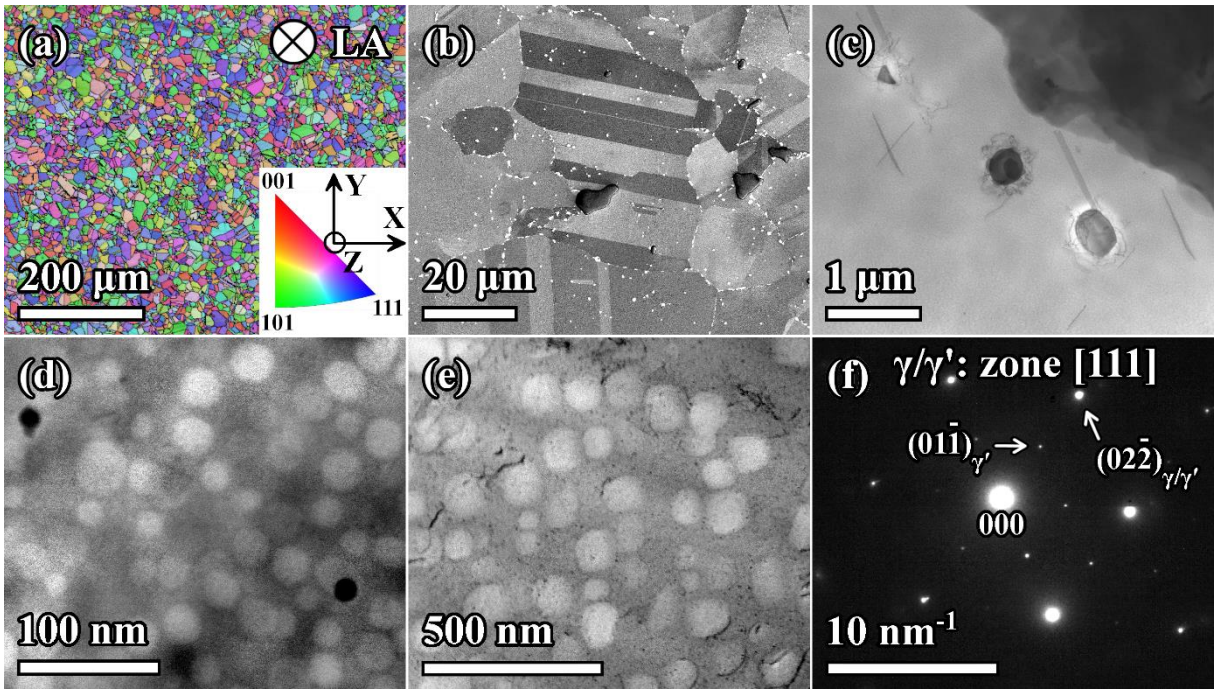

Fig. 5.3. Initial microstructure of aged René 41 superalloy. (a) EBSD IPFZ iamge revealing no significant material texture along the loading axis (LA). (b) SEM micrograph showing typical microstructure with equiaxed grains and occasional large grains up to about 50 µm in diameter, annealing twins and frequent occurrence of secondary phases precipitated due to the ageing treatment primarily at the grain boundaries. (c) STEM micrograph revealing the low initial dislocation in the material. Dislocations were observed mostly at the secondary phase particles. (d–e) STEM micrographs showing the comparison of precipitate sizes after (d) cooling in air and (e) cooling in a vacuumed furnace. (f) SAED on a *γ/γ'* interface with a typical cube/cube relationship between the *γ* matrix and the *γ'* precipitates in the zone axis [111].

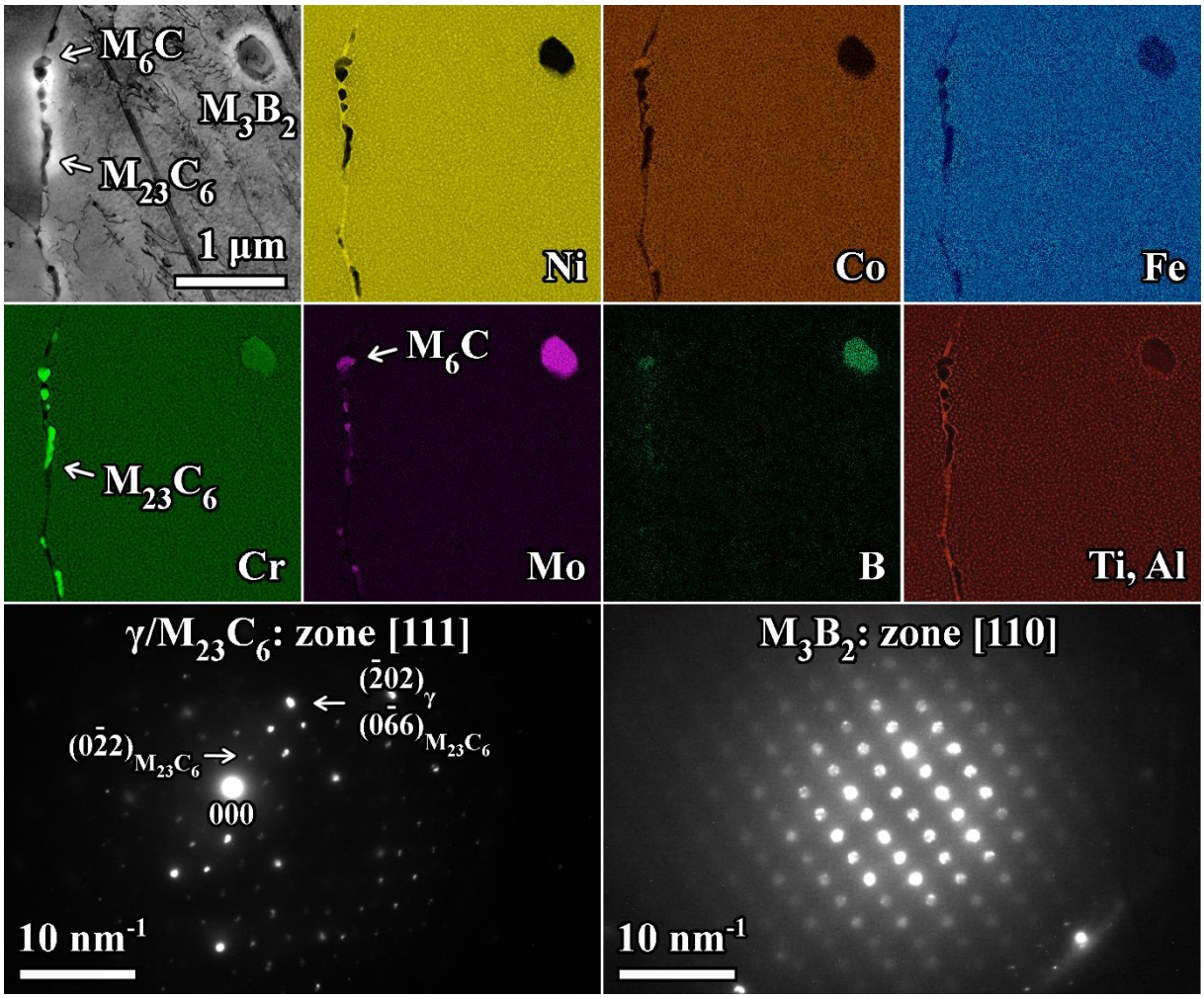

Fig. 5.4. STEM+EDS analysis of a grain boundary area of aged René 41 superalloy, complemented by SAED analysis at the particles and particle/matrix interfaces, revealing grain boundary precipitation of fine Mo-rich M_6C carbides and fine Cr-rich $M_{23}C_6$ carbides with typical orientation relationship to the γ matrix in the zone axis [111], and spherical Mo-rich M_3B_2 borides. Boron was found to partition also to M_6C carbides. Note that carbon was not evaluated due to foil contamination.

5.2 Lifetime and cyclic response

5.2.1 Room temperature fatigue loading

Lifetime data from the tests conducted at room temperature (RT) are shown in Table 6. Lifetimes were evaluated using the k_{cr} criterion shown in Eq. (4.1). Due to missing saturation plateau (see cyclic hardening/softening curves in Fig. 5.6), stress amplitude was evaluated at half-life and plastic strain amplitude was derived from the width of the half-life hysteresis loop at mean stress. Fig. 5.5a shows a plot of half-life stress amplitude $\sigma_{a,50\%Nf}$ vs. double lifetime $2{\cdot}N_f$. The experimental points were fitted by Basquin's law

$$\sigma_a = \sigma_f'\left(2N_f\right)^b \tag{5.1}$$

where σ_f' stands for fatigue strength coefficient and b for fatigue strength exponent. The values were evaluated by regression analysis using the least squares approach and are listed in Table 7. The plot clearly shows that in stress cycling, which is of interest from the application point of view, the aged material performs markedly better. In strain cycling, however, the solutionised material achieves higher lifetimes (compare in Table 6) which is connected to lower stress levels. Fig. 5.5b shows a plot of half-life plastic strain amplitude $\varepsilon_{ap,50\%Nf}$ vs. double lifetime $2{\cdot}N_f$. The experimental points were fitted by Coffin-Manson's law

$$\varepsilon_{ap} = \varepsilon_f'\left(2N_f\right)^c \tag{5.2}$$

where ε_f' stands for fatigue ductility coefficient and c for fatigue ductility exponent. The values were evaluated by regression analysis using the least squares approach and are listed in Table 7. As follows from the plot, the solutionised material attains higher levels of plastic strain amplitude at half-life. The resulting hysteresis loops in the aged state are, in comparison to the solutionised state, notably narrower, indicating lower plastic strain amplitudes (compare Fig. 5.7a to Fig. 5.9a). The difference in attained plasticity at half-life becomes bigger at lower imposed strains. It is illustrated by different slopes of the fitting curves. Flow stress is higher for the aged material as shown by cyclic stress-strain curves in the representation of half-life stress amplitude $\sigma_{a,50\%Nf}$ vs. half-life plastic strain amplitude $\varepsilon_{ap,50\%Nf}$, shown in Fig. 5.5c. The experimental points in the plot were fitted by a power law in the form

$$\sigma_a = K\varepsilon_{ap}^n \tag{5.3}$$

where K is an experimentally determined material constant and n stands for cyclic strain hardening exponent. The values were evaluated by regression analysis using the least squares approach and are listed in Table 7.

Plots in Fig. 5.6 show cyclic hardening/softening curves in representations of both stress amplitude σ_a and plastic strain amplitude ε_{ap} vs. the number of cycles N. A general feature of both material states is the absence of a saturation plateau in the range of tested strain amplitudes. Solutionised René 41 (Fig. 5.6a) exhibits initial cyclic hardening which becomes more pronounced and tends to culminate earlier with increasing strain amplitude. The initial hardening is then followed by gradual cyclic softening until fracture. Both the stress amplitude and the width of the hysteresis loop (and hence the plastic strain amplitude, see Fig. 5.7a) at half-life are more or less the same as in the first cycle. On the other hand, aged René 41 (Fig. 5.6b) exhibits no or negligible cyclic hardening (maximum increase in cyclic stress amplitude is 30 MPa for ε_a = 1.2% which constitutes a 2.5% increase), the dominant feature is gradual cyclic softening until fracture. Hence, there is a notable decrease in stress amplitude accompanied by a widening of the hysteresis loop (see Fig. 5.9a).

For the sake of comparison of softening behaviour of the two tested states, softening ratios *SR* were evaluated

$$SR = \frac{\sigma_{a,max} - \sigma_{a,50\%N_f}}{\sigma_{a,max}} \cdot 100\ (\%) \tag{5.4}$$

where $\sigma_{a,max}$ stands for maximum stress amplitude attained over the fatigue test and $\sigma_{a,50\%Nf}$ for stress amplitude at half-life. The values are listed in Table 7. In both states, the softening ratio is lowest for the lowest strain amplitude (ε_a = 0.5%), which is mostly realised in the elastic region. At higher strain amplitudes, the softening ratio oscillates around 11% and 12% for the solutionised and the aged state, respectively.

Analysis of the loop shape using the statistical theory of the hysteresis loop was performed on specimens cycled with ε_a = 0.8%. The analysis showed that solutionised material (see Fig. 5.8) exhibited a single major peak in the second derivative. In both tension and compression, the peak is shifted from about 500 MPa towards higher fictive stress in the first 30 cycles and shifted back towards lower values in the remaining fatigue life. The height of the peak was found to decrease with increasing fictive stress. Effective stresses were evaluated using the fit by Weibull distribution function in the first cycle for initial value σ_{e0} and at half-life for saturated value σ_{es}. The fit is illustrated in half-life charts by the dotted line as shown in Fig. 5.7b, the fit for the first cycle, as its importance is lower, is not shown to keep the respective charts clear. For solutionised material, both initial and saturated effective stress were around 100 MPa, as shown in Table 8, for both tensile and compressive half-loops. On the other hand, the aged material (Fig. 5.10) exhibited two major peaks in the first cycle. However, the second peak occurring at higher fictive stress at about 1450 MPa vanished quickly, with only a small peak left after 10 cycles before vanishing completely as apparent from the plot of the 100th cycle. The first peak at about 850 MPa became dominant, and continuously shifted towards lower fictive stress, and its height increased throughout the fatigue life, accordingly to the observed gradual cyclic softening until fracture. On a qualitative basis, there was little difference between tension and compression. The effective stress corresponding to the first peak developed from about 300 MPa in the first cycle (in both tension and compression) to about 200 MPa and 280 MPa at half-life for tension and compression, respectively.

5.2.2 High temperature (800 °C) fatigue loading

Lifetime data from the tests conducted at elevated temperature (800 °C) are summarised in Table 6. Note that at chosen testing temperature, it makes sense to investigate only the aged material since the ageing temperature for René 41 is 760 °C. In comparison to the aged material subjected to room temperature fatigue, cyclic stresses are reduced (see Fig. 5.5a). The performance gets worse in both stress (Fig. 5.5a shows that the 800 °C curve lies generally below) and strain cycling (compare the lifetimes in Table 6). For instance, comparing the aged specimens cycled with ε_a = 0.8%, the lifetime decreased tenfold. This is further complemented by lowering the flow stress (see Fig. 5.5c). The diagram in Fig. 5.5b shows there is also a significant drop in the number of cycles to failure at a given plastic strain amplitude. The resulting hysteresis loops (Fig. 5.11a) show a decrease in stress amplitude at half-life, however, the width of the loop did not witness any notable change.

The character of the overall cyclic stress response over cycling is similar at elevated and room temperatures. At relatively high strains ($\varepsilon_a \geq$ 0.5%), cyclic softening is dominant from the early stages of life until fracture. No cyclic hardening in the first few cycles was observed. With decreasing plastic strain, the cyclic response rather tends to saturate and remain so until fracture, which can be seen for ε_a = 0.23% in Fig. 5.6c.

Analysis of the loop shape using the statistical theory of the hysteresis loop was performed on a specimen cycled with ε_a = 0.8% (Fig. 5.11 and Fig. 5.12). From the first cycle throughout the fatigue life, two major peaks in the second derivative occurred. This contrasts with fatigue loading at RT, which witnessed a swift vanishing of the second peak occurring at higher fictive stress. The occurrence of the two peaks indicates the deformation of the two dominant phases in René 41 superalloy, namely the γ matrix and the γ' precipitates, and the effective stresses were thus derived for both in the first cycle and at half-life. Furthermore, the initial drop of the second derivative was shifter towards higher fictive stress in comparison to the room temperature data. The first peak at about 600 MPa in the first cycle gradually shifted towards lower fictive stress (about 500 MPa at half-life), and the peak became increasingly pronounced. The position of the peak and character of the shift was more or less identical for both tensile and compressive half-loops. The position of the second peak, on the other hand, was in the first cycle substantially different in tension (~1200 MPa) and compression (~1000 MPa). In compression, the second peak was dominant in the first cycle, but gradually shifted towards higher fictive stress (~1150 MPa) and decreased so that its height was in the end lower than that of the first peak. In tension, the second peak was higher and far less dominant, however, it also decreased and stabilized at about 1150 MPa. The effective stresses corresponding to the first peak, estimated using the fit by Weibull distribution function, were similar to those estimated at room temperature. Regarding the second peak, however, the estimated effective stresses in the first cycle were significantly lower, by about 300 and 400 MPa in tension and compression, respectively. The estimated saturated effective stresses were about 700 MPa in both tension and compression.

Table 6. List of conducted fatigue tests on René 41 superalloy at RT and 800 °C, complemented by lifetime, stress amplitude and plastic strain amplitude data evaluated at half-life.

René 41	ε_a (%)	N_f (-)	$\sigma_{a,50\%Nf}$ (MPa)	$\varepsilon_{ap,50\%Nf}$ (-)	$\varepsilon_{ap,50\%Nf}$ (%)	SF(%)
Solutionised, fatigue at RT	0.5	13096	701.8	0.0016	0.163	8.9
	0.8	3873	761.6	0.0041	0.414	11.5
	1	2028	816.1	0.0059	0.594	11.7
	1.2	997	857.9	0.0075	0.748	11.1
Aged, fatigue at RT	0.5	10689	900.3	0.0007	0.074	10.6
	0.8	2734	1010.5	0.0032	0.315	13.4
	1	2045	1040.8	0.0050	0.496	12.2
	1.2	792	1082.3	0.0068	0.679	12.2
Aged, fatigue at 800 °C	0.23	115266	382.3	1.73E-05	0.002	
	0.35	5470	541.1	0.0003	0.029	
	0.5	2476	676.7	0.0005	0.054	
	0.8	280	850.9	0.0026	0.256	

Table 7. Fitting curves coefficients and exponents.

René 41	σ_f' (MPa)	b (-)	ε_f' (%)	c (-)	K (MPa/100)	n (-)
Solutionised, fatigue at RT	1872	-0.073	82.15	-0.603	874.1	0.127
Aged, fatigue at RT	1568	-0.079	577.8	-0.884	1109	0.081
Aged, fatigue at 800 °C	2021	-0.135	58.34	-0.835	1041	0.161

Table 8. Effective moduli and effective stresses for γ and γ' phases of René 41 superalloy cycled with ε_a = 0.8% at RT and 800 °C, derived from the half-life hysteresis half-loops and the corresponding second derivatives, respectively.

René 41	Half-loop	E_{eff} (GPa)	$\sigma_{e0,\gamma}$ (MPa)	$\sigma_{es,\gamma}$ (MPa)	$\sigma_{e0,\gamma'}$ (MPa)	$\sigma_{es,\gamma'}$ (MPa)
Solutionised, fatigue at RT	Tensile	203	121	93	-	-
	Compressive	204	89	85	-	-
Aged, fatigue at RT	Tensile	209	328	205	1080	-
	Compressive	206	297	278	1009	-
Aged, fatigue at 800 °C	Tensile	174	196	156	786	683
	Compressive	165	211	159	593	716

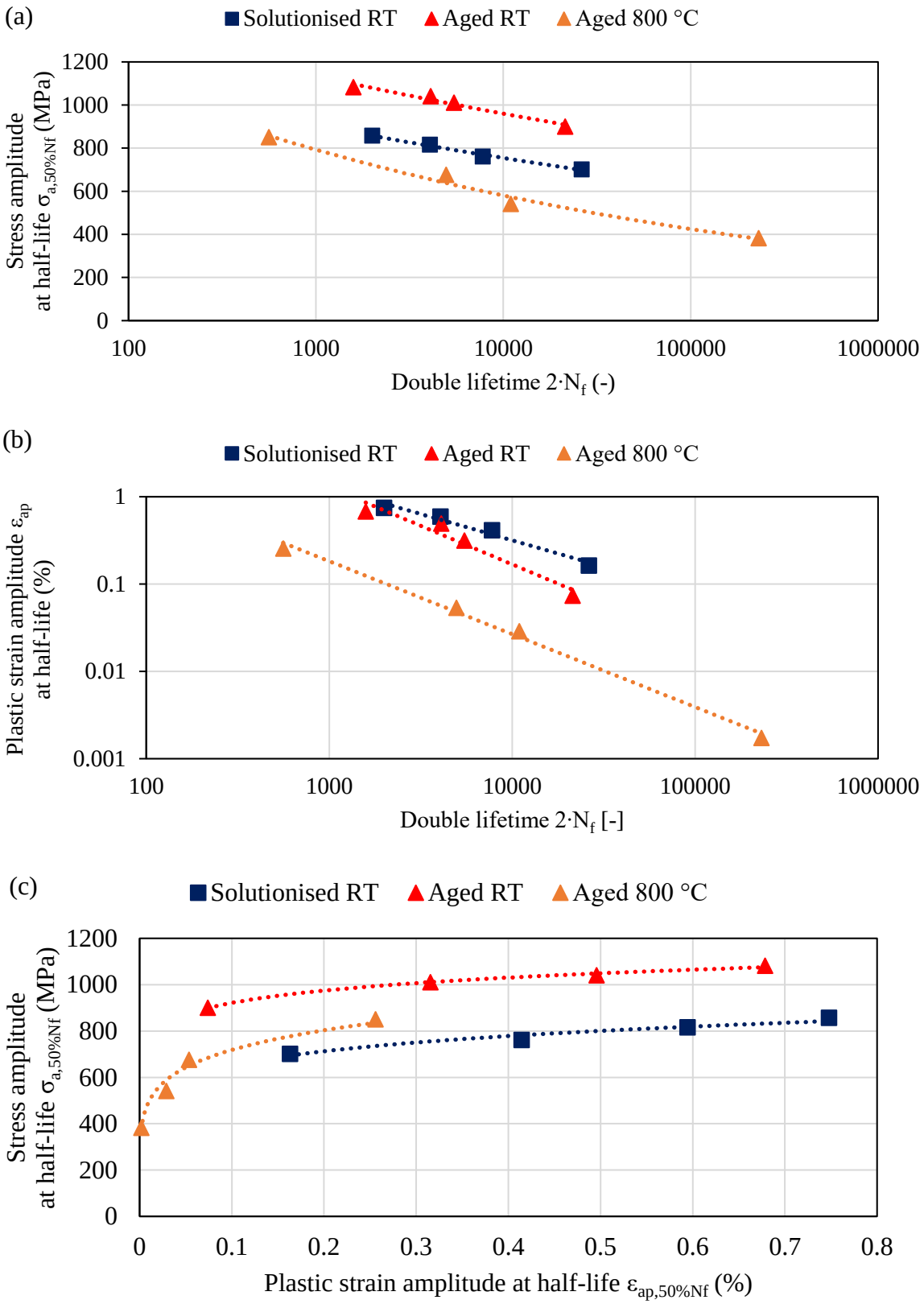

Fig. 5.5. Analyses of fatigue performance of René 41 superalloy, cycled at RT and 800 °C. (a) Basquin and (b) Coffin-Manson lifetime representation. (c) Cyclic stress-strain curve in the representation of half-life stress amplitude $\sigma_{a,50\%Nf}$ vs. half-life plastic strain amplitude $\varepsilon_{ap,50\%Nf}$.

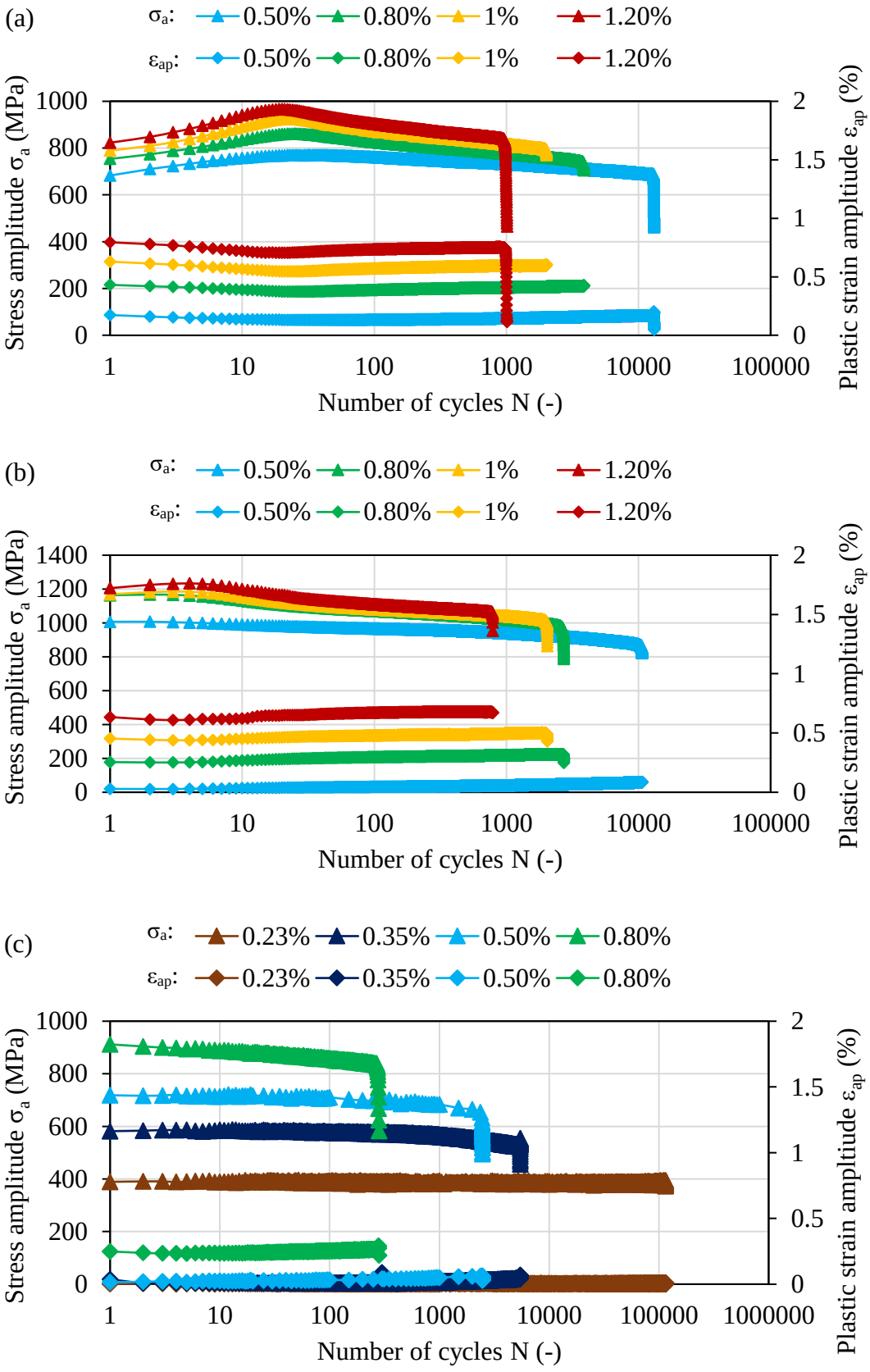

Fig. 5.6. Cyclic hardening/softening curves of René 41 superalloy cycled at RT and 800 °C. (a) Solutionised René 41 at RT. (b) Aged René 41 at RT. (c) Aged René 41 at 800 °C.

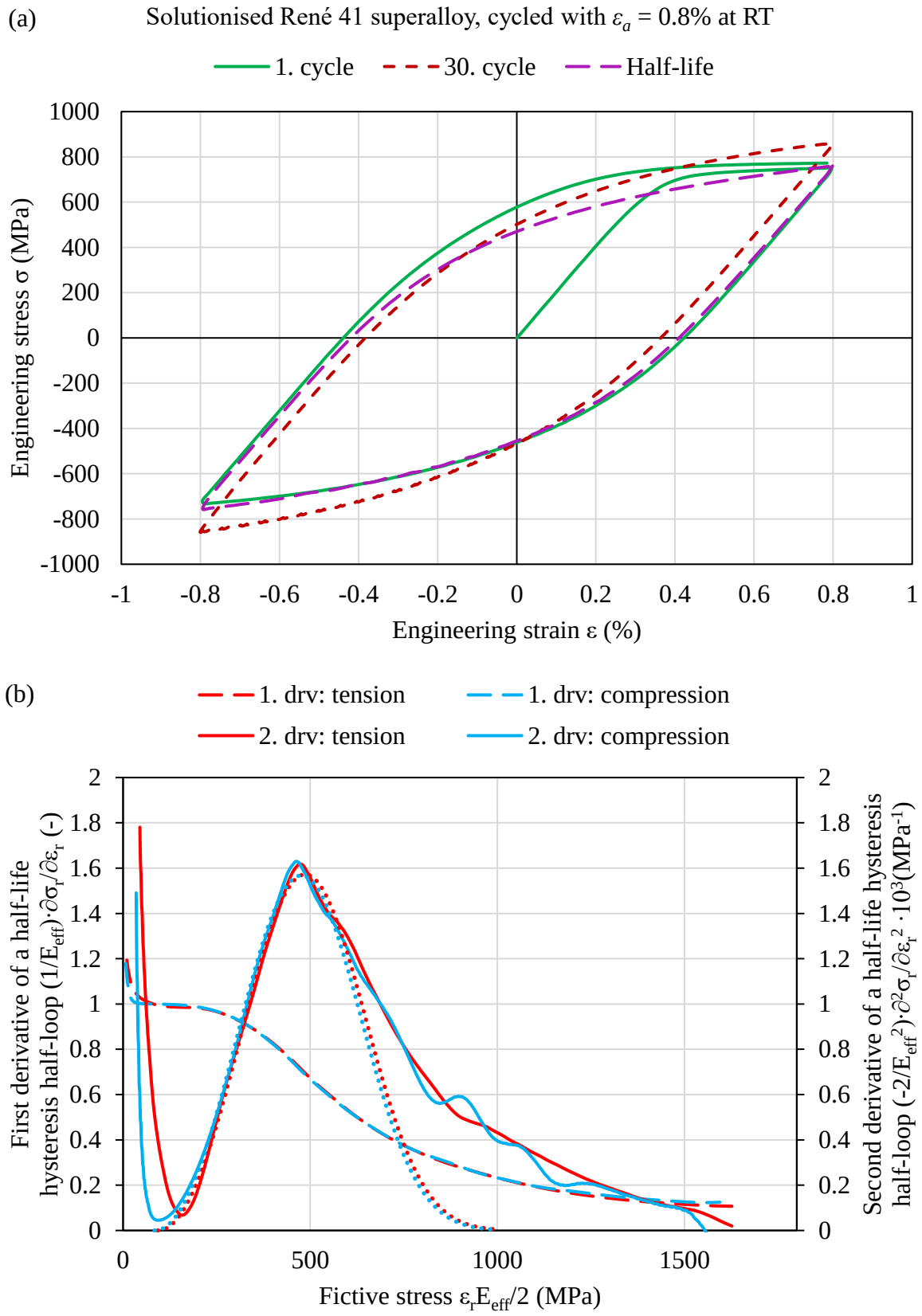

Fig. 5.7. Analysis of cyclic plasticity of solutionised René 41 superalloy cycled with ε_a = 0.8% at RT, using the statistical theory of the hysteresis loop. (a) First cycle and half-life hysteresis loops. (b) The first and second derivatives for both tensile and compressive half-loops recorded at half-life. The second derivatives show a characteristic peak corresponding to the one-phase material.

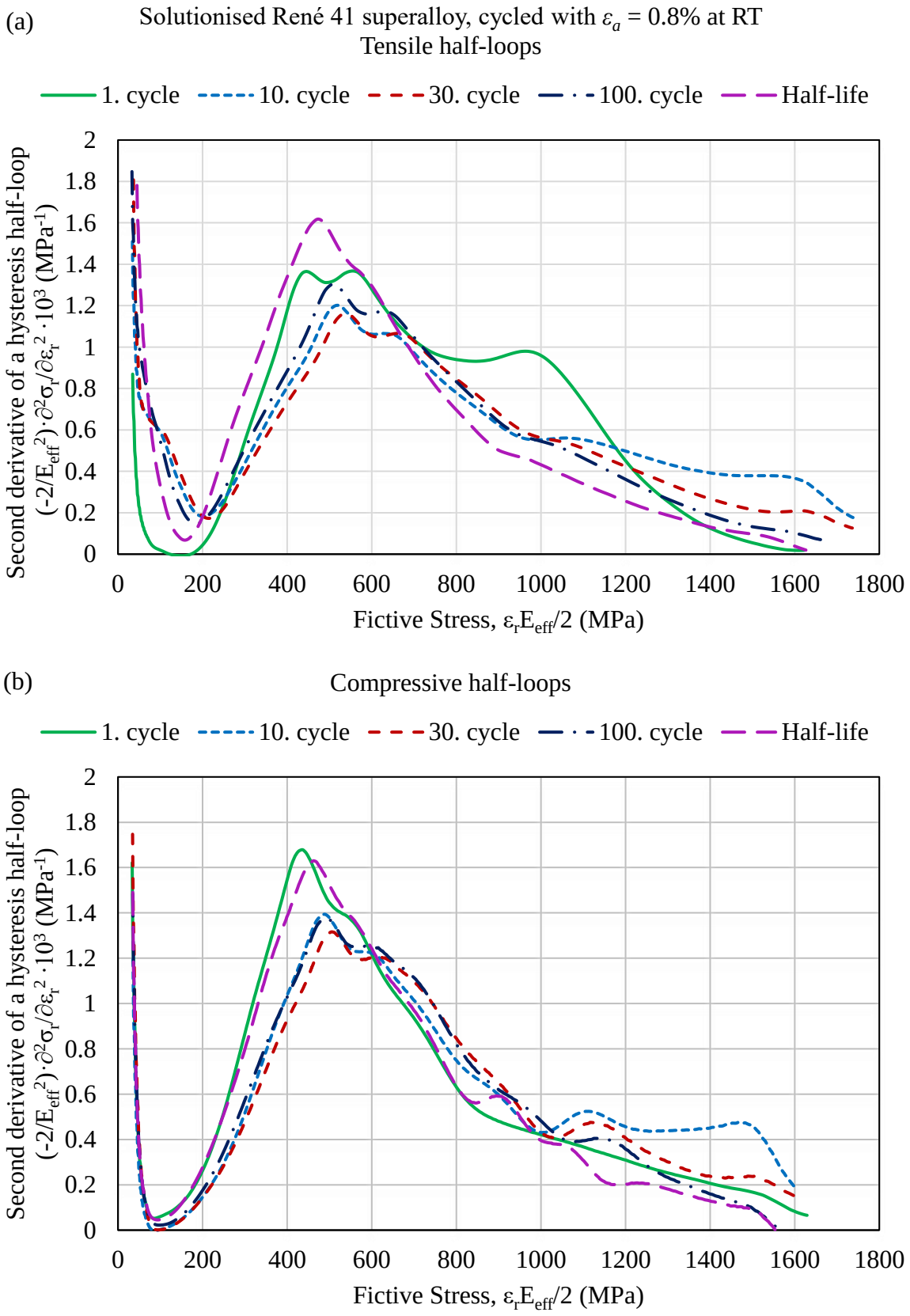

Fig. 5.8. Evolution of the second derivatives of the hysteresis loops for solutionised René 41 superalloy, cycled with ε_a = 0.8% at RT, over fatigue life, derived from (a) tensile and (b) compressive half-loops. Note that the "1. cycle" refers to the first complete tensile or compressive half-loop.

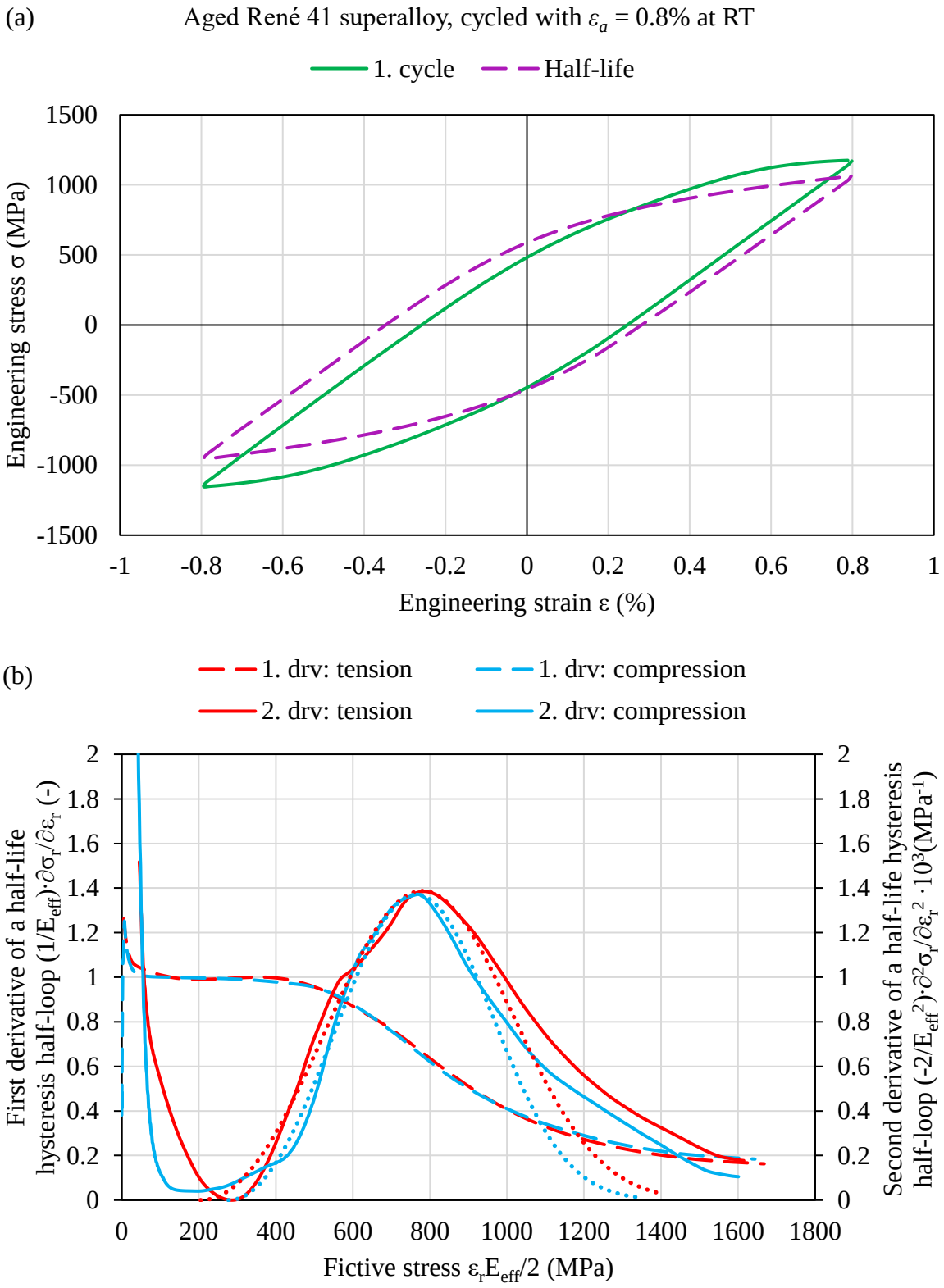

Fig. 5.9. Analysis of cyclic plasticity of aged René 41 superalloy cycled with ε_a = 0.8% at RT, using the statistical theory of the hysteresis loop. (a) First cycle and half-life hysteresis loops. (b) The first and second derivatives for both tensile and compressive half-loops recorded at half-life.

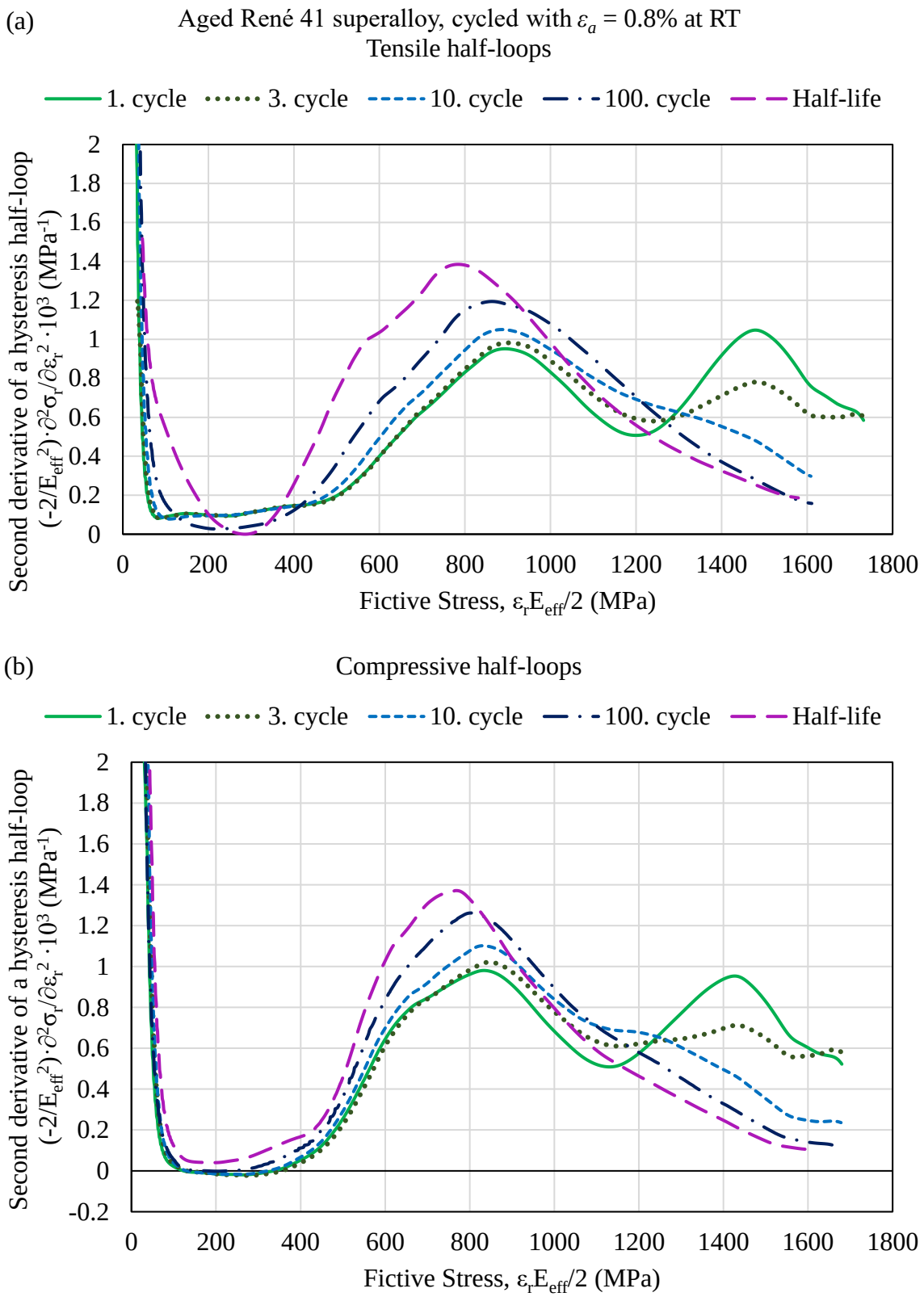

Fig. 5.10. Evolution of the second derivatives of the hysteresis loops for aged René 41 superalloy, cycled with ε_a = 0.8% at RT, over fatigue life, derived from (a) tensile and (b) compressive half-loops. Note that the "1. cycle" refers to the first complete tensile or compressive half-loop.

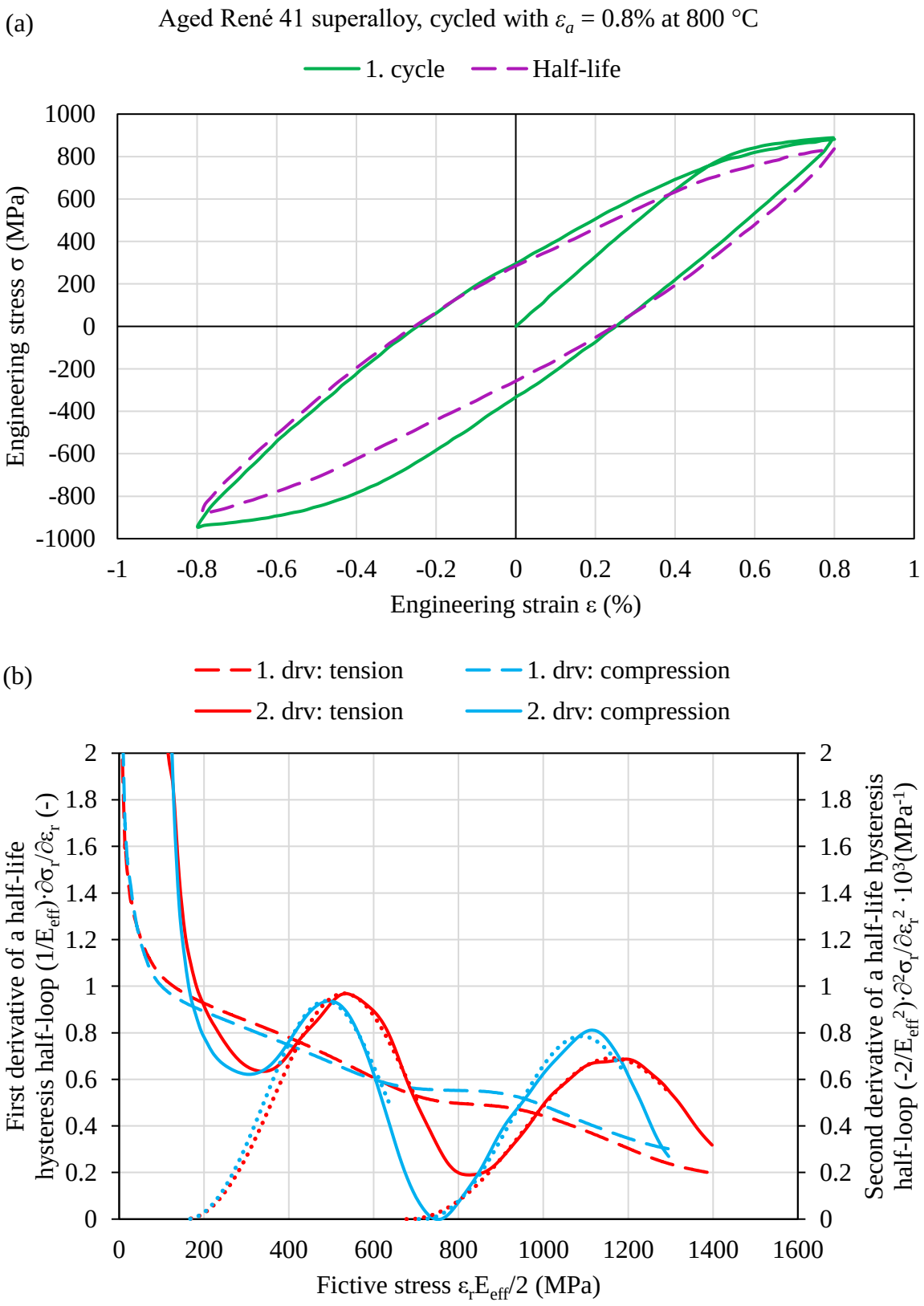

Fig. 5.11. Analysis of cyclic plasticity of aged René 41 superalloy cycled with ε_a = 0.8% at 800 °C, using the statistical theory of the hysteresis loop. (a) First cycle and half-life hysteresis loops. (b) The first and second derivatives for both tensile and compressive half-loops recorded at half-life. The second derivatives show characteristic peaks corresponding to the two dominant phases, γ and γ'.

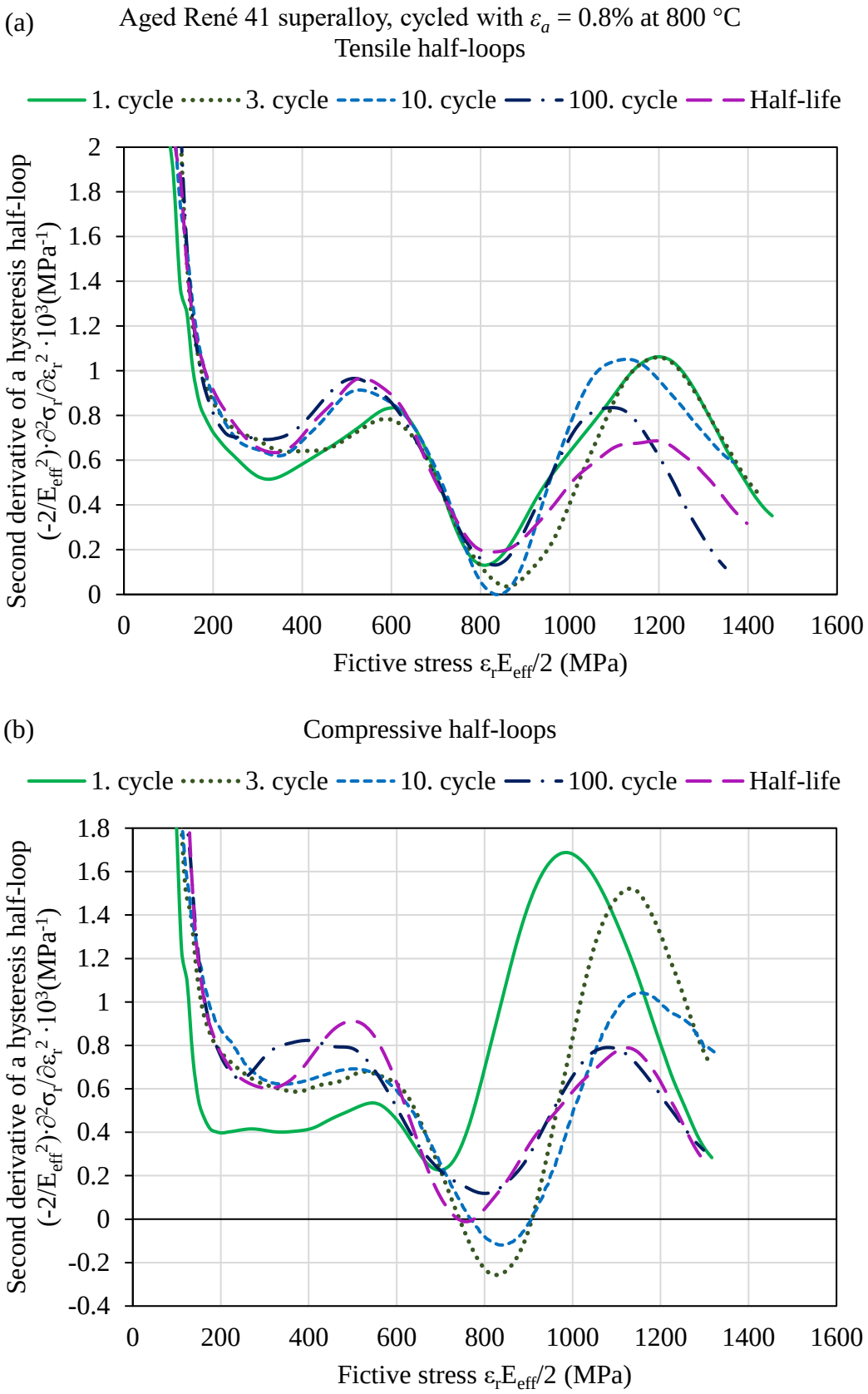

Fig. 5.12. Evolution of the second derivatives of the hysteresis loops for aged René 41 superalloy, cycled with ε_a = 0.8% at 800 °C, over fatigue life, derived from (a) tensile and (b) compressive half-loops. Note that the "1. cycle" refers to the first complete tensile or compressive half-loop.

5.3 Damage observation

5.3.1 Solutionised René 41 superalloy at RT

Overall damage, as well as deformation mechanisms, were analysed using SEM, SEM+FIB and TEM. A typical fracture surface is shown in Fig. 5.13a–d. All tested specimens exhibited multiple crack initiation (see Fig. 5.13a) with a principal crack governing lifetime. The damage was predominantly transgranular with striations on the fracture surface, indicating crack growth under cyclic loading (see Fig. 5.13b). There were numerous dimples on the fracture surface as shown in Fig. 5.13c, with a secondary phase particle at the bottom of a dimple as shown in Fig. 5.13d, indicating decohesion along particle/matrix interface due to the applied stress. Considering the size and morphology of the particle, these were presumably MC carbides, Ti(C,N) carbonitrides, and possibly also M_3B_2 borides.

Fig. 5.14a shows a typical specimen surface, heavily roughened by PSBs emanating as PSMs, and with numerous secondary cracks along the PSMs as shown in Fig. 5.14b. The density of PSMs, as well as secondary cracks along them, appeared to be proportional to total strain amplitude. Fatigue crack initiation sites were analysed using SEM with EBSD to unambiguously distinguish grain boundaries from twin boundaries. At room temperature, the cracks predominantly (over 90%) initiate at PSMs as shown in the chart in Fig. 5.22. FIB sectioning (Fig. 5.14c–e) and STEM analysis of the foils (Fig. 5.14f–g) revealed that cracks may initiate at both sides of the PSM (with an acute and/or obtuse angle to the specimen surface) and in the middle of the PSM as well. Stage I microcracks follow active slip planes, more specifically the PSBs, at which they are initiated. The microcrack propagation direction can be diverted soon after the initiation, as shown in detail in Fig. 5.14g, where a deflection by a secondary phase particle is depicted. The divergence can be caused also simply by changing to a plane parallel with a slip band. Dislocation density ahead of the early crack tip shows little ordering (Fig. 5.14f). Few microcracks were observed close to, and occasionally also directly at the twin boundaries, where slip bands are formed too.

Fig. 5.15 shows a post-mortem dislocation structure of a representative specimen cycled with ε_a = 0.5%. Fig. 5.15a shows intensive slip in PSBs on active {111} planes, which consist of parallel arrays of dislocations, as shown in detail in Fig. 5.15b. Even though multiple slip occurred, one slip system was always dominant. This is apparent also from Fig. 5.14f, where all the observed PSMs grew in the direction of the Burgers vector of the dominant slip system. PSBs were often observed in groups of closely-spaced clusters of several PSBs, while the spacing between two neighbouring clusters was larger. Fig. 5.15c shows intensive slip in PSBs grouped in clusters separated by a thick slab of the matrix. Furthermore, the image brings evidence of slip band formation at the twin boundaries. Dislocations were often dissociated into [112] {111} Shockley partials, forming stacking faults, as evidenced in the near-twin boundary area in Fig. 5.15d. No deformation twins were observed.

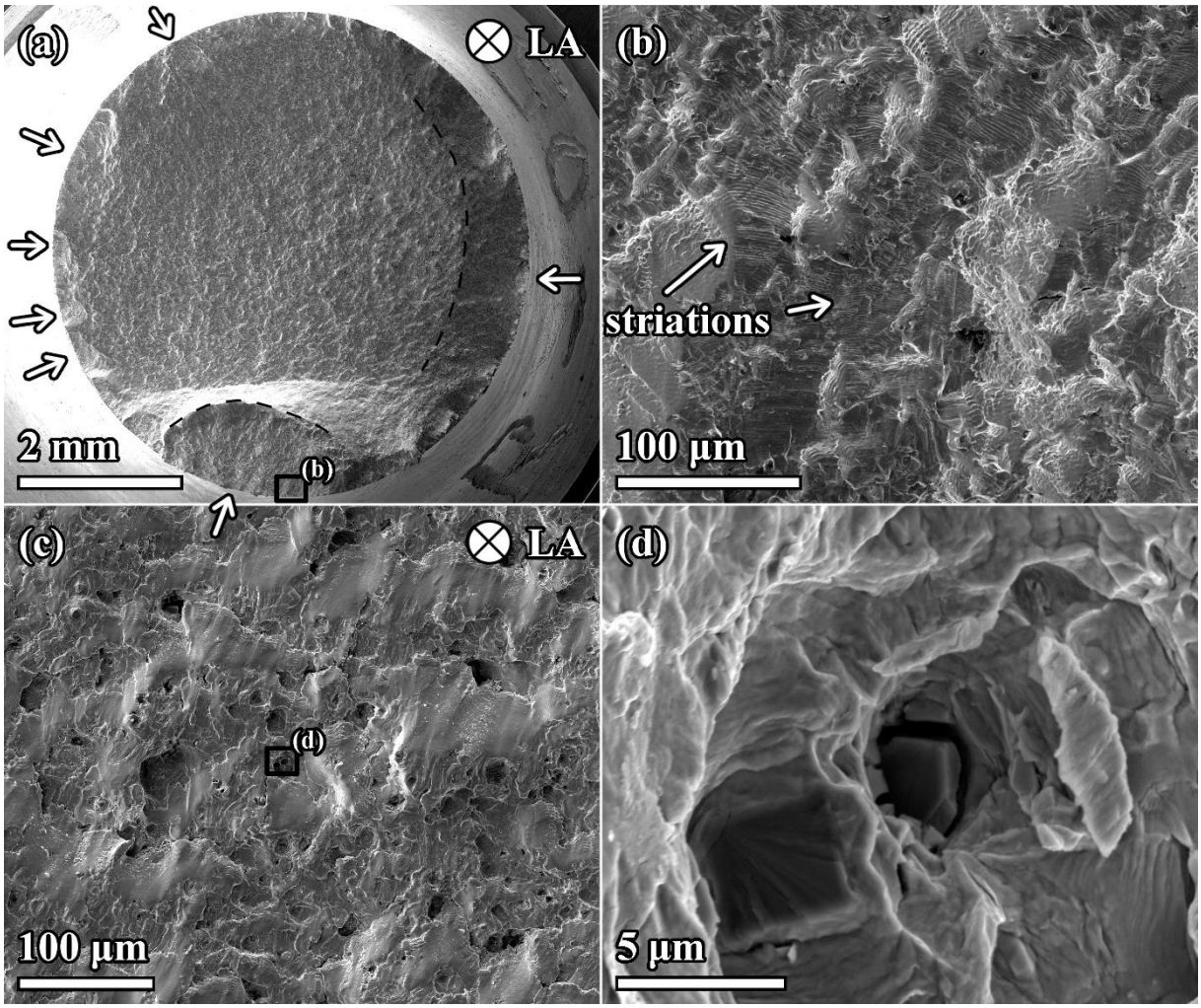

Fig. 5.13. SEM micrographs showing fatigue damage imposed on solutionised René 41 superalloy cycled with ε_a = 0.5% at RT, observed *post-mortem*. (a) Overview of fracture surface with multiple fatigue crack initiation (pointed out by arrows) and highlighted areas of fatigue crack growth, (b) a detail showing a crack initiation site with striations corresponding to early crack propagation. (c) Transgranular fracture with holes corresponding to cracking along brittle carbide phases, shown in (d) in detail. Note that flat-like facets are pressure marks, formed on the bare fracture surface due to high loads imposed on the reduced effective cross-section.

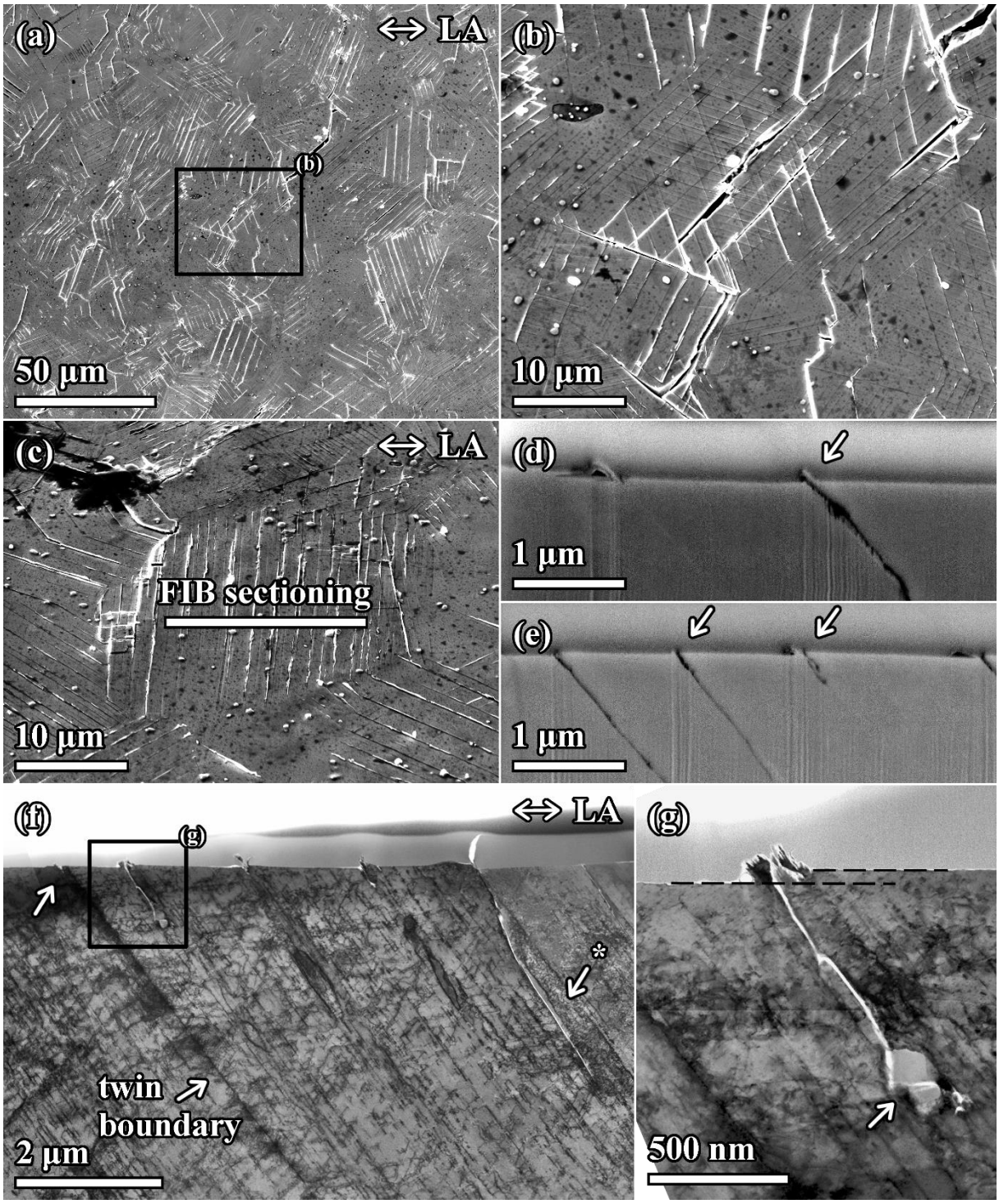

Fig. 5.14. Analysis of crack initiation in solutionised René 41 superalloy cycled with ε_a = 0.5% at RT, observed *post-mortem*. SEM micrographs showing (a) surface relief with extensive PSM formation and (b) secondary cracks along the PSMs. (c) A grain with numerous cracks along the PSMs, chosen for FIB sectioning. (d–e) Details of the cross-section with (d) a crack initiating at the side of a PSM where the slip plane is inclined to the specimen surface at an obtuse angle and (e) cracks initiating at a PSM at an acute angle to the specimen surface. (f–g) STEM micrographs showing (f) dense spacing of PSBs and the resulting PSMs at the surface, observed on a surface lamella. Notice the PSB at the twin boundary and the resulting PSM at the surface close to it. * marks a high dislocation content ahead of the crack tip with no further ordering. (g) A detail showing a microcrack initiated amid a PSM and deflected by a carbide (or boride) particle. There is a surface step at the PSM.

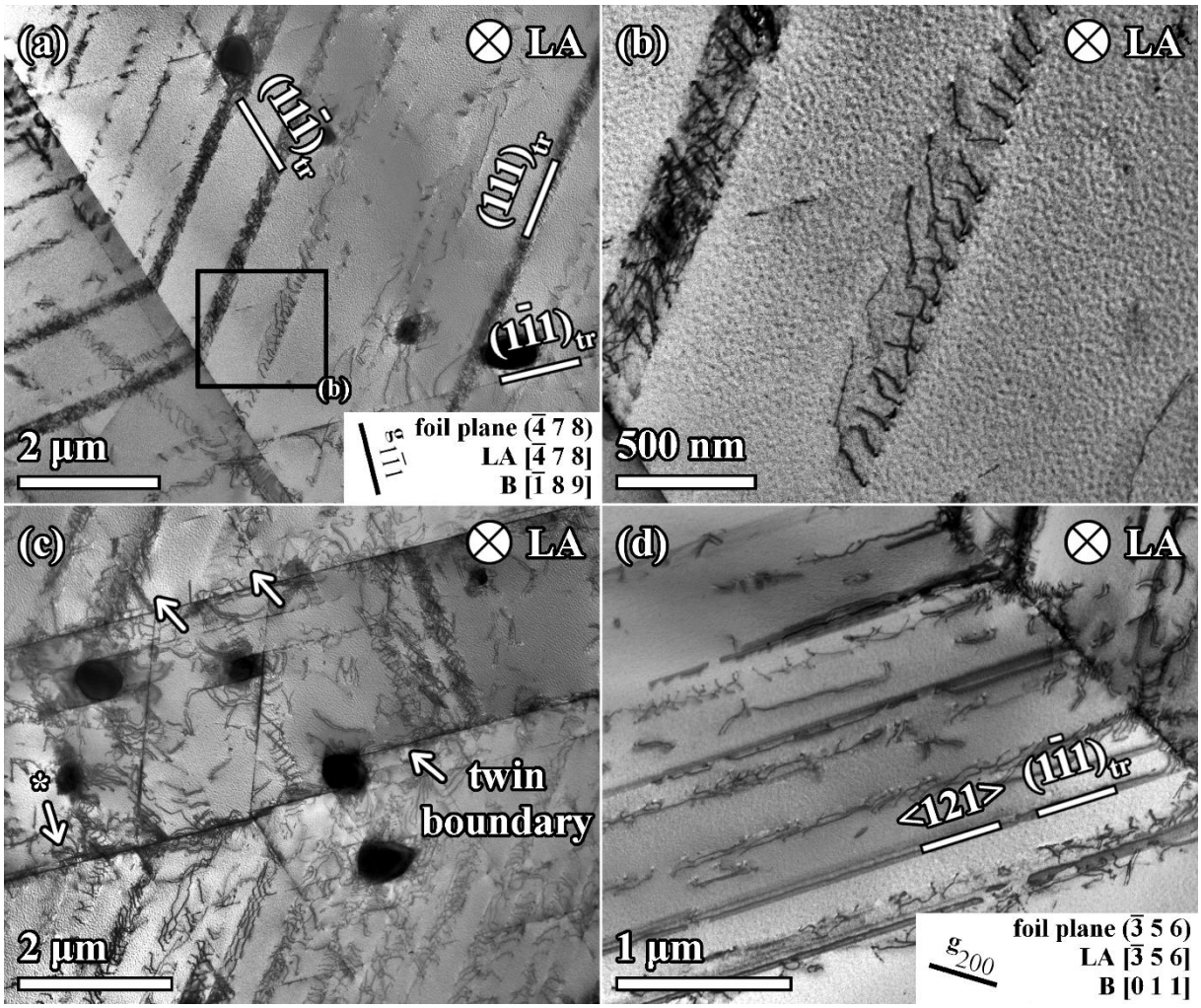

Fig. 5.15. STEM micrographs revealing deformation mechanisms in solutionised René 41 superalloy cycled with ε_a = 0.5% at RT, observed *post-mortem*. (a) The concentration of slip in PSBs. Dislocation content in the matrix is negligible. (b) A detail showing the internal structure of PSBs, comprising parallel arrays of dislocations. (c) Intensive slip bands crossing twin boundaries. Notice the slip bands in the close vicinity of twin boundaries marked by *. Arrows point out two clusters of PSBs separated by a thick slab of the matrix. (d) Stacking faults due to dissociation of perfect dislocations into [121] $(1\bar{1}1)$ Shockley partials, observed in the zone axis [110].

5.3.2 Aged René 41 superalloy at RT

Fig. 5.16a shows a typical fracture surface of an aged specimen subjected to fatigue loading at room temperature, exhibiting dimples (Fig. 5.16d) corresponding to a dominant transgranular fracture mode. Intergranular crack propagation was scarce. There were also small holes on the fracture surface, with secondary phase particles observed at the bottom (Fig. 5.16c), indicating a crack propagation along them, similar to the solutionised state. The fatigue cracks initiated on the surface (see e.g. Fig. 5.16b), predominantly from PSMs, which were abundant on the specimen surface as shown in Fig. 5.17a–c. In comparison to the solutionised state, crack initiation from twin boundaries was a little more frequent (almost 9%, as shown in the chart in Fig. 5.22). Such a crack initiated and growing along a twin boundary is shown in Fig. 5.17d. Initiation from secondary phase particles was scarce, however, their role was found to be important in crack propagation, since they were found to deflect the early microcracks as revealed by the FIB-SEM tomography analysis shown in Fig. 5.17e–i. Microcracks were

found to create networks along the active slip planes and to connect multiple PSMs (see the coalescence of two microcracks in Fig. 5.17h–i).

The material was mostly deformed by intensive PSBs along {111} planes, as shown in Fig. 5.18a. Multiple slip with usually one dominant system occurred in the majority of grains. The PSBs were composed of parallel arrays of dislocations (see Fig. 5.18b) confined to the matrix, as *γ'* precipitate shearing was observed only scarcely (Fig. 5.18d) and the majority of precipitates remained intact. Fig. 5.18c shows high dislocation density in PSBs at both sides of a twin along its boundaries.

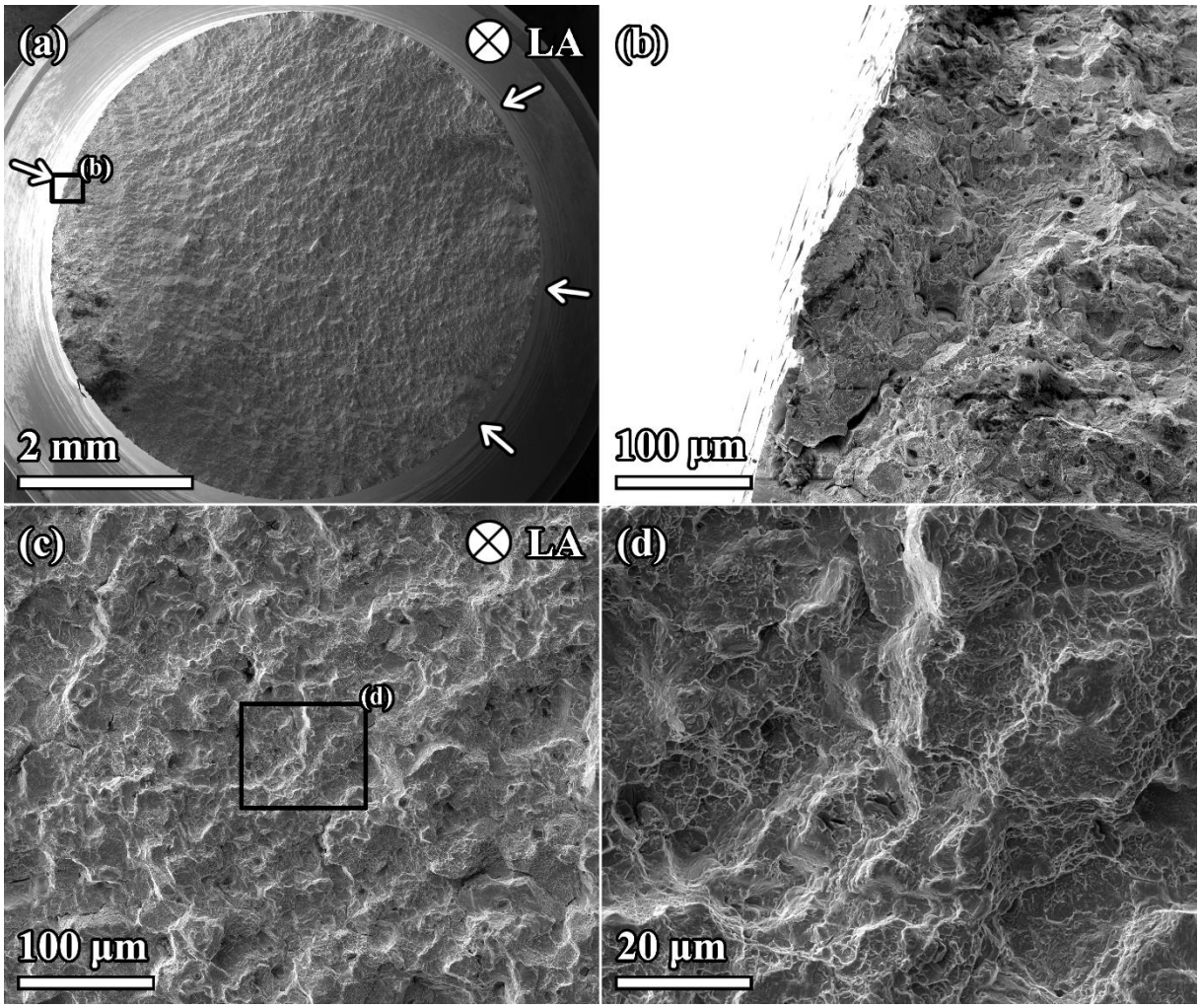

Fig. 5.16. SEM micrographs showing fatigue damage imposed on aged René 41 superalloy cycled with ε_a = 0.8% at RT, observed *post-mortem*. (a) Overview of fracture surface with multiple fatigue crack initiation (pointed out by arrows), (b) a detail showing the initiation site of the principal crack, growing from the surface. (c) Numerous holes in the fracture surface correspond to cracking along secondary phases, (d) transgranular dimple character of fracture surface in detail.

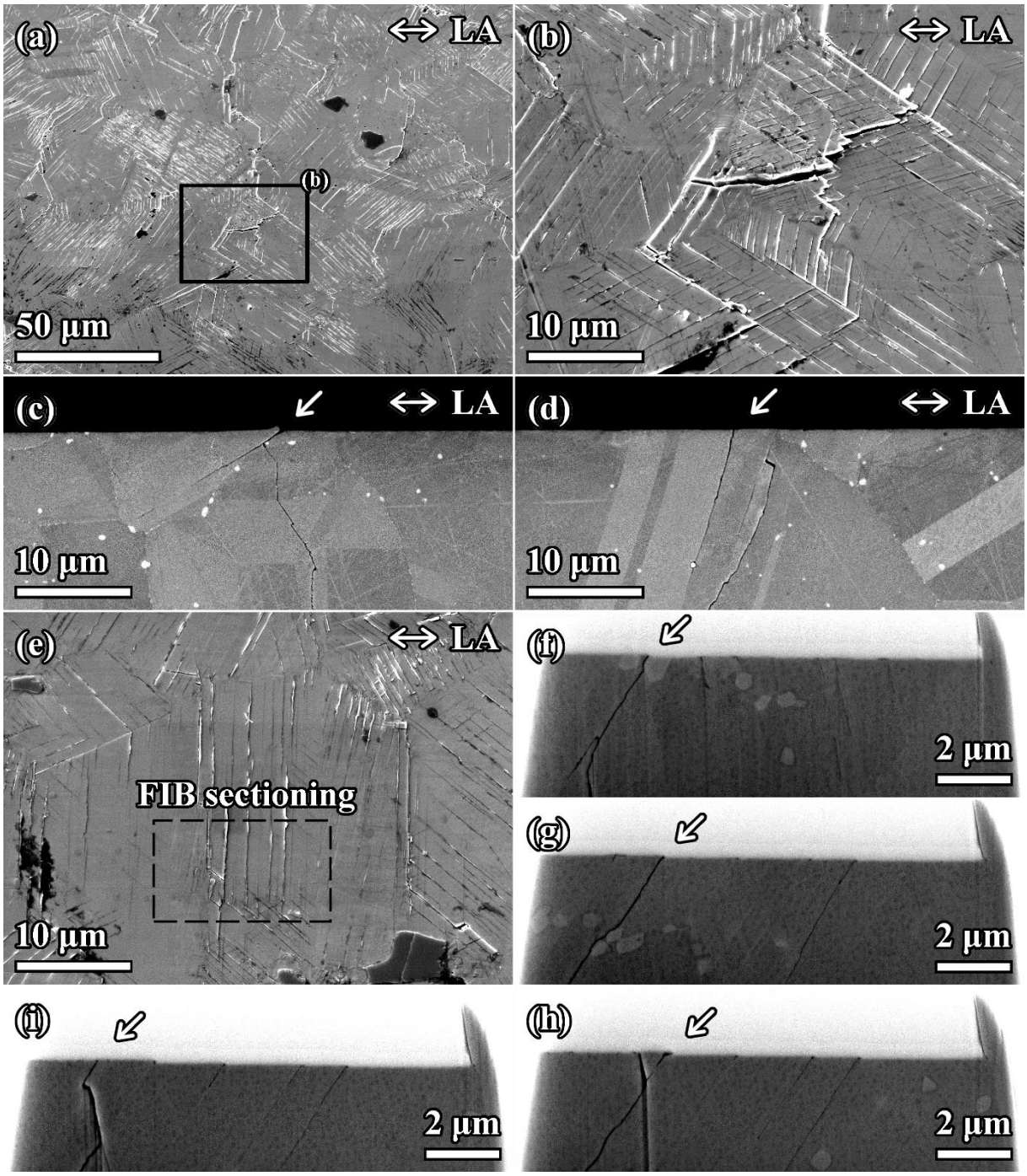

Fig. 5.17. SEM analysis of crack initiation in aged René 41 superalloy cycled with ε_a = 0.5% at RT, observed *post-mortem*. (a) Surface relief with extensive PSM formation and (b) a detail showing numerous secondary cracks along the PSMs. (c–d) Longitudinal cross-sections showing crack initiation at (c) a PSM and at (d) a twin boundary. (e–i) FIB-SEM tomography analysis: (c) SEM micrograph of a conveniently oriented grain chosen for FIB sectioning. (f–i) Details of the FIB cross-section with (f) a crack initiating at a surface secondary phase particle and further propagating along a slip plane, (g) the same crack initiating at a PSM and being deflected by secondary phase particles just before propagation across a grain boundary, (h) crack coalescence and (i) initiation of another crack from another parallel PSM.

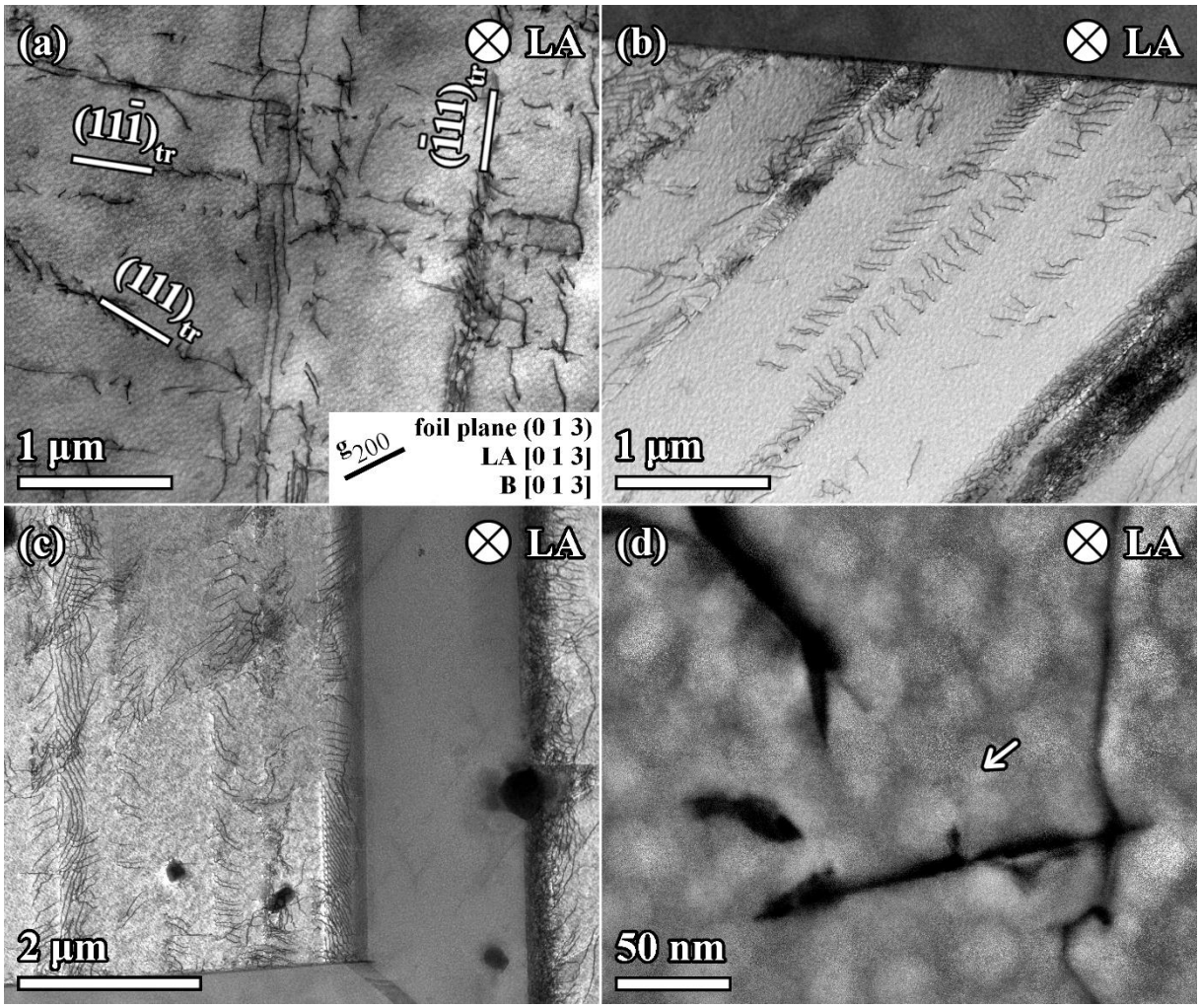

Fig. 5.18. STEM micrographs of aged René 41 superalloy cycled with ε_a = 0.5% at RT, observed *post-mortem*. (a) Typical dislocation structure with multiple active slip systems along different slip planes. (b) Numerous PSBs, internally consisting of parallel arrays of dislocations, arranged in pile-ups at a twin boundary. (c) PSBs formed at twin boundaries. (d) A detail revealing γ' precipitate shearing, pointed out by the arrow.

5.3.3 Aged René 41 superalloy at 800 °C

Fig. 5.19 reveals the character of the damage as well as the predominant damage mechanisms in aged René 41 superalloy cycled at 800 °C. The damage was predominantly intergranular which can be seen on the fracture surface shown in Fig. 5.19a–b. Specimen surface observation revealed an oxide layer covering the surface. The oxide layer formed at the weak points of the microstructure, namely grain boundaries, twin boundaries and slip markings, had a bulgy appearance as shown in Fig. 5.19c, and in greater detail in Fig. 5.20. A SEM scrutiny of a specimen cross-section (cycled with ε_a = 0.5%), shown in Fig. 5.20a–b, uncovered the extent of surface and subsurface damage, mostly in the form of voids and microcracks along the grain boundaries, with the depth of approximately 15 μm. STEM+EDS analysis of a lamella prepared from a specimen surface, shown in Fig. 5.19e, revealed the chemical composition and internal structure of the oxidic layer as well as the surface layer of the underlying substrate, which shows slight depletion of Cr. It appears the oxidic layer composes of three sublayers: firstly, lying on top of the substrate there is a Cr oxide layer with partitions of Ti and Al to it, this layer is approximately 500 nm thick, secondly, there is a thin (~100 nm) layer of Co-Fe oxides and finally, a thicker (~300 nm) Ni-Co oxide layer lies at the top.

Cross-sections produced by FIB, shown in Fig. 5.20c–f, pointed out the importance of grain boundaries in oxidation. Fig. 5.20d–e clearly show an oxide layer formed along the grain boundary and a microcrack originating where the grain boundary intersects the specimen surface. A detailed study on the specimen cycled with ε_a = 0.5% showed that even though grain boundary initiation was dominant, other sites contributed to the fatigue crack initiation as well, namely twin boundaries and PSMs (see Fig. 5.22). A detail of a FIB cross-section in Fig. 5.20f shows the penetration of oxides at the PSM and an oxidic intrusion along an active slip plane. Although the oxidation of the twin boundaries appears to be less bulgy (see Fig. 5.20d) than at PSMs, the crack initiation analysis (Fig. 5.22) showed that crack initiation occurred more often at twin boundaries. Mostly, the oxidised PSMs were observed in relatively large grains (~100 μm such as the one shown in Fig. 5.19c). Note that the contribution of secondary phases in crack initiation could be captured only in the case of intragranular crack initiation, as the grain boundary carbides were abundant (see Fig. 5.21e).

Most grains exhibited low dislocation density with only a few or completely absent slip bands. Plastic deformation was more or less equally divided between the matrix and the γ' precipitates. Dislocations were observed in the matrix, usually bowing between sheared γ' precipitates, which was manifested in the frequent occurrence of stacking faults (see the dark circles e.g. in Fig. 5.21a). In some grains, no dislocation arrangements were observed (Fig. 5.21a), while in some, traces of intensive deformation by slip bands were apparent (Fig. 5.21b) on octahedral planes. Internally, two types of PSBs were observed: Fig. 5.21c shows a typical PSB with parallel arrays of dislocations running along an active slip plane, which appeared rather scarcely, while Fig. 5.21d shows far more frequent image of a rather dislocation-depleted PSB, in which no parallel arrays were present and sometimes only the sheared γ' precipitates could be observed. As a by-product of the high-temperature exposure, grain boundary carbides coarsened (Fig. 5.21), which is mostly related to the Mo-rich M_6C carbides, as the grain boundary Cr-rich $M_{23}C_6$ carbides showed no apparent change in size.

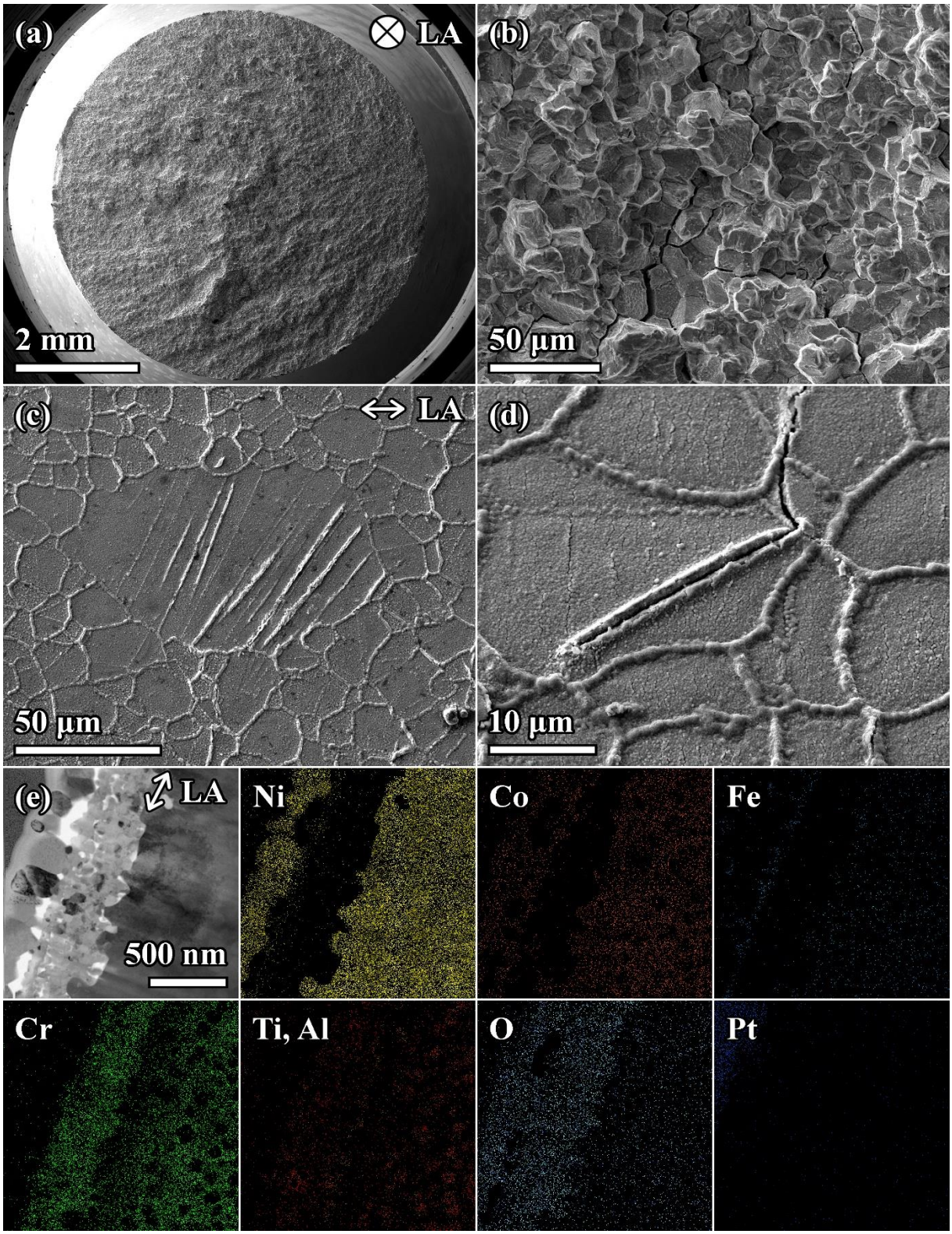

Fig. 5.19. Analysis of overall damage imposed on aged René 41 superalloy cycled with ε_a = 0.5% at 800 °C, observed *post-mortem*. (a–d) SEM micrographs of (a) a fracture surface and (b) a detail showing intergranular fracture with numerous facets corresponding to crack propagation along the grain boundaries, (c) oxidised specimen surface with preferential oxidation at grain boundaries, twin boundaries, and slip markings, and (d) a detail showing a transgranular crack propagation. (e) STEM+EDS analysis reveals the composition of the oxidic layer on top of a grain. Notice the slight depletion of Cr in the innermost sublayer of the substrate, on top of which there are thick Cr-enriched and thin Co and Fe-enriched sublayers, and the outermost Ni and Co-enriched oxide sublayers.

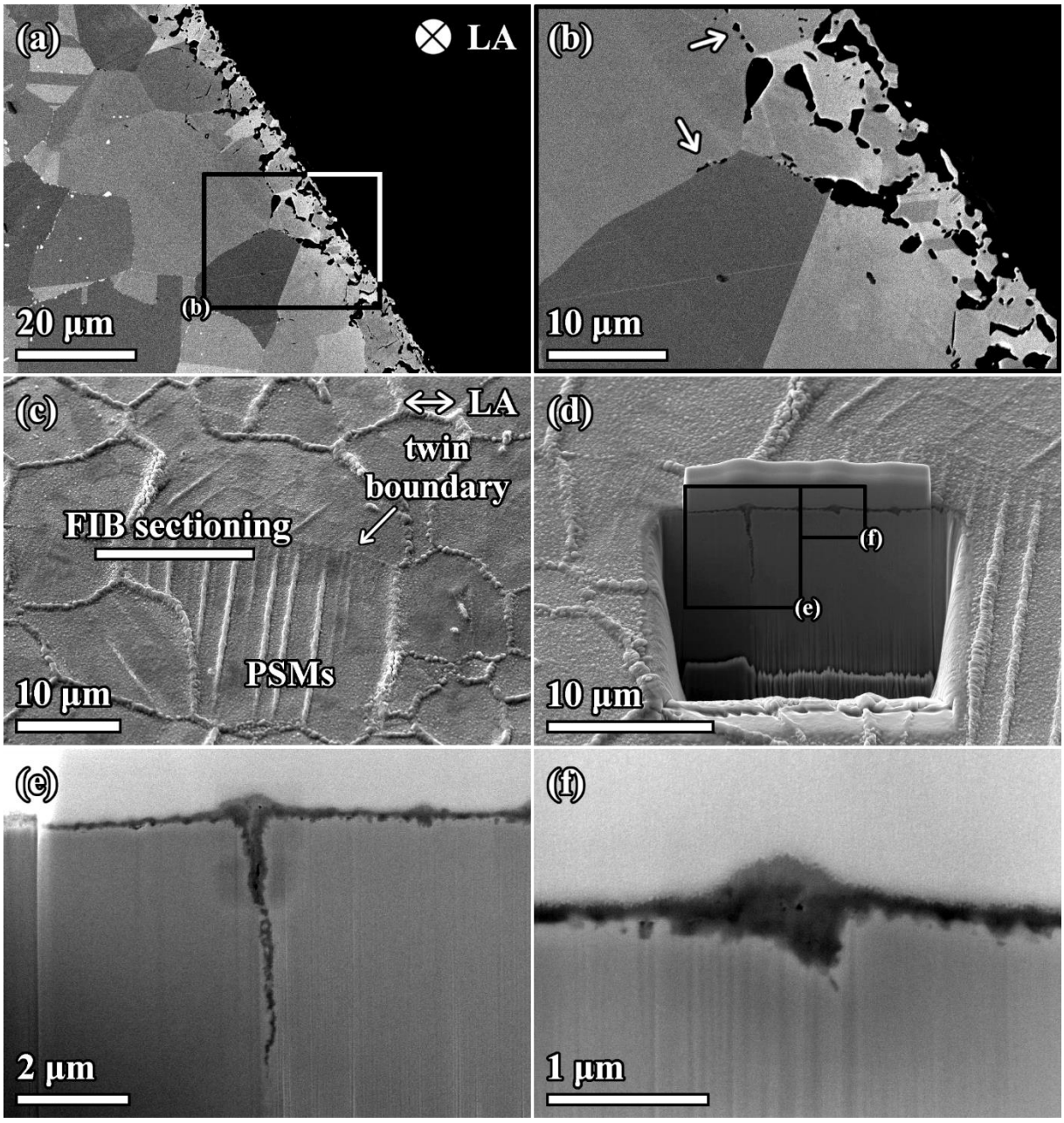

Fig. 5.20. SEM micrographs of aged René 41 cycled with ε_a = 0.5% at 800 °C, observed *post-mortem*. (a–b) Cross-section showing the extent of subsurface damage. (b) Microvoids at grain boundaries in detail. (c) Overview image of preferential oxidation sites at grain boundaries and, in case of above-average sized grains, twin boundaries and slip markings. Details of (d) FIB cross-section reveal (e) crack propagation due to oxides formed at the grain boundary and (f) a profile of an oxidised slip marking with oxidic intrusion, or initiated stage I microcrack along the active slip plane.

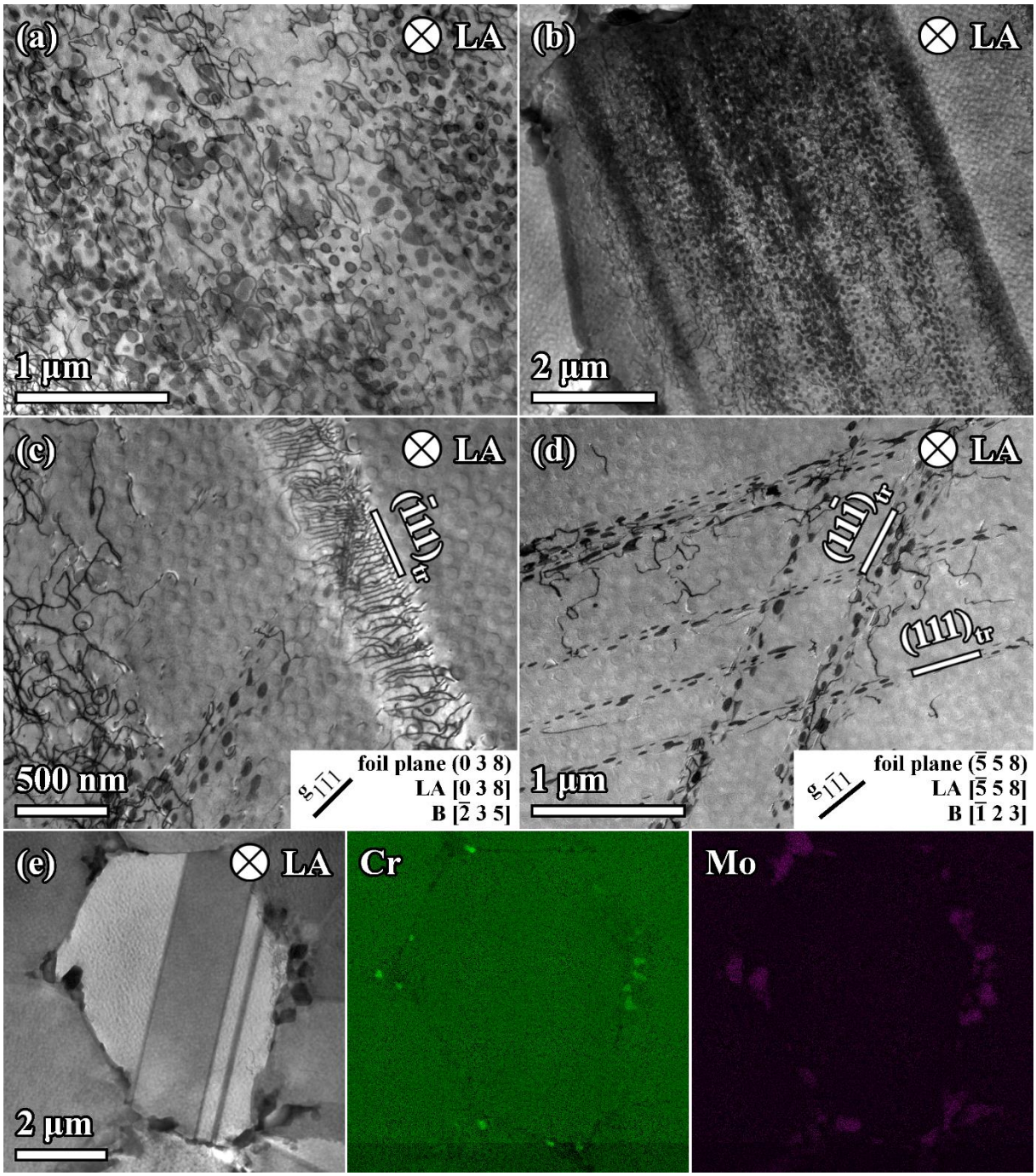

Fig. 5.21. STEM micrographs of aged René 41 cycled with ε_a = 0.5% at 800 °C, observed *post-mortem*. (a) A grain deformed rather homogenously, no traces of slip bands were observed. (b) Massively deformed grain by intensive slip bands. (c) A detail showing a slip band with parallel arrays of dislocations. Notice the Orowan loops at the bottom right corner. (d) A slip band with numerous stacking faults. (e) STEM+EDS analysis shows coarsening of the secondary phases, predominantly the Mo-rich M_6C grain boundary carbides.

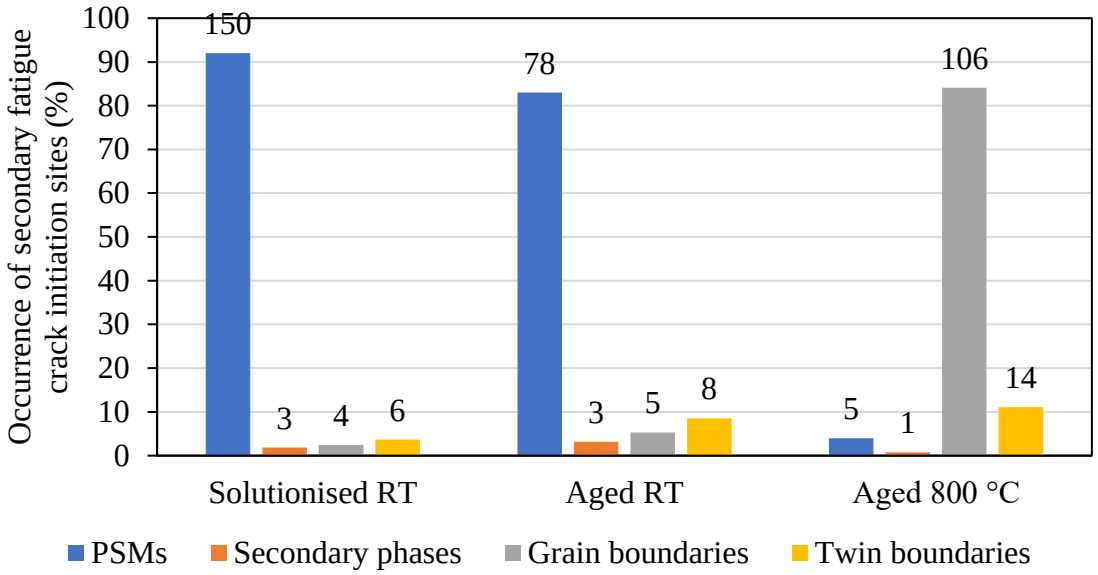

Fig. 5.22. Chart depicting a shift of initiation sites of secondary fatigue cracks in René 41 superalloy cycled with ε_a = 0.5% from predominant PSMs at room temperature (RT) to other initiation sites at 800 °C, particularly to the grain boundaries. The number of corresponding sites is labelled above the respective bars. Note that the initiation sites were evaluated over a distance of 2 mm from the fracture surface.

5.4 Evolution of surface relief and the underlying microstructure

The evolution of features occurring on the surface due to cyclic slip was thoroughly studied. A detailed study was performed on specimens cycled with ε_a = 0.8% at room temperature. The specimen testing was interrupted after a definite number of elapsed cycles and the resulting cyclic slip irreversibilities and modifications to the dislocation structure were studied using SEM + FIB and TEM. The interruptions were performed following the procedure described in Chapter 4.2.4 and schematically illustrated in Fig. 4.3.

5.4.1 Solutionised René 41 superalloy

Fig. 5.23a shows slip markings observed on the surface after one symmetrical cycle using SEM. STEM inspection (Fig. 5.23b) of a lamella, cutting the slip markings as shown in Fig. 5.23a, revealed planar dislocation arrays on {111} planes, parallel to the trace of primary slip plane – slip bands. The arrangement in slip bands was in several cases linked with the formation of slip steps on the surface. The same features – slip steps on the surface and slip bands underneath – were observed also after 3 cycles. However, not always did the formation of slip bands results in the formation of slip steps.

More complex slip markings consisting of a shallow elevation (extrusion) and a deepening parallel (intrusion) to it were identified (see Fig. 5.24a) after 10 cycles. Fig. 5.24b shows a slip step in which the presence of an embryonic intrusion is possible, however, was not unambiguously recognized. The slip markings emerged on the surface because of the repeated strain localisation in the slip bands. Due to the persistent nature of the bands, in which cyclic slip had already been concentrated for a considerable number of cycles, the slip bands were identified as persistent slip bands (PSBs) and the corresponding slip markings atop the PSBs as persistent slip markings (PSMs). It is important to emphasize that a single PSB scarcely resulted in a single PSM in the studied material. On the contrary, several PSBs were found to participate in the formation and consequent evolution of a single PSM.

An increase in plastic strain amplitude after the 30th cycle, when the stress amplitude reached a maximum, was accompanied by the evolution of the surface relief as new PSMs emerged atop the PSBs and the existing ones developed further. That was manifested in a gradual decrease in spacing between neighbouring PSMs. Fig. 5.25a shows a well-established dislocation structure after 30 cycles. Most of the cyclic slip had already been localised into PSBs which resulted in a gradual drop in plastic strain amplitude. The PSBs were often grouped into more complex planar arrays (macro-PSBs) consisting of several individual bands as indicated in Fig. 5.26e. The identification of individual PSBs was at this point already impossible. The thickness of the individual PSBs could be estimated for solitary slip bands and was found to span over only a few slip planes (hence, well below 1 nm), as indicated in Fig. 5.26d. A more developed PSB with a larger thickness (~5 nm) can be seen at the bottom right corner of Fig. 5.26d. However, caution should be taken as the thickness was only estimated from the contrast changes associated with the corresponding PSB. PSBs and macro-PSBs emerged on the surface as PSMs and macro-PSMs, respectively. Macro-PSMs were complex in shape, formed by a cluster of extrusions and intrusions and thus reflecting the strain history of several parallel PSBs at once. Two types of intrusions were identified: (i) sharp thin intrusions, closely accompanying extrusions and (ii) rather shallow and wide intrusions. TEM observations after 100 cycles revealed both fresh (Fig. 5.26b) and well-developed (Fig. 5.26c) PSMs. Fig. 5.26b shows a pronounced solitary extrusion accompanied by a 60-nm-deep intrusion on one side. A more developed PSM, consisting of a cluster of extrusions and intrusions, is shown in Fig. 5.26c. Its structure is more complicated as it includes several intrusions on one side and also amid the PSM.

With the increasing number of elapsed cycles, microcracks formed. First undeniable microcracks initiating at the surface and propagating further in the bulk were observed after 100 cycles. A FIB cross-section in Fig. 5.26a–c revealed microcracks initiated on the surface, probably from the tips of the intrusions. They ran parallel to the primary slip plane and their lengths were 230 nm and 530 nm (estimated from details in Fig. 5.26a). Due to additional cycling (500 cycles in total), the cracks grew (see Fig. 5.27a). The secondary slip system was found to contribute to the surface relief evolution too as shown in Fig. 5.27b. The surface was decorated by densely distributed, complex-shaped PSMs with thin parallel intrusions on one or both sides (Fig. 5.27c) which developed into microcracks (Fig. 5.27d) in several cases. At the first growth stage, the microcracks tended to propagate along the primary slip plane.

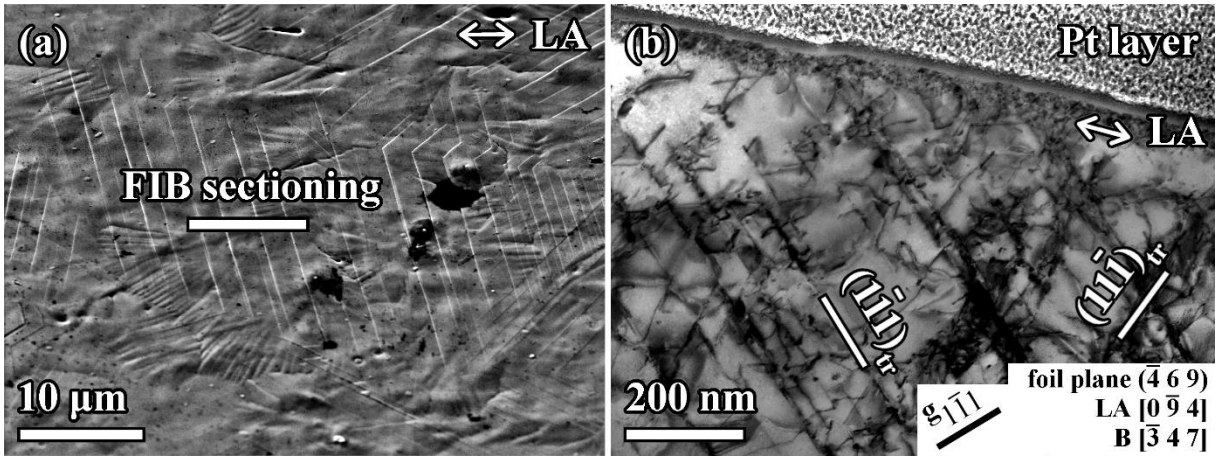

Fig. 5.23. Slip bands and related features on the specimen surface of solutionised René 41 superalloy cycled with ε_a = 0.8% at RT for 1 cycle. (a) SEM micrograph showing slip markings on the specimen surface. The FIB sectioning mark indicates the position from which the lamella was extracted. The cross-section is parallel to the loading axis (LA). (b) STEM micrograph showing slip bands along the traces of {111} planes and a compressive slip step atop a slip band. Reproduced from [34].

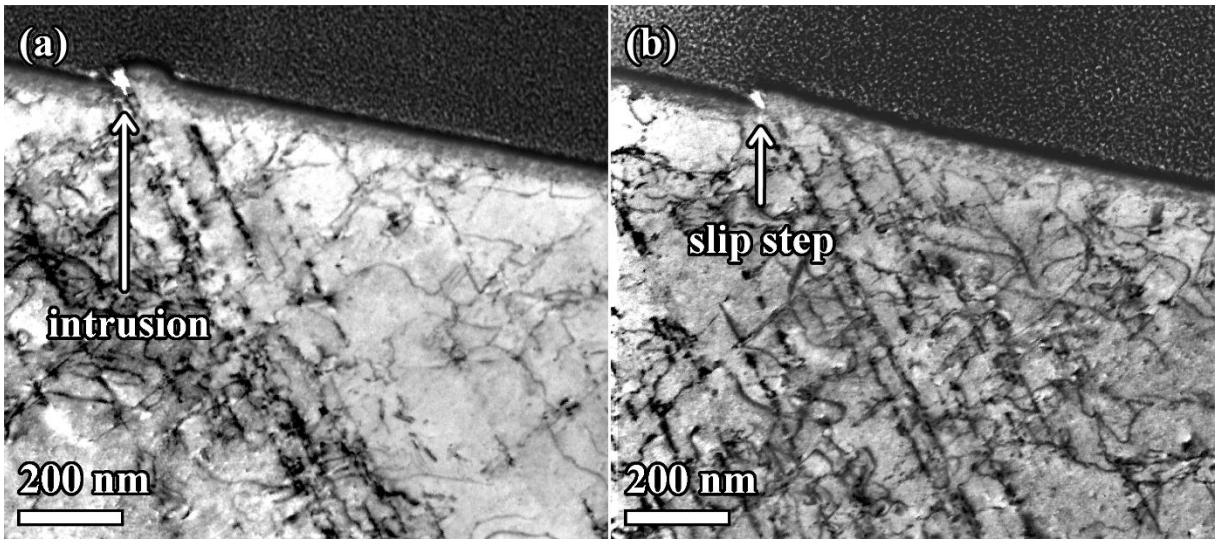

Fig. 5.24. STEM micrographs of solutionised René 41 superalloy cycled with ε_a = 0.8% at RT for 10 cycles. (a) An extrusion with parallel intrusion on one side of the extrusion. (b) A compressive slip step on the surface. Reproduced from [34].

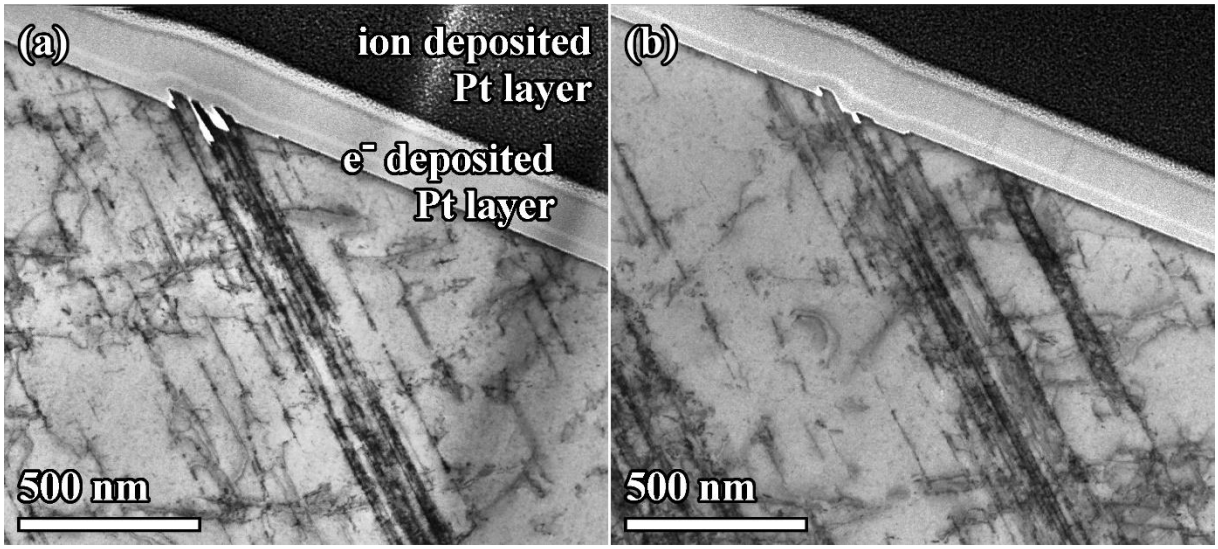

Fig. 5.25. STEM micrographs of solutionised René 41 superalloy cycled with ε_a = 0.8% at RT for 30 cycles. (a) A macro-PSM consisting of several extrusions and intrusions atop a macro-PSB consisting of several PSBs separated by thin slabs of the matrix. (b) Slip steps, an extrusion, and an intrusion on the surface. The arrow points at a macro-PSB resembling ladder-like PSBs known from single-phase fcc metals. Reproduced from [34].

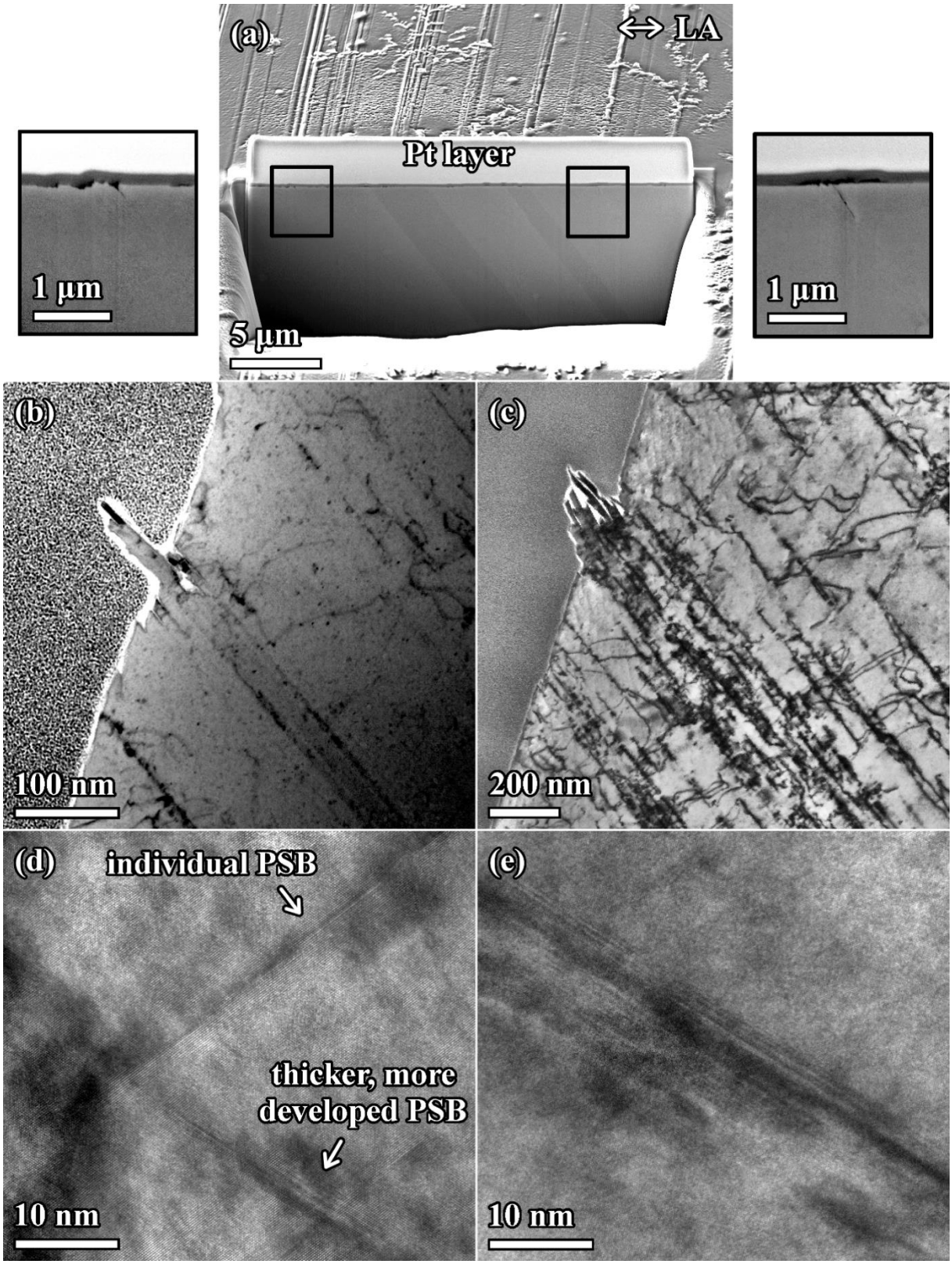

Fig. 5.26. Surface relief and the underlying dislocation structure in solutionised René 41 superalloy cycled with ε_a = 0.8 % at RT for 100 cycles. (a) SEM micrograph of a cross-section with microcracks initiated at the surface. (b–c) TEM micrographs showing (b) a solitary extrusion with an intrusion on one side and slip steps on the other, and (c) a well-developed macro-PSM. The TEM lamella observed in (b) and (c) was extracted from different locations than shown in (a). (d–e) HRTEM micrographs taken in [110] zone showing (d) individual PSB with a thickness over only a few atomic planes and a thicker, more developed PSB, and (e) adjacent PSBs forming a macro-PSB. Images a–c reproduced from [34].

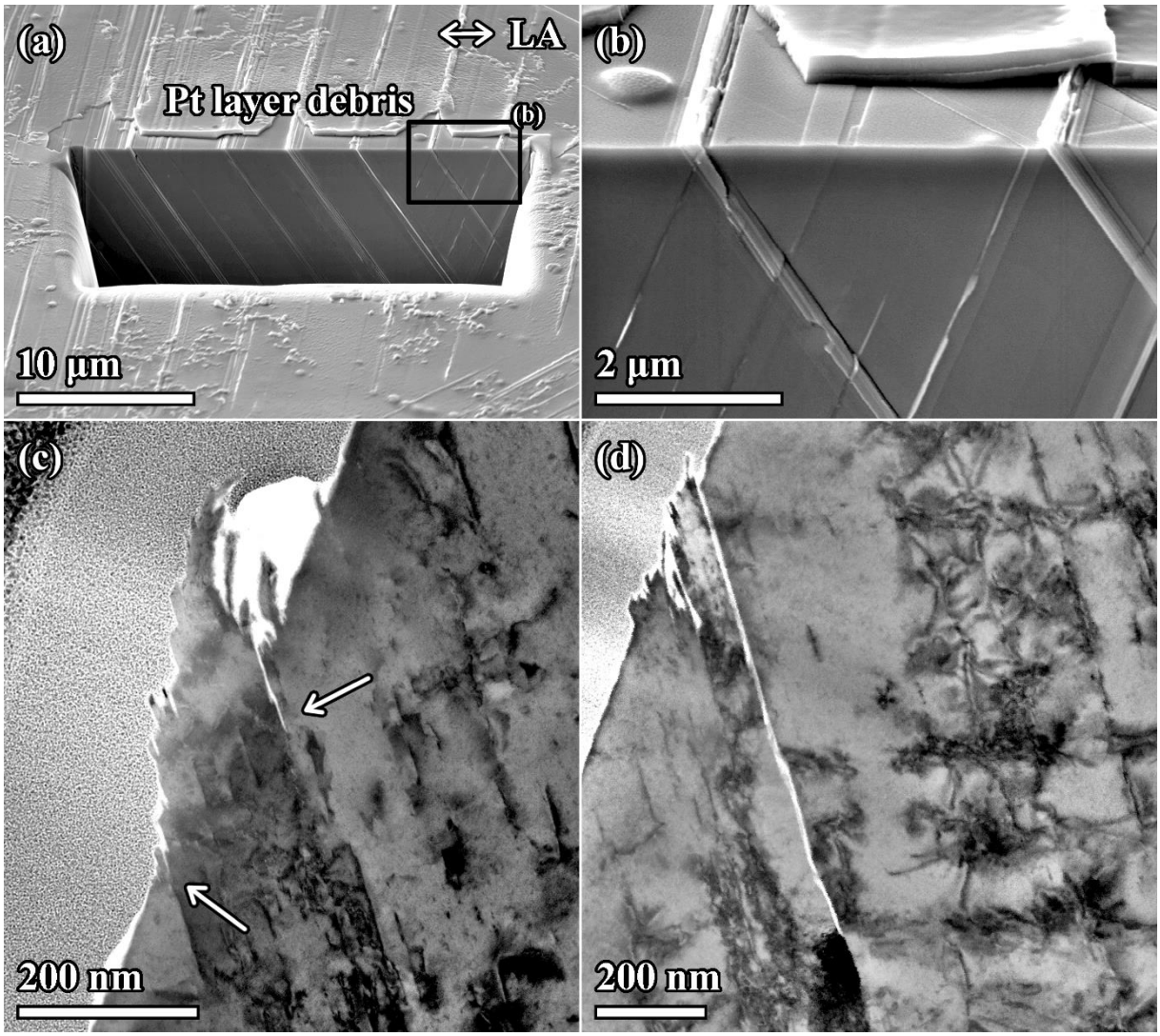

Fig. 5.27. Microstructural evolution of solutionised René 41 superalloy cycled with ε_a = 0.8 % at RT for 500 cycles. (a–b) SEM micrographs showing a cross-section with PSMs. Protective Pt layer delaminated. Microcracks initiated from a PSM and ran along the primary slip plane. The detail in (b) shows a contribution of a secondary slip plane. (c–f) TEM micrographs show the internal structure of macro-PSMs and the underlying dislocation structure. (c) A cluster of extrusions with intrusions on both sides pointed out with arrows. (d) A cluster of extrusions with intrusions in the middle and on one side. Microcrack originating from the PSM and running along the slip plane. Reproduced from [34].

5.4.2 Aged René 41 superalloy

Fig. 5.28a shows PSMs, and the underlying planar dislocation arrays (slip bands) related to them, after one symmetrical cycle using TEM. At this point, the PSMs comprised compressive (Fig. 5.28b) and tensile (Fig. 5.28c) slip steps, as well as early solitary extrusions (Fig. 5.28d). It appears the early extrusion shown in Fig. 5.28d was formed by two consecutive slip events, firstly resulting in the formation of the tensile slip step in the tensile half-cycle and secondly, the compressive slip step in the compressive half-cycle. PSBs were found in the bulk as well as along the twin boundaries. Besides, it is clear from Fig. 5.28a that the secondary slip system was active from the beginning of the fatigue testing. However, only the primary slip system was found to contribute to the evolution of slip markings by then.

After 10 cycles, the PSMs became more pronounced as documented in Fig. 5.29a showing an already well-developed extrusion, formed as a result of repeated dislocation slip in slip bands which can be thus identified as PSBs. No intrusions were observed. The planar PSBs were found to interact with the γ' precipitate microstructure, resulting in precipitate shearing as shown in Fig. 5.29b.

The evolution of both the surface relief and the underlying internal dislocation structure progressed with the number of elapsed loading cycles. PSBs often formed larger clusters (macro-PSBs) which emanated on the surface as macro-PSMs. Fig. 5.30 shows several examples of PSMs with their internal structure and related features underneath. Generally, the PSMs (or macro-PSMs) are formed atop the PSBs (or macro-PSBs). Similar to the solutionised material, the PSMs were complex in shape as several PSBs participated in their formation and subsequent evolution. Only after 100 cycles, the secondary slip system was found to contribute to the surface relief evolution as documented in Fig. 5.30a and in Fig. 5.30b in greater detail. Typically, the PSMs comprised extrusion clusters with intrusions either on one side (Fig. 5.30c) or both sides of the cluster. Sometimes, the intrusions appeared amid a PSM, and their growth resulted in a microcrack formation (Fig. 5.30d). Microcracks were found to initiate also directly from the slip steps (Fig. 5.30e), with no distinct extrusions or extrusions having been formed at the respective sites. That can, however, be misleading as the thin TEM lamella represents only a section of a grain, hence the real initiation site may be elsewhere. Besides, atypical PSM shapes were observed too. Fig. 5.30e shows a wide sharp-shaped deepening. HRTEM detail in Fig. 5.30f directly relates the slip step to the thin PSB. Furthermore, the PSBs which altogether produce the macro-PSM shown in Fig. 5.30e were found to be separated by slabs of the matrix.

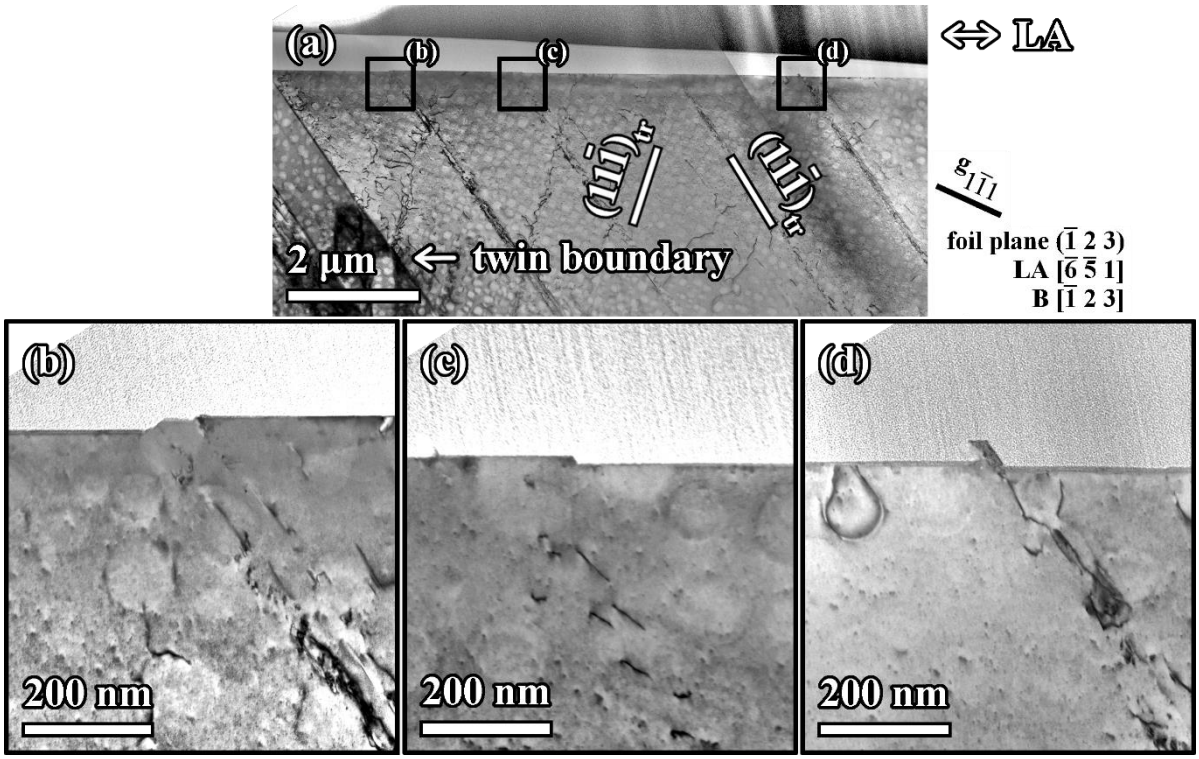

Fig. 5.28. STEM micrographs showing slip features on the specimen surface of aged René 41 superalloy cycled with ε_a = 0.8 % at RT for 1 cycle. (a) Overview of cyclic slip localisation after 1 cycle. The secondary slip system was activated. (b) Compressive slip steps and corresponding dislocation arrays underneath the surface. (c) Tensile slip step in detail. (d) Solitary extrusion and the dislocation arrays underneath the surface. Reproduced from [34].

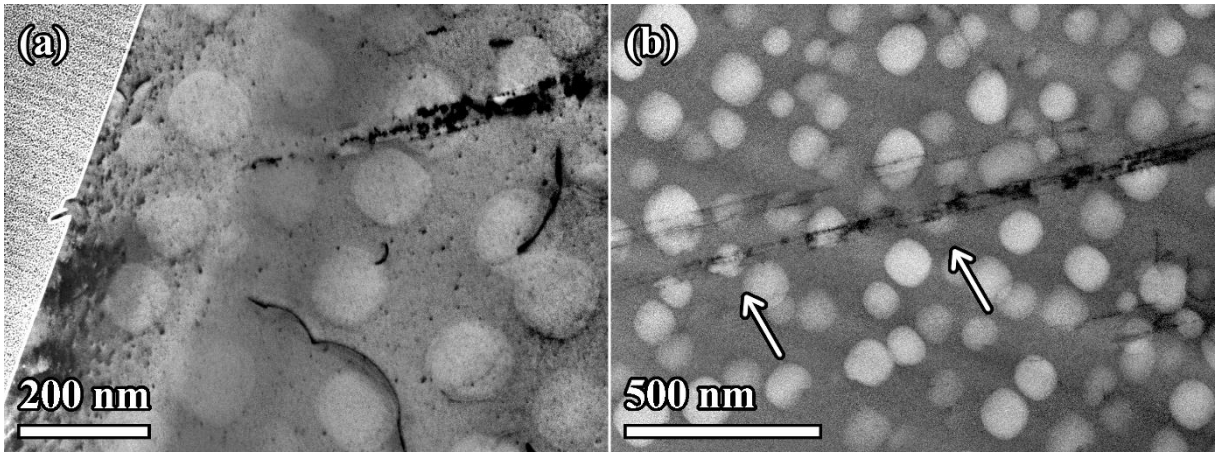

Fig. 5.29. STEM micrographs of aged René 41 superalloy cycled with ε_a = 0.8 % at RT for 10 cycles. (a) An extrusion and corresponding PSBs in the bulk underneath the surface. (b) Precipitate shearing (pointed out by arrows) by the intensive slip band. Reproduced from [34].

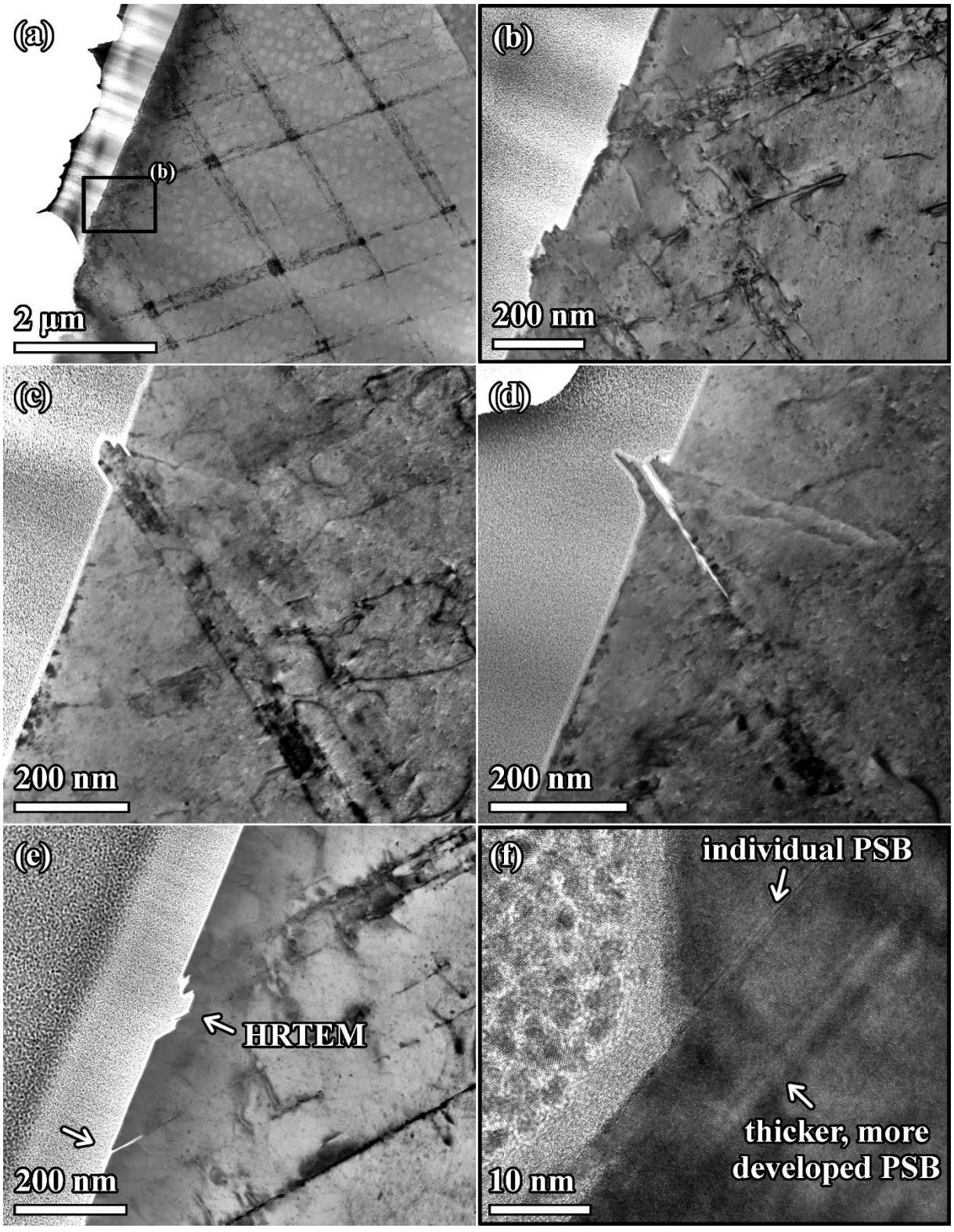

Fig. 5.30. STEM micrographs of aged René 41 superalloy cycled with ε_a = 0.8 % at RT for 100 cycles. (a–b) Cyclic slip localisation in two slip systems. Contribution of two slip systems to surface relief evolution in detail in (b). (c) An extrusion with an intrusion on one side. (d) Microcrack initiated from an intrusion amid a PSM. (e) A microcrack at the slip step and a wide deepening comprising a cluster of slip steps. (f) HRTEM detail taken in [110] zone of the area marked in (e), showing a slip step with corresponding thin individual PSB spanning over only a few atomic planes, and a thicker, more developed PSB separated by a relatively thick slab of the matrix. Images a–e reproduced from [34].

6 Discussion

6.1 Initial state

The initial microstructure of René 41 superalloy exhibited low dislocation content (see Fig. 5.1c for the solutionised and Fig. 5.3c for the aged alloy) due to heat treatment at temperatures sufficiently high to recover high dislocation density introduced by forging. The grain size difference between the two states is considered negligible as it lies within statistical error, and there is no principal reason for grain size change due to ageing treatment at 760 °C.

Several secondary phases were recognized. Unlike Collins *et al.* [103], σ and μ phases were not observed in this work. The presence of borides in René 41 (see M_3B_2 in Fig. 5.4) has not been reported before. From the variety of carbonitrides and carbides observed in this work (see Fig. 5.2 and Fig. 5.4), namely Ti(C,N), MC, M_6C and $M_{23}C_6$ ($M_{23}C_6$ were observed only after the ageing treatment), M_6C is considered the most important as it strengthens the grain boundaries and, in comparison to $M_{23}C_6$, it is stable at high temperature [46]. This corresponds to the conducted observations witnessing only a scarce population of secondary phases other than M_6C. The relatively large M(C,N) phases provide precipitation strengthening to the matrix.

Aging treatment introduced spherical γ' precipitates with two precipitate diameters of 22.8 nm (with a volume fraction 42.6%) and 98 nm (32.6%). As Reppich *et al.* [79] pointed out, the transition from precipitate shearing to Orowan looping may appear in a wide range of precipitate diameters surrounding the critical diameter, which falls within, e.g., 60–85 nm for C263 superalloy [104], 55–65 nm for Nimonic PE16 and 120–270 nm for Nimonic 105 [79]. It should be noted that the precipitate size, which conveys maximum strength upon the material, is a little lower than the transition value [79]. Since the critical precipitate diameter is unknown for René 41, one can only estimate precipitate shearing to be a dominant mode, in accordance with the bypass mechanism map by Chatterjee *et al.* [105].

6.2 Lifetime and damage

6.2.1 Room temperature

From the service point of view, Basquin (stress-related) plots such as those shown in Fig. 5.5a usually provide an adequate comparison of tested materials. The introduction of γ' to the microstructure has a positive impact on the fatigue performance of René 41 superalloy. At a given stress level, the aged material performs markedly better. In comparison to the solutionised material, the aged material exhibits much higher cyclic stresses at the expense of material plasticity (see the Coffin-Manson plastic strain-related plot in Fig. 5.5b). Lower plastic strain amplitude and higher cyclic stresses correspond to the shorter fatigue life of the aged material at a given total strain amplitude. René 41 in the solutionised state is thus desirable in applications potentially imposing high plastic strain, such as welding [101].

In both thermodynamical states, room temperature damage was fatigue-dominated, as documented in Fig. 5.13 for the solutionised and in Fig. 5.16 for the aged material. Fracture surfaces exhibited multiple crack initiation, and contained striations, indicating transgranular fatigue crack propagation, which is typical for superalloys tested at room temperature [22, 33, 69], although some alloys such as Nimonic 80A exhibit tendencies to intergranular cracking [106]. The inspection of polished specimen surfaces revealed extensive roughening by PSMs (Fig. 5.14a) with numerous cracks along them (see Fig. 5.14b–e), in agreement with previous investigations [22, 33, 69, 107]. The early microcracks were found to follow an active

slip plane (Fig. 5.17f–i), sometimes with a slight deviation within a corresponding macro-PSB (Fig. 5.27b). Clearly, in room-temperature low-cycle fatigue, PSMs are key to fatigue crack initiation, which applies generally to fcc metals [37, 108]. Since the occurrence of PSMs is a manifestation of cyclic plastic straining of the material, it can be concluded that the room-temperature fatigue lifetime of René 41 superalloy in both solutionised and aged states is governed by plastic strain amplitude.

6.2.2 High temperature (800 °C)

A significant drop in fatigue lifetime at 800 °C is apparent in both Basquin and Coffin-Manson life representations. The fracture surfaces are predominantly intergranular (Fig. 5.19b), which is indicative of a damaging mechanism other than fatigue. Intergranular cracking has been widely reported in superalloys subjected to fatigue at high temperatures [22, 33, 70]. This can also be reconciled with a relatively high content of Mo in René 41, which increases susceptibility to intergranular cracking [46]. Fig. 5.19c shows the specimen surface covered by a non-uniform oxidic layer (see Fig. 5.19e) with roughly the same composition as observed by Jiang *et al.* [87]. The oxide layer appeared thicker at grain boundaries (Fig. 5.19c) and at other weak points of the microstructure, such as twin boundaries and PSMs (Fig. 5.20c). Extensive subsurface damage (Fig. 5.20a) occurred mostly along the grain boundaries, where the oxides formed in voids along the grain boundaries (Fig. 5.20b), and at the newly formed microcracks. The voids could form due to creep [109], or due to decohesion at the carbide/matrix surface [33], however, convincing proof of the origin of the voids is missing in the present study. Since the extent of subsurface oxidation (10–15 μm at ε_a = 0.5%) is significantly higher than predicted by load-free stability tests [46], it can be assumed that cyclic stresses accelerate the penetration of oxygen. This altogether indicates an interaction of fatigue (cyclic plasticity via PSBs/PSMs on the surface, Fig. 5.20f), environmental (surface oxidation, Fig. 5.20c) and creep (voids along the grain boundaries in Fig. 5.20e) damage. Since the cracking of the oxidised grain boundaries is prevalent (see Fig. 5.22), it can be concluded that the low-cycle fatigue lifetime of René 41 superalloy at 800 °C is determined by the extent of environmental attack.

Surface oxide formation is promoted by elements with high affinity to oxygen such as Cr, Al and Ti. The oxides are brittle, and relatively low stresses are needed to crack them. Such oxide cracking is pointed out in Fig. 5.19d. This shows that the principal acting mechanism is grain boundary oxidation, in agreement with other studies on superalloys [33, 70, 81, 85, 87]. Cracking along twin boundaries and slip bands (producing PSMs) occurs too, but grain boundary cracking is more favourable due to the easy diffusion of oxygen along them. The diffusion of oxygen along the grain boundaries, resulting in internal oxide formation [110–111], is promoted by high stresses [84] and positively influenced by temperature concerning Arrhenius-type dependence. The source of elements for internal oxide formation can be the surrounding matrix (primarily Cr [112], which is getting depleted as shown in Fig. 5.19e), and secondary phases (e.g., TiC might provide Ti for internal Ti oxides [113]).

Once the crack is initiated, the propagation along the grain boundaries is promoted by internal oxidation and newly formed oxide layers on the crack surfaces. Coarsened M_6C carbides shown in Fig. 5.21e might further weaken the grain boundary strength. As a result, there is an interface decohesion and the fracture is intergranular. The presented results agree with the previous study on the embrittlement of René 41 superalloy by Prager and Sines [114]. The detrimental effect of oxygen is suppressed in a vacuum, resulting in transgranular failure mode [84, 114]. The authors [114] found that larger precipitates decrease the embrittlement sensitivity. It can thus be assumed that the overaged material shall perform better than the peak-aged one at high

temperatures. However, the effect of precipitate size on the high-temperature properties was not investigated in the presented study.

6.3 Cyclic deformation behaviour

6.3.1 Solutionised René 41 superalloy cycled at room temperature

The evolution of cyclic stresses of solutionised René 41 superalloy, shown via cyclic hardening/softening curves in Fig. 5.6a, represents a typical behaviour of γ'-free superalloys cycled at room temperature, such as solid solution-strengthened superalloys IN625 [115], Haynes 230 [116] and Hastelloy-X [117]. All these materials witness initial rapid cyclic hardening. This corresponds to the gradual increase of stress amplitude, as well as the narrowing of the hysteresis loop (compare the 1st and the 30th cycle in Fig. 5.7a) which corresponds to a decrease in plastic strain amplitude. The occurrence of cyclic hardening can be explained by high strains promoting dislocation multiplication and dislocation interactions occurring in both matrix and the newly formed slip bands. More pronounced cyclic hardening at high strain amplitudes is due to multiple slip (see Fig. 5.23b and Fig. 5.27b), which results in decreased free glide path between slip band intersections. The hardening culminates at about 2% of fatigue life for ε_a = 1.2%, and the fraction of fatigue life it takes to reach the stress amplitude maximum decreases with the strain amplitude. The absolute number of cycles to reach maximum cyclic stress, however, increases with the decreasing strain amplitude, which can be explained by the less frequent formation of slip bands due to lower imposed strain amplitude. Unlike Hastelloy-X [117], solutionised René 41 tends not to saturate the cyclic response but rather evolve into cyclic softening. This can be ascribed to the localization of cyclic slip into the intensive PSBs (see the PSBs after 30 cycles at ε_a = 0.8% in Fig. 5.25), which becomes increasingly dominant since dislocation slip within PSBs requires lower stress in comparison to the slip in the matrix. PSBs gradually widen by activation of neighbouring slip planes (indicated in Fig. 5.26d), and the material softens until fracture. This is further supported by the comparison of the internal dislocation structure after 30 cycles (Fig. 5.25) and after 100 cycles (Fig. 5.26) which witnesses higher dislocation density and wider PSBs with an increasing number of cycles.

The experimental curves obtained via the analysis of the hysteresis loop using the statistical approach [8] agree well with the evolution of cyclic stresses and the microstructure. As only one phase is deformed in solutionised René 41 superalloy, there is only one peak in the plot (Fig. 5.7b) of experimental second derivatives, consistently with Polák *et al.* [13–14]. No striking differences were noted between the plots of tensile and compressive half-loops. The evolution of the peak (Fig. 5.8a–b) corresponds to the observed cyclic behaviour, as the peak first shifts towards higher fictive stresses (cyclic hardening), but eventually shifts back towards lower stresses again (cyclic softening). The lowering and widening of the peak indicate the widening of the spectrum of critical internal stresses following the intensification of long-range stress fields due to the evolution of dislocation content in respective microvolumes. The effective stress is rather low (below 100 MPa at half-life as shown in Table 8), similar to one-phase steels [14]. This indicates the low occurrence of short-range stress fields hindering the dislocation movement.

6.3.2 Aged René 41 superalloy

6.3.2.1 Room temperature fatigue

In comparison with the solutionised state, cyclic stresses attained by the aged material are indeed much higher (see Fig. 5.6a–b) because of the dispersion of spherical *γ'* precipitates in the microstructure (Fig. 5.3d–e), which represent a principal obstacle to dislocation movement and thus increase the flow stress (Fig. 5.5c). The cyclic deformation behaviour of the aged René 41 is shown in Fig. 5.6b. It exhibits initial cyclic hardening followed by softening until fracture, similar to other wrought Ni-based superalloys such as Waspaloy [69, 71], Nimonic 80A [107] and IN718 [68–69]. In agreement with these studies, the initial cyclic hardening becomes less pronounced with decreasing plastic strain amplitude. This explains the complete absence of the cyclic hardening stage at low total strain amplitude (ε_a = 0.5%), due to which cycling is realised mostly in the elastic region and very little plasticity is necessary to accommodate the cyclic stress. Unlike these alloys, the cyclic hardening period exhibited by René 41 is notably shorter and far less pronounced, which is rather typical for heavily-deformed materials with pre-existing dislocation structure such as cold-worked steels [118–119]. The dislocation interactions which led to the initial rapid hardening in the solutionised state play a less significant role in this case. The effect of cyclic slip localisation on the cyclic stress-strain response in the aged superalloy seems similar to the solutionised counterpart as follows from the comparison of softening ratios in Table 6, even though the overall number of PSBs is lower in the aged material, as implied by the lower number of initiation sites at PSBs over the same distance from the fracture surface (Fig. 5.22) and, more importantly, the decreased plastic strain amplitude (compare for identical total strain amplitudes in Table 6). This is indicative of other mechanisms contributing to cyclic softening. Shearing of the *γ'* precipitates, which relaxes coherency strains [120] and reduces the effective precipitate size (Fig. 5.29b) can be considered a worthy candidate. A stronger cyclic softening in the early stages of the fatigue life (see Fig. 5.6b) hints that shearing of *γ'* apparently plays a significant role only in this period, which is further analysed in the next paragraphs.

The experimental curve of the second derivative exhibits two separate peaks, which corresponds to the deformation of two phases in multiphase material [15–16, 121]. It should be noted that the difference between compressive and tensile half-loops is not considered important, while the evolution of the respective peaks is. In the present work, the peaks can be attributed to the *γ* matrix and the *γ'* precipitates, which both can be sheared. While the first peak (at lower fictive stresses, attributed thus to the matrix) gradually grows and shifts towards lower fictive stresses, the second peak (at higher stresses, attributed thus to the *γ'* precipitates) vanishes completely in less than 10 cycles. The evolution of the first peak is indicative of softening of the matrix, which is well in agreement with observations on cyclic slip localization into PSBs (see Fig. 5.17a–b). The effective stress of the matrix is notably higher than in the solutionised state (by about 100–200 MPa as shown in Table 6), which can be related to the introduction of local obstacles (*γ'* precipitates) to the dislocation movement. Also, the strength of the matrix is significantly increased, which is manifested in the shift of the corresponding peak from ~450 MPa in the solutionised state (Fig. 5.7b) to ~750 MPa in the aged state (Fig. 5.9b). Since the shift in peak position (~300 MPa) surpasses the difference of effective stress (100–200 MPa), it can be concluded that the contribution of long-range stress fields, i.e., dislocation structure is higher in the aged state. This can be reconciled with the introduction of matrix/precipitate coherency strain [120]. The evolution of the second peak witnesses a substantial decrease in the number of deformed microvolumes with high fictive stress. This result indicates that *γ'* precipitates are sheared in larger numbers only in the first few cycles. Early shearing of the *γ'* observed in this study is shown in Fig. 5.29b. The result

also indicates that later on, deformation is mostly confined to the matrix, and only the underaged or previously sheared precipitates with lower flow stress are deformed too. It can be assumed that the majority of slip bands is formed at the beginning of the fatigue life, they shear the precipitates as they grow across a grain, and the slip within the slip bands intensifies over the fatigue life. This assumption is in agreement with detailed studies on the cyclic slip in Ni-based superalloys by Petrenec *et al.* [21] and Mello *et al.* [122]. It is reasonable to assume that the precipitates that interfere with slip bands are continuously sheared until they impart almost no resistance to further dislocation movement, hence the second peak diminishes. Shearing of the γ' precipitates is often considered an important mechanism contributing to the observed softening behaviour [68–69]. However, as follows from the analysis of the hysteresis loops (Fig. 5.10) and a scarce shearing of the *γ'* observed *post-mortem* in TEM (Fig. 5.18), this does not seem to be the case for René 41 superalloy, which witnesses considerable shearing of the *γ'* only in the first few cycles. This result suggests that in the fatigue-related material design of superalloys, a higher focus should be paid to the strengthening of the matrix.

6.3.2.2 Effect of high-temperature exposition (800 °C)

As shown in Fig. 5.5b, although the levels of plastic strain amplitude attained at 800 °C at given total strain amplitude are similar to room temperature levels, cyclic stresses are notably lower (e.g., by about 300 MPa for $\varepsilon_a = 0.5\%$). This is related to lower flow stress at 800 °C as indicated by cyclic stress-strain curves shown in Fig. 5.5c, and lower effective modulus shown in Table 8. Although cyclic stress response (see Fig. 5.6c) is rather stable at low strain amplitudes, there is a tendency to cyclic softening with increasing strain amplitude, which can be related to plastic straining induced by high cyclic stresses. The cyclic deformation behaviour of René 41 at 800 °C is different from many other wrought alloys which often exhibit initial cyclic hardening (e.g. Waspaloy [70], GH4742 [123], 718 Plus [124] or Haynes 230 [125]). From the wrought alloys, only a few exhibit similar behaviour of continuous cyclic softening since the first cycle (e.g. René 77 [126] and Udimet 720 Li [127]). This behaviour is rather reported for other metallurgical processes, such as powder-processed RR1000 superalloy [128] or cast IN792-5A [15, 129] and IN738LC [130]. Softening behaviour is promoted by localization of cyclic slip in PSBs (see Fig. 5.21c–d) and by shearing of *γ'* precipitates (Fig. 5.21a,b,d), in agreement with numerous studies on high-temperature deformation of Ni-based superalloys [22, 33, 43, 63, 70–71].

In comparison to the room temperature, deformation at 800 °C is more homogeneous, which is manifested in frequent shearing of γ' precipitates (Fig. 5.21a–b) and a lower tendency to form slip bands (Fig. 5.21a). Slip bands were observed exclusively along octahedral planes. Contrary to room temperature results, analysis of the hysteresis loop suggests that shearing of *γ'* is taking place throughout the fatigue life, however, its significance gradually decreases, which is manifested in the lowering of the second major peak in the second derivative plot shown in Fig. 5.12. There is still a strong influence of the first cycle as depicted by the evolution of the initially massive second peak in second derivative plots of compressive half-loops in Fig. 5.12b. The respective first-cycle peak for the tensile half-loop (Fig. 5.12a) is significantly lower, which can be attributed to the fact that the first full tensile half-cycle occurs indeed only after the first compressive half-cycle (the initial tensile load is thus not covered by the analysis). The initial evolution of the second peak with the number of cycles is unambiguous because tensile and compressive half-loops exhibit different shifts, and thus it is difficult to interpret. The following peak stress oscillation within 1100–1200 MPa may be inflicted by random precipitate-dislocation interactions outside of slip bands. Together with the continuous decrease of the corresponding peak, this would imply that the majority of PSBs are nucleated early in

the fatigue life, which is supported by previous studies on cyclic slip localization [21, 122]. Nonetheless, as the second peak decreases, the other peak heightens, which indicates that the deformation of the matrix is intensifying throughout the fatigue life. There is also a minor shift of the respective peak towards lower fictive stresses, which indicates cyclic softening of the matrix. Again, this can be attributed to the cyclic slip in PSBs, which shear away the precipitates standing in the way, until they offer no resistance to the cyclic slip.

The effect temperature has on the shape of the hysteresis loop is clear from the comparison of second derivative plots in Fig. 5.9b and Fig. 5.11b. At 800 °C, the initial drop of the second derivative, corresponding to the rapid relaxation of plastic strain under decreasing effective stress in all plasticized microvolumes [16, 121], is shifted towards higher fictive stresses. Effective stresses, however, exhibit a drop of about 50 MPa (see Table 8) in comparison to room temperature, consistently with the experimental work of Pettinari-Sturmel *et al.* [131], who investigated temperature-dependent friction stress due to short-range order in the matrix of several superalloys. On the other hand, inconsistency with Petrenec *et al.* [16] is presumably caused by an error on the authors' side due to an inaccurate fitting of a corresponding small peak. It can, however, be concluded that the contribution of effective stress (arising from short-range obstacles which can be overcome by thermal activation) to the overall cyclic strength is more significant at 800 °C since the related peak (corresponding to the distribution of critical internal stresses) is centred at notably lower fictive stress (~500 MPa, hence the drop from room temperature value is about 300 MPa). The lower contribution of the dislocation structure in the matrix (manifested in the distribution of critical internal stresses) can be reconciled with easier cross-slip and non-conservative dislocation movement at high temperatures [22], which is supported by STEM images showing more homogeneous deformation at 800 °C (see Fig. 5.21a–b). Considering the evolution of the second peak corresponding to the γ' precipitates, the presented data are in full agreement with the work of Petrenec *et al.* [16]. Effective stresses were found to be substantially lower at 800 °C (by about 200–300 MPa as shown in Table 8). TEM inspection of dislocation structures at room temperature (Fig. 5.18) and 800 °C (Fig. 5.21), witnessing far more frequent shearing of the γ' precipitates at 800 °C, indicates a presence of a principal obstacle to dislocation movement in the γ' phase at room temperature. Hence, the drop in effective stress can be explained by the presence of immobile dislocation configurations such as Kear-Wilsdorf locks at room temperature [22]. Since the difference in cyclic stress levels is lower (about 160 MPa at half-life, see Table 6) than the difference in effective stresses (about 200–300 MPa, see Table 8), it can be concluded that the contribution of internal stress of the γ' precipitates at the beginning of the fatigue life is notably lower at 800 °C. The higher participation of the matrix microvolumes in carrying the plastic strain at room temperature (see the sole peak in Fig. 5.9b and the dominant peak in Fig. 5.10) agrees well with this explanation.

6.4 Cyclic slip localization and the resulting surface relief

The cyclic slip localization and the resulting PSMs play a significant role in fatigue crack initiation at room temperature (see Fig. 5.22) while at 800 °C, their influence on fatigue lifetime is negligible due to grain boundary oxidation. The only notable features are the bulgy oxides appearing at the PSMs, similar to the ones observed at grain boundaries (Fig. 5.19c–d). Also, it seems that PSM growth is suppressed by the surface oxidic layer (Fig. 5.20f). The prevalence of environmental effects over fatigue mechanisms is typical for superalloys at this temperature [22, 43]. Hence, in the following two chapters, only the room temperature results on the evolution of PSMs are discussed.

The electron microscopy observations complemented by the analysis of the hysteresis loop strongly indicate that the majority of slip bands at room temperature are nucleated very early in the fatigue life. In agreement with previous studies on the formation of early PSBs in Ni-based superalloys [21, 122, 132–133], the localisation of cyclic slip in René 41 superalloy was observed already in the first cycle. Evidence shown in Fig. 5.23b for solutionised René 41 and in Fig. 5.28a for aged René 41 displays the planar arrays of dislocations – slip bands – which later develop into PSBs as shown in Fig. 5.25a–b. Slip bands are thin (initially spanning over only a few atomic planes as apparent from Fig. 5.26d and Fig. 5.30f) due to the slip planarity promoted by the low stacking fault energy of superalloys [51]. The PSBs do not assume the ladder-like structure in René 41 superalloy and, presumably, all superalloys. Common fcc metals exhibit ladder-like PSBs with thicknesses larger by about 2 orders of magnitude: 1-2 μm in Cu [2] and about 250–750 nm in austenitic steels [20].

As a consequence of continuous cyclic straining, dislocation density in the bands increases and point defects are produced due to dislocation interactions. When slip is concentrated in the slip bands over several cycles, they can be identified as PSBs. Slip accommodation in the slip bands imposes the formation of characteristic surface relief in the form of slip markings which become PSMs corresponding to the respective PSBs. This is clear from numerous observations conducted in this study (see e.g. Fig. 5.25). An exact point at which slip bands can be considered as PSBs, and slip markings as PSMs, is difficult to define. Due to additional stress fields [134], slip is activated also on the planes in the close vicinity of already present PSBs (compare the individual PSBs in Fig. 5.23b with the wide cluster of adjacent PSBs in Fig. 5.25a) or twin boundaries (since they lie on a slip plane too), in agreement with observations conducted by Miao *et al.* [74, 135]. That way, PSBs widen (no individual PSB wider than 10 nm was observed in this study), new PSBs form closely, and the adjacent PSBs form a cluster – macro-PSB (Fig. 5.26e), which altogether produces a single macro-PSM.

PSBs are bulk features and carry information about the loading history. PSMs observed on the surface may become complex in shape as several individual PSBs participate in the evolution of a single (macro-)PSM. The structural complexity, although unrecognized at that time, was indicated by interferometric measurements conducted by Hong and Laird [134]. Therefore, it is difficult to assess the contribution of an individual PSB to the surface relief evolution, and HRTEM is needed (see the thin PSB and the corresponding slip step in Fig. 5.30f). This is clear from Fig. 5.30f, which shows only a portion of a PSM, which is produced by several PSBs separated by slabs of the matrix. As the slip band width is low and the thicker macro-PSB structure is about to form later, the PSMs first egress in the form of slip steps on the surface (see Fig. 5.23b or Fig. 5.28), which might happen very early in the fatigue life depending on the imposed plastic strain amplitude. As follows from the detailed analysis using the interruptions to the fatigue test, further cyclic straining results in the widening and growth of already present PSMs (see e.g. the PSM after 100 cycles in Fig. 5.26), and new PSMs are formed too (notice the featureless surface above some PSBs in Fig. 5.25a). The later appearance of some PSMs suggests a continuous growth of the corresponding underlying PSBs across the volume of the grain until a surface is reached, and the excess slip subsequently produces surface relief. The growth of already present PSMs is closely related to the increase in dislocation content in PSBs as evident from the comparison of Fig. 5.24 and Fig. 5.25, supported also by observations of León-Cázares *et al.* [132].

As more PSBs participate in the evolution of a single surface feature, the occurrence of extrusions and intrusions is more likely. Early extrusions may be spotted even after the first cycle (Fig. 5.28d) if the conditions are appropriate. Slight changes of contrast in Fig. 5.27c in the extruded part of the PSM indicate that the PSM consists of several extrusions, each possibly

originally linked with the individual PSBs but later intertwined with one another. Thin individual extrusions recognized in the PSM shown in Fig. 5.26c supports this assumption. Sharp intrusions accompanying extrusions appear later, running along the active slip plane. They are present not only beside but also within the extruded part of the PSM. The first intrusion in the solutionised state was detected only after 10 cycles (see Fig. 5.24a) compared to 100 cycles in the aged state (Fig. 5.30c). Intrusions are very fine defects hence they might not be detected by means of SEM when the plastic strain amplitude is low [136]. The difference in the number of cycles to promote intrusion formation is material dependent since specific variables such as the density of edge dislocations affects the evolution of the resulting surface relief [32].

The formation of slip bands corresponding to a secondary slip system was observed even after the first cycle as shown in Fig. 5.23b and Fig. 5.28a. However, its contribution to the surface relief evolution was documented later in the fatigue life (see Fig. 5.27b, Fig. 5.30a,b). This is consistent with a detailed study on the morphology and evolution of slip bands in RR1000 superalloys conducted by León-Cázares *et al.* [132]. This result indicates that even though multiple slip occurs, there is a dominant primary slip system, which produces surface roughness early in the fatigue life and hence mostly determines the occurrence of a fatigue crack [137]. The hardening effect due to multiple slip is indeed more pronounced when more slip systems are activated since the mean free glide length of dislocations is reduced as active planes are intersected [22].

6.5 The structure of PSMs

The experimental evidence provided in this work witnessed PSMs consisting of:

(i) slip steps (Fig. 5.28b–c),
(ii) a cluster of closely-spaced slip steps (Fig. 5.25b),
(iii) a solitary extrusion (Fig. 5.28d),
(iv) an extrusion accompanied by an intrusion on one side (Fig. 5.26b),
(v) a cluster of extrusions with intrusion on one (Fig. 5.30c) or both sides (Fig. 5.27c) of the cluster,
(vi) a cluster of extrusions with intrusions amid PSM (Fig. 5.26c).

The character of slip affects not only the internal structure of PSBs, but also the resulting PSMs. Since PSMs are a result of slip events in the underlying PSBs, the PSMs observed on the surface of René 41 superalloy are correspondingly thin. This is a consequence of slip planarity manifested in the absence of ladder-like PSB structure and significantly thinner PSBs than observed in wavy-slip metals such as Cu [138] and stainless steels [139]. In such materials, PSBs typically exhibit ladder-like structure with a width of about 1 μm, hence the resulting PSMs assume a similar width. The PSM thickness may be larger [138] when PSBs occur close to one another and form thus a macro-PSB with the resulting macro-PSM [20]. In this work, the thickness of the early (macro-)PSMs was gradually increasing up to ~300 nm. In agreement with previous studies on PSM evolution using atomic force microscopy [33, 140], the change in the PSM width was substantial only in the early stages of fatigue life (first ~100 cycles for ε_a = 0.8%), indicating a continuously increasing number of thin individual PSBs involved in the evolution of a single (macro-)PSM. Since the PSM evolution for both wavy- and planar-slip materials is a result of principally identical events, the assumed shapes are similar.

In the following subchapters, the observed PSM structures and shapes shall be discussed with previous observations and their compatibility with the existing models.

6.5.1 Slip steps

It is well-established that PSBs emerge on the polished specimen surface in the form of PSMs, which look like thin lines in SEM images (see e.g. Fig. 5.23a). As revealed by TEM analysis on the specimens during the interrupted test at room temperature, the PSMs first emerge in the form of slip steps on the specimen surface, regardless of the presence of γ' in the microstructure (see Fig. 5.23b and Fig. 5.28). The observations of the early surface evolution correspond well to the predictions based on random slip events in PSBs by Differt *et al.* [27], the computer model by Rosenbloom and Laird [28], and the slip-based model by Tanaka and Mura [25]. Hence, it can be concluded that slip steps form due to dislocations escaping from the underlying slip bands to the specimen surface. Since all these models assumed ladder-like PSB structure, which is not present in the material investigated in this study, it can be argued that the occurrence of slip steps does not rely on the ladder-like dislocation structure of PSBs.

Presented observations strongly indicate that the occurrence of the early PSMs in the form of slip steps is not significantly affected by the diffusion effects, in agreement with the initially low point defect production rate as follows from resistivity measurements on copper [19]. This can be further reconciled with the recent experimental study by Stinville *et al.* [133] who utilised the DIC method to assess the occurrence of the early slip steps in René 88DT superalloy. The authors [133] demonstrated that positive (tensile) slip steps form during the tensile half-cycle due to intensive dislocation slip in PSBs in the underlying bulk and that the slip steps can vanish or even evolve into negative (compressive) slip steps during the subsequent compressive half-cycle. It was reasoned that the dislocations generated in the compressive half-cycle can fully recover a slip step produced during the tensile half-cycle before reaching maximum compression, which results in an increment of slip and consequent negative slip formation. Another hypothesis [133] assumed that should the respective slip band develop in a compressive half-cycle, a negative slip step is formed. Proposed mechanisms explain well the occurrence of positive and negative slip steps observed in this study. If a tensile slip step appears near a compressive slip step, either a deepening or an elevation arises. The deepenings or elevations may appear as soon as in the first cycle as documented in Fig. 5.28d. It follows from the comparison of the slip steps shown in Fig. 5.28b and Fig. 5.28c that the shape of the slip step is directly related to the thickness of the respective slip band. As new PSBs often nucleate closely to the already existing PSBs, the resulting PSMs widen accordingly, and more complex deepenings (Fig. 5.30f) or elevations (Fig. 5.25b) comprising several slip steps can be observed later in fatigue life.

The results of Stinville *et al.* [133] might have been influenced by the adopted experimental procedure, which incorporated interruptions to the stress-controlled cycling at maximum compression stress. Most of the steps observed by the authors later in fatigue life were positive which was probably caused by cyclic creep in stress-controlled cycling. Hence, it can be assumed that strain-controlled cycling is more suitable for this type of analysis. Furthermore, the authors' approach [133] imposes a significant imbalance between tensile and compressive strains in several initial cycles because the cycle is not completed – for instance, in the first cycle, the specimen is subjected to tensile quarter-cycle and compressive half-cycle (similar to Fig. 4.3a). In this work, interruptions at maximum compression strain were performed on the solutionised specimen, and because of the cycle imbalance, the early slip steps were predominantly compressive. On the other hand, the enhanced interruptions at 0% plastic strain adopted for the aged material yielded no such result. It should be, however, noted that the occurrence of positive or negative slip steps evaluated by TEM analysis does not provide means to bring the representative amount of data.

6.5.2 Extrusions and intrusions: observations and models

The more complex shape of PSMs occurring later in the fatigue life indicates that there is another mechanism participating in the PSM evolution. Electrical resistivity measurements performed by Polák [19] indicated that point defects are produced over fatigue life due to dislocation multiplication/annihilation events, and the point defect production rate saturates following the cyclic stress-strain response. Coupled with electron microscopy observations [24], this further indicates that diffusion of point defects occurs to reach local equilibria and plays thus a significant role in the evolution of the PSB and the corresponding PSM as well. The presence of well-developed PSMs exhibiting extruded material (extrusions) and crack-like deepenings (intrusions) was revealed in both solutionised (see Fig. 5.27c–d) and aged (see Fig. 5.29a and Fig. 5.30c) specimens. The PSB and the PSM structures appear to be independent of the performed ageing treatment. The PSMs observed in this work closely resemble a thick (~1 μm) 'macro-PSM' on top of the 'macro-PSB' observed in copper, also termed 'protrusion' by some authors when the macro-PSB protrudes above the original surface [9, 141–142]. However, features observed in this work are notably smaller in scale due to high slip planarity.

At room temperature, surface relief is a preferential site for the initiation of the fatigue crack (see Fig. 5.22). Therefore, the majority of models attempting to describe fatigue crack initiation propose a mechanism leading to the extrusion or extrusion/intrusion formation during cyclic straining. In the following paragraphs, the predictions of individual models shall be discussed with the findings of the present work.

While the occurrence and the shapes of slip steps can be explained well by random slip-based models [27–28], they do not satisfactorily explain the more developed PSMs with extrusions and sharp intrusions. Hence, it can be assumed that the random slip mechanism is rather a complement to other mechanisms which are not random, and that account for the formation of more complicated surface relief in the form of extrusions and intrusions. Random slip models serve well in explaining the surface roughening of PSMs.

Computer simulation using discrete dislocation dynamics [30, 39, 40] can predict the localisation of cyclic plastic strain and the production of small elevations and egressions of the surface for low number of cycles. Unfortunately, due to the limitations in computer capacity, no predictions are available for a high number of loading cycles, and the analyses are overly simplified, e.g., by omitting diffusion effects [40]. Although the results show appreciable variability of the surface relief, which is in good agreement with some of the early experimental observations (e.g. the PSM formed by several slip steps in Fig. 5.25b), there is a significant discrepancy in the PSM shapes observed later in the fatigue life (Fig. 5.26c).

Ma and Laird [142] identified developed PSMs with extrusions on copper single crystals as 'protrusions', which consisted of adjacent PSBs separated by a thin slab of the matrix in between. Authors claimed that protrusions form by a macroscopic displacement of material in the gauge length and the microscopic relative displacements between two adjacent lamellae. The growth of a protrusion was supposed to occur by a shuttling mechanism, i.e., the PSB and the matrix lamellae both slip in the direction of the primary Burgers vector but in a constrained manner due to specimen gripping. On the other side of the crystal, negative protrusions (labelled 'encroachments') should form. In the present work, similar features were observed – 'protrusions' in Fig. 5.25b and 'encroachments' in Fig. 5.30e, and these features were identified as PSMs comprising several slip steps, consistently with the literature [2, 9]. Authors predicted the existence of thin intrusions and possibly cracks within the protrusions, more specifically at the PSB-matrix interface, which is in agreement with many observed intrusions in this work (see e.g. the intrusion amid a macro-PSM in Fig. 5.30d or a more typical intrusion at the

macro-PSB-matrix interface in Fig. 5.30c). Although the work of Ma and Laird [142] is consistent with the observations presented here, the explanations provided by the authors are deemed insufficient since an explanation of the physical events inevitably resulting in the surface roughening was missing completely.

Work presented by Cretegny and Saxena [141] investigated fatigued pure copper using atomic force microscopy. According to the authors, protrusions contain a much higher density of slip bands than regular stand-alone slip band arrangement, well in agreement with the findings of the present work (compare Fig. 5.24b with Fig. 5.25a). The authors suggested that protrusions form by 'the multiplication of active planes within a slip band and not the growth of closely packed slip bands due to cyclic deformation'. While the suggestion may be reasonable for pure fcc metals exhibiting typically wavy slip due to high stacking fault energy, it seems unlikely for a material with low stacking fault energy due to which planar slip is favoured. Several images (see Fig. 5.25, Fig. 5.29a or Fig. 5.30c,f) unambiguously prove that the protrusions (or rather PSMs) grow on top of a cluster of closely packed slip bands as a result of the ongoing cyclic deformation. It should be emphasized that although atomic force microscopy is a powerful tool in terms of surface feature quantification, it needs to be supported by other microscopy techniques to reveal the actual mechanisms governing the fatigue damage.

Tanaka and Mura [25] presented a model which seems to sufficiently predict the shape of the slip steps (see e.g. Fig. 5.25a,b). However, the model ignores the role of point defects which was found to be significant for the PSM growth, resulting in more complex shapes of PSMs than just the simple slip steps, as found in this study (compare slip steps in Fig. 5.28b–c with developed PSMs in Fig. 5.30b,d) and also previous studies [9, 32] as well. The predicted shapes are simple and do not explain the real shapes observed later in the fatigue life.

Repetto and Ortiz [15] published a model which considers the PSM shape as a competition between the elongation of the PSB, which pushes the material out of the matrix, and the vacancy flux through the surface, which causes the surface to recede. The model correctly predicts fatigue crack initiation at the PSB-matrix interface. The cracks are supposed to initiate from gradually sharpening grooves on the surface. Although the predicted crack initiation site corresponds to the experimental findings presented here, no gradually sharpening grooves were observed.

The shapes of the early PSMs with extrusions (Fig. 5.28d) are similar to the static extrusions predicted by the EGM model [26] which explains the extrusion and intrusion formation by a combined glide and annihilation of dislocations, and the resulting vacancy production. The static extrusions are expected to form rapidly, and their height is related to the number of point defects produced by the annihilation of edge dislocations in dislocation walls. Subsequent extrusion growth may appear in a thin layer adjacent to the PSB-matrix interface due to temperature-dependent point defect mobility. Due to energy reasons, only vacancy-type point defects are considered, and only extrusions are predicted. Intrusions identified by other investigators [37–38, 143] are labelled as already initiated stage I microcracks. Mughrabi [9] simplified the equation for static extrusion height in the form of Eq. (2.27). Table 9 shows a comparison between the predicted and the observed extrusion heights which were estimated from the TEM micrographs. The extrusion height was calculated from the size of the largest investigated surface grain, and since the grain size in the direction of the active Burgers vector was unknown, the result was multiplied by a factor of 2 in order not to underestimate the prediction. Even though a conservative approach was taken, the comparison exhibits a substantial difference, which indicates that some of the assumptions by the EGM model are incorrect.

Table 9. Comparison of extrusion heights observed and the static extrusion heights predicted by Mughrabi [9]. Note that the extrusion height is regarded in the direction of the active Burgers vector.

		Solutionised state	Aged state
Size of the largest investigated grain		20 μm	20 μm
Predicted height [9]		24 nm	24 nm
Observed height	1 cycle		42 nm (Fig. 5.28d)
	10 cycles	42 nm (Fig. 5.24)	33 nm (Fig. 5.29a)
	100 cycles	93 nm (Fig. 5.26b), 218 nm (Fig. 5.26c)	57 nm (Fig. 5.30c), 95 nm (Fig. 5.30c,d)

Although the predictions by the EGM model yield a good agreement at low temperatures [38] when the diffusion is less significant, there is a notable discrepancy with the room temperature data. Despite the discrepancies shown in Table 9, it is reasonable to assume that the EGM model correctly identified but underestimated the contribution of diffusion effects to the PSM evolution, and hence to the overall fatigue life in a low-cycle regime. A substantial modification to the EGM model presented by Polák [24, 32] seems to fit the presented observations more accurately. The basis of the model is that the point defects (mostly vacancies) are steadily produced in PSBs due to dislocation interactions, and they migrate to the matrix across the PSB-matrix interface. Since the diffusion of vacancies corresponds to the transfer of matter in the opposite direction, mass accumulates in PSBs. Consequently, internal compressive stress in the PSB and internal tensile stress in the adjacent matrix arise, and these stresses are relaxed by surface relief formation. The resulting shape of the surface relief thus reflects the slip history inside the corresponding PSBs. Extrusions are supposed to form first, they evolve on top of the PSBs to be later accompanied by thin intrusions arising at the PSB-matrix interface. Polák reasons that the intrusion formation is delayed due to the higher flow stress of the matrix. This is in appreciable agreement with conducted observations (see the early extrusion without an intrusion in Fig. 5.29a and the extrusion-intrusion pair in Fig. 5.30c). Fatigue cracks initiate from the intrusions which are sharp and cause thus a significant notch effect. This assumption agrees well e.g. with Fig. 5.27d, showing a fatigue crack initiated from the intrusion at the side of a PSM. Contrary to the EGM model, Polák assumes the vacancy production not only in the dislocation walls but also in the channels, resulting in a higher predicted extrusion height [32] and the continuous growth of extrusion over the entire width. Since resistivity data for fatigued superalloys are missing and such measurement was not conducted in the present study, the quantitative approach presented by Polák and Man [32], describing the extrusion and intrusion evolution, could not be compared to the conducted observations. Although the Polák's model seems to describe the evolution of the surface relief accurately on the qualitative basis, quantitative approach also needs to be employed in future to assess the model's predictions in relation to the experimental observations, and to verify its validity for superalloys.

In superalloys, the situation is complicated by the planarity of slip, because of which the PSB structure exhibits no dislocation walls or channels and is rather composed of dislocation pile-ups (Fig. 5.18b). Macro-PSMs observed later in the fatigue life (see Fig. 5.30) are indeed composed not of a single extrusion but a cluster of alternating extrusions and intrusions related to individual PSBs. This is consistent with Polák's prediction of the formation of macro-PSBs in which closely-packed PSBs are separated by thin slabs of the matrix, which is further supported by observations of Ma and Laird [142]. Due to the PSM structural complexity, it is difficult to assess whether the extrusion growth is realised over the entire extrusion width or just at a thin sheet adjacent to the PSB-matrix interface. The intensity of slip in individual PSBs differs, hence the stresses arising from the vacancy flux vary, and the resulting extrusion heights of individual extrusions within a single PSM vary too as shown in Fig. 5.27c. Since

macro-PSBs comprise several individual PSBs, the PSB-matrix interface occurs also within a resulting macro-PSM. This explains the occurrence of intrusions amid a PSM, surrounded by extrusions as shown in Fig. 5.30d.

The Polák's model focuses rather on saturation features. As mentioned in Chapter 6.5.1, the slip-based models approximate well the shapes of the early PSMs in the form of slip steps. It is thus evident that the early slip bands first produce surface steps by the escape of dislocations, and more complex surface relief arise later since vacancy production occurs due to dislocation interactions in PSBs and the subsequent vacancy diffusion needs time [19]. The evidence shown in Fig. 5.24a and Fig. 5.29a, documenting taller and more rugged PSMs, indicates that diffusion effects may occur as early as in the 10^{th} cycle. Later in the fatigue life, the PSM growth becomes prevalent since the diffusion mechanism becomes dominant [144]. Since PSMs may appear on the surface later, it is possible to observe PSMs with several slip steps even after 100 cycles as shown in Fig. 5.30e.

6.6 Fatigue crack initiation

6.6.1 Room temperature

Fatigue cracks observed in this study at room temperature initiated predominantly from PSMs (see the statistics shown in Fig. 5.22) and propagated along active slip planes. This finding is consistent with numerous previous observations [33, 68–70, 118]. Due to the notch effect, most cracks initiated from sharp intrusions, which occurred at the PSB-matrix interface, mostly at the side of a macro-PSM (Fig. 5.30c). In simple metals, crack initiation is likely to appear at the first developed PSMs [145]. In this work, however, nothing of the sort has been observed. Crack initiation from the middle of a macro-PSM was observed too (Fig. 5.30d). Less often, cracks were found also at slip steps as shown in Fig. 5.30e, which strongly resembled 'isolated intrusions' observed by Basinski and Basinski [38]. Since PSM profiles change along the PSM length [20], it is likely that a more developed PSM structure may appear in other parallel sections of the grain. Hence, it can be assumed that the crack in the bottom left of Fig. 5.30e started from an intrusion, which nucleated at some distance from the location of the lamella. This example illustrates that sectioning provides only limited 2D information on the overall 3D behaviour. Unlike Man *et al.* [146] who observed crack initiation from intrusions occurring predominantly at the side of a PSM where the active slip plane is inclined to the surface at an acute angle, cracking was quite often observed also at an obtuse angle (see Fig. 5.14d).

From the other initiation sites, twin boundaries were the most frequent. Sensitivity to cracking at the twin boundaries increased slightly after the ageing treatment (see Fig. 5.22). The overall occurrence was rather low in comparison to some other superalloys (René 88DT [74–75], IN718 [68]). Cyclic slip localization at the twin boundary (see (Fig. 5.18c) is generally promoted due to an additional stress field [77], hence the cracks at twin boundaries (Fig. 5.17d) occur. In LCF regime, stresses are high enough to initiate cracks at other sites, and the resulting occurrence of twin boundary cracks is thus rather seldom.

The role of secondary phase particles in fatigue crack initiation of René 41 superalloy was found to be negligible. This is a grain size effect, since large grain sizes (and thus the reduced number of grain boundaries) promote such behaviour, as follows from the study on cast MAR-M247 superalloy by Šulák *et al.* [33]. In the case of René 41 superalloy, the role of secondary phase particles is rather in grain boundary strengthening, manifested in a low occurrence of cracks initiated at grain boundaries at room temperature, and the deflection of fatigue cracks propagating along an active slip plane, as shown in Fig. 5.17f–g and in more detail in Fig. 5.14g.

6.6.2 Effect of high-temperature exposition (800 °C)

The fatigue crack initiation at grain boundaries, although insignificant at room temperature, is dominant at elevated temperature as a consequence of a synergistic influence of high tensile stress, high temperature and the oxidising environment. This is common for superalloys loaded at high temperatures [22, 33, 70, 81, 85, 127]. Preferential oxidation of the grain boundaries resulting in bulgy oxides (see Fig. 5.19c) is related to the high imposed plastic strain [87], which is common for testing in the LCF regime. Subsequently, the brittle oxide layer cracks due to high tensile stress, which is followed by crack propagation into the bulk along the oxidised grain boundaries (Fig. 5.20e). The resulting fracture is predominantly intergranular (Fig. 5.19a–b) with frequent crack branching (Fig. 5.19b), which is a typical feature of environmental damage [85].

At 800 °C, the twin boundaries and PSMs were oxidised (see Fig. 5.20c), and the initiation from them occurred scarcely (Fig. 5.22). However, crack propagation along the PSMs was still observed (Fig. 5.19d). High material integrity within the grains despite the presence of stress concentrators from oxidic intrusions (Fig. 5.20f) was the reason why cracking at the grain boundaries was preferred.

Grain boundary carbides may increase the susceptibility to environmental attack at 800 °C [85], which may be further promoted by carbide coarsening (shown in Fig. 5.21e). It is unclear whether the impact of coarsened carbides at 800 °C is rather positive (grain boundary strengthening) or negative (embrittlement). Large particles, presumably of M(C,N)-type, accelerate fatigue crack propagation as shown in Fig. 5.13d.

7 Conclusions

In the present work, fatigue tests were conducted on René 41 superalloy in a low-cycle fatigue regime at room and elevated (800 °C) temperatures. The resulting stress-strain response was analysed using the statistical theory of the hysteresis loop to identify the character of cyclic deformation over fatigue life. Fatigue data were related to microscopy observations taken by scanning and transmission electron microscope. The general conclusions are as follows:

- For a comprehensive qualitative study on the aspects of plastic straining of materials with complex microstructures such as Ni-based superalloys, several experimental techniques shall be employed. This particularly constitutes electron microscopy observations with high resolution.
- Analysis of the hysteresis loop using the statistical approach is a powerful tool for deformation behaviour analyses of multiphase materials and complements well the microscopy observations.

Regarding the lifetime and damage behaviour of the investigated alloy, the following conclusions can be drawn:

- At room temperature, the damage is mostly transgranular, and the lifetime is governed by plastic strain amplitude. This is due to fatigue cracks initiating predominantly from persistent slip markings created on the surface as a consequence of the localization of cyclic plastic strain in persistent slip bands.
    - From a service point of view, aged René 41 performs markedly better than the solutionised counterpart due to principal strengthening by γ' precipitates.
    - Solutionised René 41 attains higher plasticity, which justifies its use in applications requiring high plasticity like welding.
- Exposure to fatigue at 800 °C results in significantly shorter lifetimes due to environmental damage in the form of oxides on the surface. The resulting damage is mostly intergranular due to relatively low material integrity at the grain boundaries, which is reduced by oxygen diffusion and carbide coarsening.

Regarding the deformation behaviour, the following conclusions can be drawn:

- At room temperature, plastic deformation is highly inhomogeneous. Two major competing mechanisms were recognized: initial increase in dislocation density promoting cyclic hardening, and localization of cyclic slip in persistent slip bands promoting softening behaviour. Softening by shearing of coherent γ' precipitates is significant only in the early stages of fatigue life, which might be enough to counter the initial cyclic hardening.
- At 800 °C, plastic deformation is more homogeneous. Localization of cyclic slip is less pronounced and, on the other hand, shearing of the γ' is abundant, although decreasingly occurrent over fatigue life. Both mechanisms contribute to cyclic softening observed throughout the fatigue test. Slip bands were observed exclusively along octahedral crystallographic planes.

From the detailed study on the localization of cyclic slip and consequent formation of surface relief over fatigue life of René 41 superalloy, published previously in [34], the following conclusions can be drawn:

- Cyclic slip is localized to persistent slip bands from the first cycle. Consequently, surface roughening arises in the form of persistent slip markings that consist of slip steps, extrusions and intrusions.
- The majority of persistent slip bands nucleates very early in the fatigue life.
- The formation mechanism of slip steps is by an escape of dislocations in (persistent) slip bands to the surface. The most comprehensive description of the slip step formation and evolution was provided by Stinville *et al.* [133].
- Later in fatigue life, vacancies are produced due to dislocation interactions and diffusion effects become significant. A more complex relief in the form of extrusions and intrusions arises. Intrusions are sharp, generally appear later, and cause a significant notch effect for fatigue crack initiation.
- The shape of the persistent slip markings is predicted well by the EGM model [26] as well as Polák's model [24]. However, the former yields a notable discrepancy between predicted and observed extrusion heights. This, together with resistivity measurements [19], implies an underestimation of the diffusion effects in favour of Polák's model. Nevertheless, Polák's model could not be verified in the present research due to missing data for the quantification of surface features. Hence, further effort in this direction should be made in future.

8 References

[1] SURESH, S. *Fatigue of Materials*. 2nd ed. Cambridge: Cambridge University Press, 1998. ISBN 0521578477.

[2] POLÁK, J. *Cyclic Plasticity and Low Cycle Fatigue Life of Metals*. 2nd ed. Prague: Academia, 1991. ISBN 8020000089.

[3] EWING, J.A. and J.C.W. HUMFREY. The fracture of metals under repeated alternations of stress. *Philosophical Transactions of the Royal Society of London. Series A, Containing Papers of a Mathematical or Physical Character*. 1903, **71**(467-476), 241–250. ISSN 2053-9126. DOI:10.1098/rspl.1902.0065

[4] FORSYTH, P.J.E. and D.A. RYDER. Fatigue Fracture: Some Results Derived from the Microscopic Examination of Crack Surfaces. *Aircraft Engineering and Aerospace Technology*. 1960, **32**(4), 96–99. ISSN 0002-2667. DOI:10.1108/eb033233

[5] THOMPSON, N. and N. WADSWORTH. The Origin of Fatigue Fracture in Copper. *The Philosophical Magazine*. 1956, **1**(2), 113–126. ISSN 0031-8086. DOI:10.1080/14786435608238086

[6] LYNCH, S.P. and S. MOUTSOS. A brief history of fractography. *Journal of Failure Analysis and Prevention*. 2006, **6**(6), 54–69. ISSN 1547-7029. DOI:10.1361/154770206X156231

[7] MEYERS, M.A. and K.K. CHAWLA. *Mechanical behavior of materials*. 2nd ed. New York: Cambridge University Press, 2009. ISBN 9780521866750.

[8] POLÁK, J. and M. KLESNIL. The Hysteresis Loop 1. A Statistical Theory. *Fatigue of Engineering Materials and Structures*. 1982, **5**(1), 19–32. ISSN 0160–4112. DOI:doi.org/10.1111/j.1460-2695.1982.tb01221.x

[9] MUGHRABI, H. Cyclic Slip Irreversibilities and the Evolution of Fatigue Damage. *Metallurgical and Materials Transactions B*. 2009, **40**(4), 431–453. ISSN 1073-5615. DOI:10.1007/s11663-009-9240-4

[10] MASING, G. Zur Heyn'schen Theorie der Verfestigung der Metalle durch verborgen elastische Spannungen. In: HARRIES, C. D., ed. *Wissenschaftliche Veröffentlichungen aus dem Siemens-Konzern*. III. Band. Berlin: Springer, 1923, s. 231–239. ISBN 9783642996634.

[11] POLÁK, J. and M. KLESNIL. Statistická teorie hysterezní smyčky. *Kovové materiály*. 1980, **18**(3), 329-344. ISSN 0023-432X.

[12] BURMEISTER, H.-J. and C. HOLSTE. Change of activation area during cyclic deformation. II. Quantitative interpretation with a model of heterogeneous plastie deformation. *Physica Status Solidi (a)*. 1981, **64**(2), 611-624. ISSN 0031-8965. DOI:10.1002/pssa.2210640226

[13] POLÁK, J., M. KLESNIL and J. HELEŠIC. The Hysteresis Loop 2. An Analysis of the Loop Shape. *Fatigue of Engineering Materials and Structures*. Pergamon Press Ltd., 1982, **5**(1), 33–44. ISSN 0160-4112.

[14] POLÁK, J., F. FARDOUN and S. DEGALLAIX. Analysis of the hysteresis loop in stainless steels I. Austenitic and ferritic steels. *Materials Science and Engineering: A*. 2001, **297**(1-2), 144-153. ISSN 0921-5093. DOI:10.1016/S0921-5093(00)01251-X

[15] ŠMÍD, M., M. PETRENEC, J. POLÁK, K. OBRTLÍK and A. CHLUPOVÁ. Analysis of the Effective and Internal Cyclic Stress Components in the Inconel Superalloy Fatigued at Elevated Temperatures. *Advanced Materials Research*. 2011, **278**, 393–398. ISSN 1662-8985.

[16] PETRENEC, M., J. POLÁK, J. TOBIÁŠ, M. ŠMÍD, A. CHLUPOVÁ and R. PETRÁŠ. Analysis of cyclic plastic response of nickel based IN738LC superalloy. *International Journal of Fatigue*. Elsevier, 2013, **65**, 44–55. ISSN 0142-1123. DOI:https://doi.org/10.1016/j.ijfatigue.2013.09.008

[17] HUMPHREYS, F.J. and M. HATHERLY. *Recrystallization and related annealing phenomena*. 2nd ed. Boston: Elsevier, 2004. ISBN 0080441645.

[18] ANTONOPOULOS, J.G., L.M. BROWN and A.T. WINTER. Vacancy dipoles in fatigued copper. *The Philosophical Magazine: A Journal of Theoretical Experimental and Applied Physics*. 2006, **34**(4), 549-563. ISSN 0031-8086. DOI:10.1080/14786437608223793

[19] POLÁK, J. Electrical resistivity of cyclically deformed copper. *Czechoslovak Journal of Physics*. 1969, **19**(3), 315–322. ISSN 0011-4626. DOI:10.1007/BF01712868

[20] POLÁK, J., V. MAZÁNOVÁ, M. HECZKO, I. KUBĚNA and J. MAN. Profiles of persistent slip markings and internal structure of underlying persistent slip bands. *Fatigue & Fracture of Engineering Materials & Structures*. 2017, **40**(7), 1101-1116. ISSN 8756-758X. DOI:10.1111/ffe.12567

[21] PETRENEC, M., J. POLÁK, T. ŠAMOŘIL, J. DLUHOŠ and K. OBRTLÍK. In Situ Study of the Mechanisms of High Temperature Damage in Elastic-Plastic Cyclic Loading of Nickel Superalloy. *Advanced Materials Research*. 2014, **891-892**, 530-535. ISSN 1662-8985. DOI:10.4028/www.scientific.net/AMR.891-892.530

[22] ANTOLOVICH, S.D. and B. LERCH. Cyclic Deformation, Fatigue and Fatigue Crack Propagation in Ni-base Alloys. In: *Superalloys, Supercomposites, Superceramics*. Elsevier, 1989, s. 363-411. ISBN 9780126908459. DOI:10.1016/B978-0-12-690845-9.50018-X

[23] ESSMANN, U. and H. MUGHRABI. Annihilation of Dislocations During Glide at Low Temperatures. In: *Strength of Metals and Alloys*. Elsevier, 1979, s. 1101-1106. ISBN 9781483284125. DOI:10.1016/B978-1-4832-8412-5.50183-1

[24] POLÁK, J. On the role of point defects in fatigue crack initiation. *Materials Science and Engineering* [online]. 1987, **92**, 71–80. ISSN 0025-5416. DOI:10.1016/0025-5416(87)90157-1

[25] TANAKA, K. and T. MURA. A Dislocation Model for Fatigue Crack Initiation. *Journal of Applied Mechanics*. 1981, **48**(1), 97-103. ISSN 0021-8936. DOI:10.1115/1.3157599

[26] ESSMANN, U., U. GÖSELE and H. MUGHRABI. A model of extrusions and intrusions in fatigued metals I. Point-defect production and the growth of extrusions. *Philosophical Magazine A*. 1981, **44**(2), 405-426. ISSN 0141-8610. DOI:10.1080/01418618108239541

[27] DIFFERT, K., U. ESMANN and H. MUGHRABI. A model of extrusions and intrusions in fatigued metals II. Surface roughening by random irreversible slip. *Philosophical Magazine A*. 1986, **54**(2), 237-258. ISSN 0141-8610. DOI:10.1080/01418618608242897

[28] ROSENBLOOM, S.N. and C. LAIRD. Fatigue crack nucleation based on a random slip process—I. Computer model. *Acta Metallurgica et Materialia*. 1993, **41**(12), 3473-3482. ISSN 0956-7151. DOI:10.1016/0956-7151(93)90227-J

[29] REPETTO, E.A. and M. ORTIZ. A micromechanical model of cyclic deformation and fatigue-crack nucleation in f.c.c. single crystals. *Acta Materialia*. 1997, **45**(6), 2577-2595. ISSN 1359-6454. DOI:10.1016/S1359-6454(96)00368-0

[30] DÉPRÉS, C., C.F. ROBERTSON and M.C. FIVEL. Low-strain fatigue in AISI 316L steel surface grains: a three-dimensional discrete dislocation dynamics modelling of the early cycles I. Dislocation microstructures and mechanical behaviour. *Philosophical Magazine*. 2004, **84**(22), 2257-2275. ISSN 1478-6435. DOI:10.1080/14786430410001690051

[31] SANGID, M.D. The physics of fatigue crack initiation. *International Journal of Fatigue*. 2013, **57**, 58-72. ISSN 01421123. DOI:10.1016/j.ijfatigue.2012.10.009

[32] POLÁK, J. and J. MAN. Mechanisms of extrusion and intrusion formation in fatigued crystalline materials. *Materials Science and Engineering: A*. 2014, **596**, 15-24. ISSN 0921-5093. DOI:10.1016/j.msea.2013.12.005

[33] ŠULÁK, I. and K. OBRTLÍK. AFM, SEM and TEM study of damage mechanisms in cyclically strained MAR-M247 at room temperature and high temperatures. *Theoretical and Applied Fracture Mechanics*. 2020, **108**. ISSN 0167-8442. DOI:10.1016/j.tafmec.2020.102606

[34] BABINSKÝ, T., I. KUBĚNA, I. ŠULÁK, T. KRUML, J. TOBIÁŠ and J. POLÁK. Surface relief evolution and fatigue crack initiation in René 41 superalloy cycled at room temperature. *Materials Science and Engineering: A*. 2021, **819**. ISSN 0921-5093. DOI:10.1016/j.msea.2021.141520

[35] MAZÁNOVÁ, V., V. ŠKORÍK, T. KRUML and J. POLÁK. Cyclic response and early damage evolution in multiaxial cyclic loading of 316L austenitic steel. *International Journal of Fatigue*. 2017, **100**, 466–476. ISSN 0142-1123.

[36] POLÁK, J. and M. SAUZAY. Growth of extrusions in localized cyclic plastic straining. *Materials Science and Engineering: A*. 2009, **500**(1-2), 122-129. ISSN 0921-5093. DOI:10.1016/j.msea.2008.09.022

[37] POLÁK, J. and J. MAN. Fatigue crack initiation – The role of point defects. *International Journal of Fatigue*. 2014, **65**, 18-27. ISSN 0142-1123. DOI:10.1016/j.ijfatigue.2013.10.016

[38] BASINSKI, Z.S. and S.J. BASINSKI. Fundamental aspects of low amplitude cyclic deformation in face-centred cubic crystals. *Progress in Materials Science*. 1992, **36**, 89-148. ISSN 0079-6425. DOI:10.1016/0079-6425(92)90006-S

[39] DÉPRÉS, C., C.F. ROBERTSON and M.C. FIVEL. Low-strain fatigue in 316L steel surface grains: a three dimension discrete dislocation dynamics modelling of the early cycles. Part 2. *Philosophical Magazine*. 2006, **86**(1), 79-97. ISSN 1478-6435. DOI:10.1080/14786430500341250

[40] MENG, F., E. FERRIÉ, C. DÉPRÉS and M. FIVEL. 3D discrete dislocation dynamic investigations of persistent slip band formation in FCC metals under cyclical deformation. *International Journal of Fatigue*. 2021, **149**. ISSN 0142-1123. DOI:10.1016/j.ijfatigue.2021.106234

[41] DURAND-CHARRE, M. *The microstructure of superalloys*. Boca Raton: CRC Press, 1997. ISBN 90-5699-097-7.

[42] REED, R.C. *The Superalloys*. Cambridge: Cambridge University Press, 2006. ISBN 9780511541285. DOI:10.1017/CBO9780511541285

[43] PINEAU, A. and S.D. ANTOLOVICH. High temperature fatigue of nickel-base superalloys - A review with special emphasis on deformation modes and oxidation. *Engineering Failure Analysis*. 2009, **16**(8), 2668–2697. ISSN 1350-6307. DOI:10.1016/j.engfailanal.2009.01.010

[44] MATTERSTOCK, B., J.L. MARTIN, J. BONNEVILLE, T. KRUML and P. SPÄTIG. Mechanical strength of the binary compound Ni3Al. *Materials Science and Engineering: A*. 1997, **239-240**, 169-173. ISSN 0921-5093. DOI:10.1016/S0921-5093(97)00577-7

[45] LI, Y., C. LI, L. YU, Z. MA, H. LI and Y. LIU. Characterization of γ′ precipitate and γ/γ′ interface in polycrystalline Ni3Al-based superalloys. *Vacuum*. 2020, **176**. ISSN 0042-207X. DOI:10.1016/j.vacuum.2020.109310

[46] DONACHIE, M.J. and S.J. DONACHIE. *Superalloys. A Technical Guide*. 2nd ed. Materials Park: ASM International, 2002. ISBN 0871707497.

[47] DONG, X., X. ZHANG, K. DU, Y. ZHOU, T. JIN and H. YE. Microstructure of Carbides at Grain Boundaries in Nickel Based Superalloys. *Journal of Materials Science & Technology*. 2012, **28**(11), 1031-1038. ISSN 1005-0302. DOI:10.1016/S1005-0302(12)60169-8

[48] ANTONOV, S., W. AN, S. UTADA et al. Evaluation and Comparison of Damage Accumulation Mechanisms During Non-isothermal Creep of Cast Ni-Based Superalloys. In: TIN, S., M. HARDY, J. CLEWS, J. CORMIER, Q. FENG, J. MARCIN, C. O'BRIEN and A. SUZUKI, ed. *Superalloys 2020*. Cham: Springer International Publishing, 2020, s. 228-239. The Minerals, Metals & Materials Series. ISBN 9783030518332. DOI:10.1007/978-3-030-51834-9_22

[49] ZUBACK, J.S., A.D. IAMS, F. ZHANG, L.A. GIANNUZZI and T.A. PALMER. Stable nitride precipitation in additively manufactured nickel superalloys. *Journal of Alloys and Compounds*. 2022, **910**. ISSN 0925-8388. DOI:10.1016/j.jallcom.2022.164918

[50] DU, B., L. SHENG, C. CUI, J. YANG and X. SUN. Precipitation and evolution of grain boundary boride in a nickel-based superalloy during thermal exposure. *Materials Characterization*. 2017, **128**, 109-114. ISSN 1044-5803. DOI:10.1016/j.matchar.2017.03.038

[51] PETTINARI, F., J. DOUIN, G. SAADA, P. CARON, A. COUJOU and N. CLÉMENT. Stacking fault energy in short-range ordered γ-phases of Ni-based superalloys. *Materials Science and Engineering: A*. 2002, **325**(1-2), 511-519. ISSN 0921-5093. DOI:10.1016/S0921-5093(01)01765-8

[52] CATON, M.J., S.K. JHA, A.H. ROSENBERGER and J.M. LARSEN. Divergence of Mechanisms and the Effect on the Fatigue LIfe Variablity of Rene' 88 DT. In: *Superalloys 2004 (Tenth International Symposium)*. TMS, 2004, s. 305-312. ISBN 0-87339-576-X. DOI:10.7449/2004/Superalloys_2004_305_312

[53] POPE, D.P. and S.S. EZZ. Mechanical properties of Ni3AI and nickel-base alloys with high volume fraction of γ'. *International Metals Reviews*. 1984, **29**(3), 136-167. ISSN 0308-4590. DOI:10.1179/imtr.1984.29.1.136

[54] TAKEUCHI, S. and E. KURAMOTO. Temperature and orientation dependence of the yield stress in Ni3Ga single crystals. *Acta Metallurgica*. 1973, **21**(4), 415-425. ISSN 0001-6160. DOI:10.1016/0001-6160(73)90198-3

[55] PAIDAR, V., D.P. POPE and V. VITEK. A theory of the anomalous yield behavior in L12 ordered alloys. *Acta Metallurgica*. 1984, **32**(3), 435-448. ISSN 0001-6160. DOI:10.1016/0001-6160(84)90117-2

[56] VEYSSIèRE, P. and G. SAADA. Microscopy and plasticity of the L12 γ' phase. In: NABARRO, F.R.N. and M.S. DUESBERY. *Dislocations in Solids: L12 Ordered Alloys* [online]. Vol. 10. Elsevier, 1996, s. 253-441. Dislocations in Solids. ISBN 9780444823700. DOI:10.1016/S1572-4859(96)80008-8

[57] LIU, G., X. ZHANG, X. CHEN et al. Additive manufacturing of structural materials. *Materials Science and Engineering: R: Reports*. 2021, **145**. ISSN 0927-796X. DOI:10.1016/j.mser.2020.100596

[58] ŠULÁK, I. and K. OBRTLÍK. The effect of dwell on thermomechanical fatigue behaviour of Ni-base superalloy Inconel 713LC. *International Journal of Fatigue*. 2023, **166**. ISSN 0142-1123. DOI:10.1016/j.ijfatigue.2022.107238

[59] BABINSKÝ, T. and J. POLÁK. Effective and internal stresses in 713LC and Rene 41 superalloys using analysis of the hysteresis loop shape. *Procedia Structural Integrity*. 2019, **23**, 523–528. ISSN 2452-3216. DOI:10.1016/j.prostr.2020.01.139

[60] ŠULÁK, I., K. OBRTLÍK and L. ČELKO. High-temperature low-cycle fatigue behaviour of HIP treated and untreated superalloy MAR-M247. *Kovové Materiály - Metallic Materials*. 2016, **54**(06), 471-481. ISSN 0023-432X. DOI:10.4149/km_2016_6_471

[61] OBRTLÍK, K., L. ČELKO, T. CHRÁSKA, I. ŠULÁK and P. GEJDOŠ. Effect of alumina-silica-zirconia eutectic ceramic thermal barrier coating on the low cycle fatigue behaviour of cast polycrystalline nickel-based superalloy at 900 °C. *Surface and Coatings Technology*. 2017, **318**, 374-381. ISSN 0257-8972. DOI:10.1016/j.surfcoat.2017.03.003

[62] ŠULÁK, I., K. OBRTLÍK, L. ČELKO, P. GEJDOŠ and D. JECH. High-Temperature Low-Cycle Fatigue Behaviour of MAR-M247 Coated with Newly Developed Thermal and Environmental Barrier Coating. *Advances in Materials Science and Engineering*. 2018, **2018**, 1-8. ISSN 1687-8434. DOI:10.1155/2018/9014975

[63] MINER, R.V., J. GAYDA and R.D. MAIER. Fatigue and creep-fatigue deformation of several nickel-base superalloys at 650 °C. *Metallurgical Transactions A*. 1982, **13**(10), 1755-1765. ISSN 0360-2133. DOI:10.1007/BF02647831

[64] MUJAHID, M., C.A. GATER and J.W. MARTIN. Microstructural Study of a Mechanically Alloyed ODS Superalloy. *Journal of Materials Engineering and Performance*. 1998, **7**(4), 524-532. ISSN 1059-9495. DOI:10.1361/105994998770347684

[65] LIU, L., Q. DING, Y. ZHONG et al. Dislocation network in additive manufactured steel breaks strength–ductility trade-off. *Materials Today*. 2018, **21**(4), 354-361. ISSN 1369-7021. DOI:10.1016/j.mattod.2017.11.004

[66] ŠULÁK, I., T. BABINSKÝ, A. CHLUPOVÁ, A. MILOVANOVIć and L. NÁHLÍK. Effect of building direction and heat treatment on mechanical properties of Inconel 939 prepared by additive manufacturing. *Journal of Mechanical Science and Technology*. 2022. ISSN 1738-494X. DOI:10.1007/s12206-022-2101-7

[67] DELARGY, K.M., S.W.K. SHAW and G.D.W. SMITH. Effects of heat treatment on mechanical properties of high-chromium nickel-base superalloy IN 939. *Materials Science and Technology*. 1986, **2**(10), 1031-1037. ISSN 0267-0836. DOI:10.1179/mst.1986.2.10.1031

[68] FOURNIER, D. and A. PINEAU. Low cycle fatigue behavior of inconel 718 at 298 K and 823 K. *Metallurgical Transactions A*. 1977, **8**(7), 1095-1105. ISSN 0360-2133. DOI:10.1007/BF02667395

[69] MERRICK, H.F. The low cycle fatigue of three wrought nickel-base alloys. *Metallurgical Transactions*. 1974, **5**(4), 891-897. ISSN 0360-2133. DOI:10.1007/BF02643144

[70] LERCH, B.A., N. JAYARAMAN and S.D. ANTOLOVICH. A study of fatigue damage mechanisms in Waspaloy from 25 to 800°C. *Materials Science and Engineering*. 1984, **66**(2), 151-166. ISSN 0025-5416. DOI:10.1016/0025-5416(84)90177-0

[71] STOLTZ, R.E. and A.G. PINEAU. Dislocation-precipitate interaction and cyclic stress-strain behavior of a γ′ strengthened superalloy. *Materials Science and Engineering*. 1978, **34**(3), 275-284. ISSN 0025-5416. DOI:10.1016/0025-5416(78)90060-5

[72] JIANG, R., D.J. BULL, A. EVANGELOU et al. Strain accumulation and fatigue crack initiation at pores and carbides in a SX superalloy at room temperature. *International Journal of Fatigue*. 2018, **114**, 22-33. ISSN 0142-1123. DOI:10.1016/j.ijfatigue.2018.05.003

[73] ANTON, D.L. and M.E. FINE. Fatigue crack evolution in overaged Ni-14.4at.% Al alloy with coherent precipitates. *Materials Science and Engineering*. 1983, **58**(1), 135-142. ISSN 0025-5416. DOI:10.1016/0025-5416(83)90145-3

[74] MIAO, J., T.M. POLLOCK and J. WAYNE JONES. Crystallographic fatigue crack initiation in nickel-based superalloy René 88DT at elevated temperature. *Acta Materialia*. 2009, **57**(20), 5964-5974. ISSN 1359-6454. DOI:10.1016/j.actamat.2009.08.022

[75] STINVILLE, J.-C., N. VANDERESSE, F. BRIDIER, P. BOCHER and T.M. POLLOCK. High resolution mapping of strain localization near twin boundaries in a nickel-based superalloy. *Acta Materialia*. 2015, **98**, 29-42. ISSN 1359-6454. DOI:10.1016/j.actamat.2015.07.016

[76] TEXIER, D., J. CORMIER, P. VILLECHAISE, J.-C. STINVILLE, C.J. TORBET, S. PIERRET and T.M. POLLOCK. Crack initiation sensitivity of wrought direct aged alloy 718 in the very high cycle fatigue regime: the role of non-metallic inclusions. *Materials Science and Engineering: A*. 2016, **678**, 122-136. ISSN 0921-5093. DOI:10.1016/j.msea.2016.09.098

[77] HEINZ, A. and P. NEUMANN. Crack initiation during high cycle fatigue of an austenitic steel. *Acta Metallurgica et Materialia*. 1990, **38**(10), 1933-1940. ISSN 0956-7151. DOI:10.1016/0956-7151(90)90305-Z

[78] PETRENEC, M., K. OBRTLÍK and J. POLÁK. High Temperature Low Cycle Fatigue of Superalloys Inconel 713LC and Inconel 792-5A. *Key Engineering Materials*. 2007, **348–349**, 101–104. ISSN 1662-9795. DOI:10.4028/www.scientific.net/KEM.348-349.101

[79] REPPICH, B., P. SCHEPP and G. WEHNER. Some new aspects concerning particle hardening mechanisms in γ' precipitating nickel-base alloys—II. Experiments. *Acta Metallurgica*. 1982, **30**(1), 95-104. ISSN 0001-6160. DOI:10.1016/0001-6160(82)90049-9

[80] ŠULÁK, I., K. OBRTLÍK, L. ČELKO, T. CHRÁSKA, D. JECH and P. GEJDOŠ. Low cycle fatigue performance of Ni-based superalloy coated with complex thermal barrier coating. *Materials Characterization*. 2018, **139**, 347-354. ISSN 1044-5803. DOI:10.1016/j.matchar.2018.03.023

[81] ANTOLOVICH, S.D., S. LIU and R. BAUR. Low cycle fatigue behavior of René 80 at elevated temperature. *Metallurgical Transactions A*. 1981, **12**(3), 473-481. ISSN 0360-2133. DOI:10.1007/BF02648545

[82] PLUMBRIDGE, W.J. and E.G. ELLISON. Low-cycle-fatigue behaviour of superalloy blade materials at elevated temperature. *Materials Science and Technology*. 1987, **3**(9), 706-715. ISSN 0267-0836. DOI:10.1179/mst.1987.3.9.706

[83] HYNNÄ, A., V.-T. KUOKKALA, J. LAURILA and P. KETTUNEN. High-temperature low-cycle fatigue behavior of superalloy MA 760. *Journal of Materials Engineering and Performance*. 1993, **2**(4), 531-535. ISSN 1059-9495. DOI:10.1007/BF02661737

[84] WAGENHUBER, E.-G., V.B. TRINDADE and U. KRUPP. The Role of Oxygen-Grain-Boundary Diffusion During Intercrystalline Oxidation and Intergranular Fatigue Crack Propagation in Alloy 718. In: *Superalloys 718, 625, 706 and Various Derivatives (2005)*. TMS, 2005, s. 591-600. ISBN 9780873396028. DOI:10.7449/2005/Superalloys_2005_591_600

[85] MCMAHON, C.J. On the mechanism of premature in-service failure nickel-base superalloy gas turbine blades. *Materials Science and Engineering*. 1974, **13**(3), 295-297. ISSN 0025-5416. DOI:10.1016/0025-5416(74)90202-X

[86] KITAGUCHI, H.S., H.Y. LI, H.E. EVANS, R.G. DING, I.P. JONES, G. BAXTER and P. BOWEN. Oxidation ahead of a crack tip in an advanced Ni-based superalloy. *Acta Materialia*. 2013, **61**(6), 1968-1981. ISSN 1359-6454. DOI:10.1016/j.actamat.2012.12.017

[87] JIANG, R., D. PROPRENTNER, M. CALLISTI, B. SHOLLOCK, X.T. HU, Y.D. SONG and P.A.S. REED. Role of oxygen in enhanced fatigue cracking in a PM Ni-based superalloy: Stress assisted grain boundary oxidation or dynamic embrittlment?. *Corrosion Science*. 2018, **139**, 141-154. ISSN 0010-938X. DOI:10.1016/j.corsci.2018.05.001

[88] GABB, T.P., S.L. DRAPER, D.R. HULL, R.A. MACKAY and M.V. NATHAL. The role of interfacial dislocation networks in high temperature creep of superalloys. *Materials Science and Engineering: A*. 1989, **118**, 59-69. ISSN 0921-5093. DOI:10.1016/0921-5093(89)90058-0

[89] CHUNG, D.W., M. CHATURVEDI and D.J. LLOYD. The characteristics of the barrier during serrated yielding in the γ' precipitation hardened super alloys (Co-Ni-Cr-Ti system). *Acta Metallurgica*. 1976, **24**(3), 227-232. ISSN 0001-6160. DOI:10.1016/0001-6160(76)90072-9

[90] HAYES, R.W. and W.C HAYES. On the mechanism of delayed discontinuous plastic flow in an age-hardened nickel alloy. *Acta Metallurgica*. 1982, **30**(7), 1295-1301. ISSN 0001-6160. DOI:10.1016/0001-6160(82)90148-1

[91] RAO, K.B.S., H. SCHUSTER and G.R. HALFORD. On massive carbide precipitation during high temperature low cycle fatigue in alloy 800H. *Scripta Metallurgica et Materialia*. 1994, **31**(4), 381-386. ISSN 0956-716X. DOI:10.1016/0956-716X(94)90004-3

[92] DONACHIE, M.J., A.A. PINKOWISH, W.P. DANESI, J.F. RADAVICH and W.H. COUTS. Effect of hot work on the properties of Waspaloy. *Metallurgical and Materials Transactions B*. 1970, **1**(9), 2623-2630. ISSN 1073-5615. DOI:10.1007/BF03038394

[93] HEEP, L., D. BÜRGER, C. BONNEKOH, P. WOLLGRAMM, A. DLOUHÝ and G. EGGELER. The effect of deviations from precise [001] tensile direction on creep of Ni-base single crystal superalloys. *Scripta Materialia*. 2022, **207**. ISSN 1359-6462. DOI:10.1016/j.scriptamat.2021.114274

[94] LILENSTEN, L., P. KÜRNSTEINER, J.R. MIANROODI, A. CERVELLON, J. MOVERARE, M. SEGERSÄLL, S. ANTONOV and P. KONTIS. Segregation of Solutes at Dislocations: A New Alloy Design Parameter for Advanced Superalloys. In: TIN, S., M. HARDY, J. CLEWS, J. CORMIER, Q. FENG, J. MARCIN, C. O'BRIEN and A. SUZUKI, ed. *Superalloys 2020*. Cham: Springer International Publishing, 2020, s. 41-51. The Minerals, Metals & Materials Series. ISBN 9783030518332. DOI:10.1007/978-3-030-51834-9_4

[95] WU, X., S.K. MAKINENI, P. KONTIS, G. DEHM, D. RAABE, B. GAULT and G. EGGELER. On the segregation of Re at dislocations in the γ' phase of Ni-based single crystal superalloys. *Materialia*. 2018, **4**, 109-114. ISSN 2589-1529. DOI:10.1016/j.mtla.2018.09.018

[96] ABEL, A. Fatigue of copper single crystals at low constant plastic strain amplitudes. *Materials Science and Engineering*. 1978, **36**(1), 117–124. ISSN 0025-5416. DOI:10.1016/0025-5416(78)90201-X

[97] BROOM, T. and R.K. HAM. The hardening of copper single crystals by fatigue. *Proceedings of the Royal Society of London. Series A. Mathematical and Physical Sciences*. 1959, **251**(1265), 186–199. ISSN 0080-4630. DOI:10.1098/rspa.1959.0101

[98] ANTOLOVICH, S.D. Microstructural aspects of fatigue in Ni-base superalloys. *Philosophical Transactions of the Royal Society A: Mathematical, Physical and Engineering Sciences*. 2015, **373**(2038). ISSN 1364-503X. DOI:10.1098/rsta.2014.0128

[99] PHILLIPS, E.P. *Fatigue of René 41 Under Constant- and Random- Amplitude Loading at Room and Elevated Temperatures*. Washington, D.C.: National Aeronautics and Space Administration, 1965. NASA TN D-3075.

[100] ELKIND, S. A radiation-cooled nuclear rocket nozzle for long firing durations. *Journal of Spacecraft and Rockets*. 1965, **2**(3), 353-357. ISSN 0022-4650. DOI:10.2514/3.28183

[101] KAYACAN, R., R. VAROL and O. KIMILLI. The effects of pre- and post-weld heat treatment variables on the strain-age cracking in welded Rene 41 components. *Materials Research Bulletin*. 2004, **39**(14-15), 2171-2186. ISSN 0025-5408. DOI:10.1016/j.materresbull.2004.08.003

[102] VANDER VOORT, G.F., ed. *ASM Handbook, Volume 9: Metallography and Microstructures*. Materials Park, OH: ASM International, 2004. ISBN 0871707063. DOI:10.31399/asm.hb.v09.9781627081771

[103] COLLINS, H.E. Relative Stability of Carbide and Intermetallic Phases in Nickel-Base Superalloys. In: *International Symposium on Structural Stability in Superalloys (1968)*. Seven Springs, PA, 1968, s. 171-198. DOI:10.7449/1968/SUPERALLOYS_1968_171_198

[104] MANONUKUL, A., F.P.E. DUNNE and D. KNOWLES. Physically-based model for creep in nickel-base superalloy C263 both above and below the gamma solvus. *Acta Materialia*. 2002, **50**(11), 2917-2931. ISSN 1359-6454. DOI:10.1016/S1359-6454(02)00119-2

[105] CHATTERJEE, S., Y. LI and G. PO. A discrete dislocation dynamics study of precipitate bypass mechanisms in nickel-based superalloys. *International Journal of Plasticity*. 2021, **145**. ISSN 0749-6419. DOI:10.1016/j.ijplas.2021.103062

[106] LERCH, B. and V. GEROLD. Room temperature deformation mechanisms in Nimonic 80A. *Acta Metallurgica*. 1985, **33**(9), 1709-1716. ISSN 0001-6160. DOI:10.1016/0001-6160(85)90165-8

[107] LERCH, B.A. and V. GEROLD. Cyclic hardening mechanisms in NIMONIC 80A. *Metallurgical Transactions A*. 1987, **18**(12), 2135-2141. ISSN 0360-2133. DOI:10.1007/BF02647085

[108] MUGHRABI, H. Microstructural mechanisms of cyclic deformation, fatigue crack initiation and early crack growth. *Philosophical Transactions of the Royal Society A: Mathematical, Physical and Engineering Sciences*. 2015, **373**(2038). ISSN 1364-503X. DOI:10.1098/rsta.2014.0132

[109] GUTH, S., S. DOLL and K.-H. LANG. Influence of phase angle on lifetime, cyclic deformation and damage behavior of Mar-M247 LC under thermo-mechanical fatigue. *Materials Science and Engineering: A*. 2015, **642**, 42-48. ISSN 0921-5093. DOI:10.1016/j.msea.2015.06.055

[110] WOODFORD, D.A. Environmental damage of a cast nickel base superalloy. *Metallurgical Transactions A*. 1981, **12**(2), 299-308. ISSN 0360-2133. DOI:10.1007/BF02655203

[111] YANG, S.L., U. KRUPP, H.-J. CHRIST and V. BRAZ TRINDADE. The Relationship between Grain Boundary Character and the Intergranular Oxide Distribution in IN718 Superalloy. *Advanced Engineering Materials*. 2005, **7**(8), 723-726. ISSN 1438-1656. DOI:10.1002/adem.200500036

[112] ROMAIN, C., D. TEXIER, C. DESGRANGES, J. CORMIER, S. KNITTEL, D. MONCEAU and D. DELAGNES. Oxidation of Thin Nickel-Based Superalloy Specimens: Kinetics Study and Mechanical Integrity. *Oxidation of Metals*. 2021, **96**(1-2), 169-182. ISSN 0030-770X. DOI:10.1007/s11085-021-10075-2

[113] LYTLE, F.W., R.B. GREEGOR and T. LUHMAN. Examination of the titanium environment in a René 41 nickel base superalloy by X-ray absorption spectroscopy. *Metallurgical Transactions A*. 1986, **17**(4), 739-741. ISSN 0360-2133. DOI:10.1007/BF02643995

[114] PRAGER, M. and G. SINES. Embrittlement of Precipitation Hardenable Nickel-Base Alloys by Oxygen. *Journal of Basic Engineering*. 1971, **93**(2), 225-230. ISSN 0021-9223. DOI:10.1115/1.3425217

[115] Y.-Y., WANG, CHEN L.-J., WANG B.S. and ZHANG S.-Q. Low cycle fatigue and fracture behavior of Inconel 625 alloy at room temperature. *Journal of Shenyang University of Technology*. 2016, **38**(2), 170-174. DOI:10.7688/j.issn.1000-1646.2016.02.09

[116] BARRETT, P.R., R. AHMED, M. MENON and T. HASSAN. Isothermal low-cycle fatigue and fatigue-creep of Haynes 230. *International Journal of Solids and Structures*. 2016, **88-89**, 146-164. ISSN 0020-7683. DOI:10.1016/j.ijsolstr.2016.03.011

[117] JABLONSKI, D.A. *Fatigue Behavior of Hastelloy X at Elevated Temperatures in Air, Vacuum and Oxygen Environment*. 1978. Dissertation thesis. Massachusetts Institute of Technology. Vedoucí práce R.M. Pelloux.

[118] GANESH SUNDARA RAMAN, S. and K.A. PADMANABHAN. Effect of prior cold work on the room-temperature low-cycle fatigue behaviour of AISI 304LN stainless steel. *International Journal of Fatigue*. 1996, **18**(2), 71-79. ISSN 0142-1123. DOI:10.1016/0142-1123(95)00078-X

[119] HONG, S.-G. and S.-B. LEE. Dynamic strain aging under tensile and LCF loading conditions, and their comparison in cold worked 316L stainless steel. *Journal of Nuclear Materials*. 2004, **328**(2-3), 232-242. ISSN 0022-3115. DOI:10.1016/j.jnucmat.2004.04.331

[120] LIU, T.K., G.L. WU, C.K. LIU, Z.H. NIE, T. UNGÁR, Y. REN and Y.D. WANG. Interface coherency strain relaxation due to plastic deformation in single crystal Ni-base superalloys. *Materials Science and Engineering: A*. 2013, **568**, 83-87. ISSN 0921-5093. DOI:10.1016/j.msea.2013.01.035

[121] POLÁK, J., F. FARDOUN and S. DEGALLAIX. Analysis of the hysteresis loop in stainless steels II. Austenitic–ferritic duplex steel and the effect of nitrogen. *Materials Science and Engineering: A*. 2001, **297**(1-2), 154-161. ISSN 0921-5093. DOI:10.1016/S0921-5093(00)01252-1

[122] MELLO, A.W., A. NICOLAS and M.D. SANGID. Fatigue strain mapping via digital image correlation for Ni-based superalloys: The role of thermal activation on cube slip. *Materials Science and Engineering: A*. 2017, **695**, 332-341. ISSN 0921-5093. DOI:10.1016/j.msea.2017.04.002

[123] KONG, W.-W., C. YUAN, B.-N. ZHANG, H.-Y. QIN and G.-P. ZHAO. Investigation on low-cycle fatigue behaviors of wrought superalloy GH4742 at room-temperature and 700 °C. *Materials Science and Engineering: A*. 2019, **751**, 226-236. ISSN 0921-5093. DOI:10.1016/j.msea.2019.02.075

[124] LEÓN-CÁZARES, F. D., F. MONNI, T. JACKSON, E. I. GALINDO-NAVA and C.M.F. RAE. Stress response and microstructural evolution of nickel-based superalloys during low cycle fatigue: Physics-based modelling of cyclic hardening and softening. *International Journal of Plasticity*. 2020, **128**. ISSN 0749-6419. DOI:10.1016/j.ijplas.2020.102682

[125] LU, Y.L., L.J. CHEN, G.Y. WANG et al. Hold time effects on low cycle fatigue behavior of HAYNES 230® superalloy at high temperatures. *Materials Science and Engineering: A*. 2005, **409**(1-2), 282-291. ISSN 0921-5093. DOI:10.1016/j.msea.2005.05.120

[126] ANTOLOVICH, S.D., E. ROSA and A. PINEAU. Low cycle fatigue of René 77 at elevated temperatures. *Materials Science and Engineering*. 1981, **47**(1), 47-57. ISSN 0025-5416. DOI:10.1016/0025-5416(81)90040-9

[127] MARCHIONNI, M., G.A. OSINKOLU and G. ONOFRIO. High temperature low cycle fatigue behaviour of UDIMET 720 Li superalloy. *International Journal of Fatigue*. 2002, **24**(12), 1261-1267. ISSN 0142-1123. DOI:10.1016/S0142-1123(02)00043-9

[128] ZHAO, L.G., J. TONG, B. VERMEULEN and J. BYRNE. On the uniaxial mechanical behaviour of an advanced nickel base superalloy at high temperature. *Mechanics of Materials*. 2001, **33**(10), 593-600. ISSN 0167-6636. DOI:10.1016/S0167-6636(01)00071-0

[129] OBRTLÍK, K., M. PETRENEC, J. MAN, J. POLÁK and K. HRBÁČEK. Isothermal fatigue behavior of cast superalloy Inconel 792-5A at 23 and 900 °C. *Journal of Materials Science*. 2009, **44**(12), 3305-3314. ISSN 0022-2461. DOI:10.1007/s10853-009-3446-3

[130] OBRTLÍK, K., A. CHLUPOVÁ, M. PETRENEC and J. POLÁK. Low Cycle Fatigue of Cast Superalloy Inconel 738LC at High Temperature. *Key Engineering Materials*. 2008, **385-387**, 581-584. ISSN 1662-9795. DOI:10.4028/www.scientific.net/KEM.385-387.581

[131] PETTINARI-STURMEL, F., J. DOUIN, A. COUJOU and N. CLÉMENT. Characterisation of short-range order using dislocations. *Zeitschrift für Metallkunde*. 2006, **97**(3), 200-204. ISSN 0044-3093. DOI:10.3139/146.101243

[132] LEÓN-CÁZARES, F.D., R. SCHLÜTTER, T. JACKSON, E.I. GALINDO-NAVA and C.M.F. RAE. A multiscale study on the morphology and evolution of slip bands in a nickel-based superalloy during low cycle fatigue. *Acta Materialia*. 2020, **182**, 47-59. ISSN 1359-6454. DOI:10.1016/j.actamat.2019.10.033

[133] STINVILLE, J.-C., P.G. CALLAHAN, M.A. CHARPAGNE, M.P. ECHLIN, V. VALLE and T.M. POLLOCK. Direct measurements of slip irreversibility in a nickel-based superalloy using high resolution digital image correlation. *Acta Materialia*. 2020, **186**, 172-189. ISSN 1359-6454. DOI:10.1016/j.actamat.2019.12.009

[134] HONG, S.I. and C. LAIRD. Cyclic deformation behaviour of Cu-16at.%Al single crystals part II: Cyclic hardening and slip band behavior. *Materials Science and Engineering: A*. 1990, **128**(1), 55-75. ISSN 0921-5093. DOI:10.1016/0921-5093(90)90096-L

[135] MIAO, J., T.M. POLLOCK and J.W. JONES. Fatigue Crack Initiation in Nickel-Based Superalloy René 88 DT at 593 °C. In: *Superalloys 2008 (Eleventh International Symposium)*. TMS, 2008, s. 589-597. ISBN 978-0-87339-728-5. DOI:10.7449/2008/Superalloys_2008_589_597

[136] HÖPPEL, H.W., P. GOIK, C. KRECHEL and M. GÖKEN. Ex and in situ investigations on the role of persistent slip bands and grain boundaries in fatigue crack initiation. *Journal of Materials Research*. 2017, **32**(23), 4276-4286. ISSN 0884-2914. DOI:10.1557/jmr.2017.313

[137] LAVENSTEIN, S., Y. GU, D. MADISETTI and J.A. EL-AWADY. The heterogeneity of persistent slip band nucleation and evolution in metals at the micrometer scale. *Science*. 2020, **370**(6513). ISSN 0036-8075. DOI:10.1126/science.abb2690

[138] BASINSKI, Z.S. and S.J. BASINSKI. Formation and growth of subcritical fatigue cracks. *Scripta Metallurgica*. 1984, **18**(8), 851-856. ISSN 0036-9748. DOI:10.1016/0036-9748(84)90409-5

[139] POLÁK, J., V. MAZÁNOVÁ, M. HECZKO, R. PETRÁŠ, I. KUBĚNA, L. CASALENA and J. MAN. The role of extrusions and intrusions in fatigue crack initiation. *Engineering Fracture Mechanics*. 2017, **185**, 46-60. ISSN 0013-7944. DOI:10.1016/j.engfracmech.2017.03.006

[140] SEIDAMETOVA, G., J.-B. VOGT and I. PRORIOL SERRE. The early stage of fatigue crack initiation in a 12%Cr martensitic steel. *International Journal of Fatigue*. 2018, **106**, 38-48. ISSN 0142-1123. DOI:10.1016/j.ijfatigue.2017.09.006

[141] CRETEGNY, L. and A. SAXENA. AFM characterization of the evolution of surface deformation during fatigue in polycrystalline copper. *Acta Materialia*. 2001, **49**(18), 3755-3765. ISSN 1359-6454. DOI:10.1016/S1359-6454(01)00271-3

[142] MA, B.-T. and C. LAIRD. Overview of fatigue behavior in copper single crystals—I. Surface morphology and stage I crack initiation sites for tests at constant strain amplitude. *Acta Metallurgica*. 1989, **37**(2), 325-336. ISSN 0001-6160. DOI:10.1016/0001-6160(89)90217-4

[143] LUKÁŠ, P. and L. KUNZ. Role of persistent slip bands in fatigue. *Philosophical Magazine*. 2004, **84**(3-5), 317-330. ISSN 1478-6435. DOI:10.1080/14786430310001610339

[144] MAN, J., M. VALTR, A. WEIDNER, M. PETRENEC, K. OBRTLÍK and J. POLÁK. AFM study of surface relief evolution in 316L steel fatigued at low and high temperatures. *Procedia Engineering*. 2010, **2**(1), 1625-1633. ISSN 1877-7058. DOI:10.1016/j.proeng.2010.03.175

[145] FATHI SOLA, J., R. KELTON, E.I. MELETIS and H. HUANG. Predicting crack initiation site in polycrystalline nickel through surface topography changes. *International Journal of Fatigue*. 2019, **124**, 70-81. ISSN 0142-1123. DOI:10.1016/j.ijfatigue.2019.02.027

[146] MAN, J., P. KLAPETEK, O. MAN, A. WEIDNER, K. OBRTLÍK and J. POLÁK. Extrusions and intrusions in fatigued metals. Part 2. AFM and EBSD study of the early growth of extrusions and intrusions in 316L steel fatigued at room temperature. *Philosophical Magazine*. 2009, **89**(16), 1337-1372. ISSN 1478-6435. DOI:10.1080/14786430902917624

9 List of abbreviations and symbols

Symbol	Dimension	Meaning
a	(m^{-1})	Reciprocal characteristic diffusion distance
b	(-)	Fatigue strength exponent
c	(Hz)	Fatigue ductility exponent
C	(-)	Proportionality parameter of the Weibull distribution function
d	(m)	Grain size
d	(m)	Precipitate size
d_c	(m)	Parameter characterizing the material-dependent delay between the start of extrusion and intrusion growth
e	(m)	(Static) extrusion height
E	(Pa)	Young's modulus
E_{eff}	(Pa)	Effective Young's modulus
f	(Hz)	Frequency of strain cycling
G	(Pa)	Shear modulus
i	(m)	Intrusion depth
k	(-)	Shape parameter of the Weibull distribution function
k_{cr}	(-)	Crack criterion
K	(Pa)	Material constant
l	(m)	Length of the PSB in the direction of active Burgers vector
m	(-)	Schmid factor
n	(-)	Cyclic strain hardening exponent
N	(-)	Number of cycles
N_f	(-)	Number of cycles until fracture
p	(-)	Vacancy production rate in a PSB
r_{im}	(m^{-1})	Maximum intrusion growth rate
R	(-)	Stress asymmetry
T	(°C)	Temperature
U	(V)	Voltage
w	(m)	Width of a PSB
x	(m)	Distance from the middle of a PSB
α	(-)	Parameter characterizing short-range obstacles
γ	(-)	Shear strain
$\Delta\varepsilon_p$	(-)	Width of the hysteresis loop
ε	(-)	Engineering strain
ε_a	(-)	Strain amplitude
ε_{ap}	(-)	Plastic strain amplitude
$\varepsilon_{ap,50\%Nf}$	(-)	Plastic strain amplitude at half-life
ε_c	(-)	Cumulative plastic strain
ε_e	(-)	Elastic strain
ε_f'	(-)	Fatigue ductility coefficient, also true fracture strain
ε_m	(-)	Mean strain

ε_{max}	(-)	Maximum strain
ε_{min}	(-)	Minimum strain
ε_{mp}	(-)	Mean plastic strain
$\varepsilon_{max,p}$	(-)	Maximum plastic strain
$\varepsilon_{min,p}$	(-)	Minimum plastic strain
ε_p	(-)	Plastic strain
ε_{pr}	(-)	Relative plastic strain
ε_r	(-)	Relative strain
ε_t	(-)	Total strain
$\dot{\varepsilon}$	(s^{-1})	Strain rate
η	(-)	Scale parameter of the Weibull distribution function
Θ	(-)	Location parameter of the Weibull distribution function
Θ	(°, rad)	Angle between the loading direction and the slip plane normal
λ	(°, rad)	Angle between the loading direction and the slip direction
ν_p	(-)	Poisson's ratio
ρ_c	(m^{-2})	Edge dislocation density
σ	(Pa)	Engineering stress
σ_a	(Pa)	Stress amplitude
$\sigma_{a,max}$	(Pa)	Maximum stress amplitude over the fatigue test
$\sigma_{a,50\%Nf}$	(Pa)	Stress amplitude at half-life
σ_e	(Pa)	Effective stress component
σ_{e0}	(Pa)	Initial effective stress
$\sigma_{e0,\gamma}$	(Pa)	Initial effective stress of the γ phase
$\sigma_{e0,\gamma'}$	(Pa)	Initial effective stress of the γ' phase
σ_{es}	(Pa)	Saturated effective stress
$\sigma_{es,\gamma}$	(Pa)	Effective stress of the γ phase
$\sigma_{es,\gamma'}$	(Pa)	Effective stress of the γ' phase
σ_f'	(Pa)	Fatigue strength coefficient
σ_i	(Pa)	Internal stress component
σ_{ic}	(Pa)	Critical internal stress
σ_m	(Pa)	Mean stress
σ_{max}	(Pa)	Maximum stress
σ_{min}	(Pa)	Minimum stress
σ_r	(Pa)	Relative stress
σ_0	(Pa)	Yield limit, critical flow stress
τ	(Pa)	Shear stress
τ_0	(Pa)	Critical shear stress

Abbreviation	Meaning
AM	Additive manufacturing
APB	Anti-phase boundary
CSF	Complex stacking fault
EDS	Energy-dispersive spectroscopy
FIB	Focused ion beam
HIP	Hot isostatic pressing
HRTEM	High resolution transmission electron microscopy
LA	Loading axis
LCF	Low-cycle fatigue
PSB	Persistent slip band
PSM	Persistent slip marking
OES	Optical emission spectroscopy
RT	Room temperature
SAED	Selected area electron diffraction
SEM	Scanning electron microscopy
SESF	Superlattice extrinsic stacking fault
SISF	Superlattice intrinsic stacking fault
STEM	Scanning transmission electron microscopy
TCP	Topologically closed-packed (phases)
TEM	Transmission electron microscopy

10 List of publications by the author

Publications related to the dissertation topic

T. Babinský, J. Polák, Effective and internal stresses in 713LC and Rene 41 superalloys using analysis of the hysteresis loop shape, Procedia Structural Integrity, 23 (2019) 523–528. https://doi.org/10.1016/j.prostr.2020.01.139.

T. Babinský, I. Kuběna, I. Šulák, T. Kruml, J. Tobiáš, J. Polák, Surface relief evolution and fatigue crack initiation in René 41 superalloy cycled at room temperature, Materials Science & Engineering: A, 819 (2021), https://doi.org/10.1016/j.msea.2021.141520.

Other publications

T. Babinský, J. Dluhoš, A. Candeias, M. Petrenec, In-situ study of recrystallization and deformation processes in free-cutting steel, in: Metal 2018 – 27th International Conference On Metallurgy And Materials, Conference Proceedings, Brno, (2018) 35–39.

I. Šulák, K. Obrtlík, **T. Babinský**, S. Guth, The low cycle fatigue behaviour of MAR-M247 superalloy under different strain rates and cycle shapes at 750 °C, International Journal of Fatigue. 164 (2022). https://doi.org/10.1016/j.ijfatigue.2022.107133.

A. Chlupová, I. Šulák, **T. Babinský**, J. Polák, Intergranular fatigue crack initiation in polycrystalline copper, Materials Science & Engineering: A. 848 (2022). https://doi.org/10.1016/j.msea.2022.143357.

I. Šulák, **T. Babinský**, A. Chlupová, A. Milovanović, L. Náhlík, Effect of building direction and heat treatment on mechanical properties of Inconel 939 prepared by additive manufacturing, Journal of Mechanical Science and Technology, (2022). https://doi.org/10.1007/s12206-022-2101-7.

T. Babinský, I. Šulák, I. Kuběna, J. Man, A. Weiser, E. Švábenská, L. Englert, S. Guth, Thermomechanical fatigue of additively manufactured 316L steel, Materials Science & Engineering: A, 869 (2023), https://doi.org/10.1016/j.msea.2023.144831.

11 International experience

Research internships

- October 2020 – May 2021: Karlsruhe Institute of Technology, Institute for Applied Materials, supervision by Dr.-Ing. Stefan Guth.
- October 2021 – December 2021: University of Belgrade, Innovation Center at the Faculty of Mechanical Engineering, supervision by Prof. Aleksandar Sedmak.

International conferences

- Ninth International Conference on Materials Structure & Micromechanics of Fracture (MSMF9) held in Brno, Czech Republic in June 2019:

T. Babinský, J. Polák, Effective and internal stresses in 713LC and Rene 41 superalloys using analysis of the hysteresis loop shape (poster)

- European Conference on Fracture (ECF 2022) held in Funchal, Portugal in June 2022:

T. Babinský, I. Šulák, A. Weiser, L. Englert, S. Guth, Damage mechanisms in additively manufactured 316L stainless steel subjected to thermomechanical fatigue (oral)

- Tenth International Conference on Materials Structure & Micromechanics of Fracture (MSMF10) held in Brno, Czech Republic in September 2022:

T. Babinský, I. Šulák, A. Weiser, L. Englert, S. Guth, Damage mechanisms of SLM-printed 316L steel subjected to thermomechanical fatigue (oral)

- EuroSuperalloys 2022 held in Bamberg, Germany in September 2022:

T. Babinský, I. Šulák, A. Chlupová, A. Milovanović, L. Náhlík, Mechanisms of fatigue damage in additively manufactured IN939 superalloy (oral)